Clemson University

TigerPrints

12-2023

Studies on Electrochemical Hydrogen Isotope Separation

Liyanage Mayura Sankalpa Silva
Clemson University, lsilva@clemson.edu

Studies on Electrochemical Hydrogen Isotope Separation

A Dissertation
Presented to
the Graduate School of
Clemson University

In Partial Fulfillment
of the Requirements for the Degree
Doctor of Philosophy
Chemistry

---

by
Liyanage Mayura Sankalpa Silva
December 2023

Accepted by:
Prof. Stephen Creager, Committee Chair
Prof. Ken Marcus
Prof. George Chumanov
Dr. Xin Xiao

Abstract

Hydrogen isotope separation using Proton Exchange Membrane (PEM) based electrochemical cells represents a potentially attractive process in both scientific and industrial arenas. Historically, Chemical Vapor Deposited (CVD) graphene's role in this separation process has been acknowledged as significant. However, this dissertation contends with the traditional understanding by focusing on the role of unintentional introduction of other cations besides proton and deuteron, particularly ammonium and copper, during the CVD graphene transfer onto PEMs like Nafion. Through rigorous examination and experimentation, it was discerned that these cations might have profound implications on observed proton/deuteron transportation within membrane based electrochemical cells.

A comprehensive literature review revealed a striking absence of discourse on the possible role of unintended cation introduction during graphene transfer. Moreover, while prior literature has lauded the high selectivity ratios linked with graphene, recent studies, including this one, suggest that the previously reported high isotopic selectivity values might be influenced more by catalysts and the overlooked presence of alternate cations from proton/deuteron, rather than graphene alone.

Central to this research is the hypothesis that the challenges in reproducing previously reported high H/D selectivities stem from methodological inconsistencies. As such, an integral objective of this study was to develop a reliable, reproducible pro-

cedure for evaluating CVD graphene-deposited PEMs. Time-dependent studies were conducted using a custom-built Online Electrochemistry Mass Spectrometry (OEMS) system to discern whether the observed selectivity was transient or permanent and to address direct separation of H and D from feed mixtures of H_2 and D_2 rather than independent observations of cell currents and H vs D transport rates from cells with feeds of only H_2 and D_2 that were not mixed.

The findings presented in this dissertation provide insights into the roles of unintentionally introduced cations in hydrogen isotope separation and suggest a refined methodological approach for future research in this domain. This work contributes to the ongoing discourse about CVD graphene's role in electrochemical hydrogen isotope separation, highlighting the value of a comprehensive and thorough scientific approach.

Keywords: Hydrogen Isotope Separation, Proton Exchange Membranes, OEMS, CVD graphene, Nafion, Cation Exchange.

Dedication

This work is dedicated to the cherished memories of Ariyapala Fernando and Yasawathi Fernando, whose lessons and love shaped my journey.

Acknowledgments

First and foremost, I wish to express my profound gratitude to my advisor, Prof. Stephen Creager, whose wisdom, guidance, and unwavering support have been pivotal throughout this research journey. Working under your mentorship has been both an honor and a privilege, one that I will cherish throughout my career.

I would also like to extend my appreciation to my committee members: Prof. Ken Marcus, Prof. George Chumanov, and Dr. Steve Xiao. Their feedback and academic perspectives have been invaluable in refining this dissertation and enhancing my academic growth.

My sincere thanks go to our research collaborators at SRNL and Vanderbilt University. The collaboration enriched our work and provided valuable perspectives that significantly elevated the quality of our research.

I am grateful to the Department of Energy (DOE) for their financial support, which was essential in carrying out this research.

On a personal note, my profound gratitude goes to my wife, Thashmi Maneesha, whose unwavering love, patience, and support have been my bedrock throughout this journey. To my parents, Shiromi Priyadarshani and Upul Pushpakumara, and my brothers, Lahiru Umesh and Shanu Heshan, your faith in me and your constant encouragement have been my guiding light. Your belief in my potential has been the wind beneath my wings.

I also want to acknowledge my former group members, Dr. Saheed Bukola, Bryan Bill, Kyle Beards, and Mansour Saberi, whose friendship, shared experiences, and insights have enriched both my research and my time at Clemson.

A special shoutout to Tony Slapikas, whose knowledge was instrumental in setting up the QMS, and whose guidance has been essential in setting up and navigating the intricacies of our research equipment.

Dr. Haijun Qian, your expertise during the EDX and SEM imaging sessions at the Clemson Electron Microscope Laboratory was invaluable.

Lastly, I'd like to thank the Department of Chemistry at Clemson. Being a part of this Ph.D. program has been a transformative experience. The conducive academic environment, coupled with the immense support from faculty and peers alike, has made this journey both challenging and fulfilling.

To everyone mentioned and many others who have been a part of this journey: Thank you. Your contributions, both big and small, have culminated in the realization of this dissertation.

Table of Contents

List of Tables

List of Figures

Chapter 1

Introduction

1.1 Background

As nuclear fusion reactors relying on the efficient production of stable hydrogen isotopes, deuterium and tritium emerge as potential solutions for looming energy crises, the importance of hydrogen isotope separation escalates[1][2][3]. Beyond its role in energy production, deuterium's particular use in isotope tracing, nuclear magnetic resonance spectroscopy, as neutron moderators in nuclear reactors, and in medical applications emphasizes the depth and range of its significance across both scientific research and industrial domains[4][5]. Over the years, a multitude of techniques for separating hydrogen isotopes have been developed. These include traditional methods such as cryogenic distillation[6] and the Girdler-Sulfide process[7]. These techniques often require substantial energy inputs and sophisticated infrastructure, posing significant limitations in terms of cost-efficiency and scalability[8].

Against this backdrop, membrane-based separation methods have emerged as a promising alternative. This approach, based on the use of proton exchange membranes (PEMs), a material that facilitates proton movement while inhibiting the mi-

gration of electrons to separate isotopes, is appreciated for its relative simplicity, lower energy demands, and potential for scaling[9]. Recent advancements in nanomaterials have further propelled research interest in this field. Notably, graphene, a single layer of carbon atoms arranged in a two-dimensional honeycomb lattice, has captured the scientific community's attention due to its exceptional electrical, mechanical, and thermal properties[10]. Notably, the inclusion of graphene within PEM membranes specifically Nafion membranes has been explored due to graphene's reported selective permeability towards hydrogen isotopes[9][11][12].

However, as with any burgeoning field of research, the integration of graphene into PEMs and its implications on hydrogen isotope separation are not without complexities and ambiguities[13]. While the promise of graphene-enhanced PEMs is tantalizing, it is imperative to dissect and understand the complexities, gaps, and potential misconceptions that might cloud our understanding of this sophisticated interplay between materials science and electrochemistry. By diving into this intricate landscape, this dissertation aims to clarify on the potentialities, challenges, and enigmas surrounding hydrogen isotope separation in Proton Exchange Membranes, laying the groundwork for future innovations and technological advancements.

1.2   Research Context

The journey of understanding hydrogen isotope separation within graphene-integrated PEMs is rich and multidimensional, having evolved over the years as technology and knowledge advanced[9][10][11][12][13][14][15]. The research landscape has been shaped by multitude explorations, innovations, and questions, some of which remain unanswered.

1.2.1 State of Knowledge

Initial investigations into hydrogen isotope separation within PEMs highlighted the transformative potential of this approach. With the introduction of graphene into the equation, excitement in the scientific community reached new heights. Early studies, particularly those analyzing monolayers of exfoliated graphene, reported a H/D separation factor of 10[11], suggesting that graphene's unique structure and properties could enhance isotope selectivity within PEMs. The major disadvantage of exfoliated graphene is that it is not scalable, prompting scientists to turn to Chemical Vapor Deposition (CVD) as a more viable technique for large-scale production of high-quality graphene. This culminated in a series of studies that extensively explored the deposition of CVD graphene onto Nafion, further emphasizing the synergistic benefits. In 2017, Lozado-Hidalgo and colleagues demonstrated that a CVD graphene-embedded Nafion membrane could effectively differentiate between hydrogen isotopes, achieving a separation factor of around 8 despite cracks and imperfections in graphene[12]. Building on this, Bukola et al. in 2018 achieved a separation factor of roughly 14 using Nafion — Graphene — Nafion sandwich membranes in an electrochemical pump cell while acknowledging similar imperfections in the graphene layer[9].

However, as with any evolving domain of scientific inquiry, subsequent research has brought forth a mix of corroborations and contradictions. The work of Xue et al. (2022) stands out in this context, presenting a counternarrative that challenges the previously accepted prominence of CVD graphene in determining H/D selectivity. Their findings underscored the influence of catalysts, suggesting that they play a more vital role than graphene in the selectivity process[13].

1.2.2 Research Gaps and Challenges

Despite the comprehensive research conducted to date, notable gaps and challenges persist. A glaring omission from current literature is the consideration of unintentional cation introduction during the graphene transfer process onto Nafion membranes. The implications of exchanged cations in the PEM, particularly ammonium and copper, remain completely unexplored in the domain of graphene-integrated PEMs, presenting a potential blind spot in our understanding of their impact on hydrogen isotope separation.

Moreover, the methodologies employed to assess graphene-deposited PEMs vary significantly across studies. The absence of a standardized, reproducible procedure to prepare graphene-integrated Nafion membranes has led to inconsistent findings, incorrect control experiments. This inconsistency is further exacerbated by the lack of time-dependent studies which would provide insights into the long-term efficacy reported isotopic separation and stability of these graphene-embedded Nafion membranes.

Lastly, the discourse's prevailing ambiguity surrounding the exact role and impact of graphene in PEMs, as evidenced by the conflicting findings of multiple studies, signifies the need for further systematic, unbiased, and in-depth investigation.

In conclusion, despite preliminary investigations into hydrogen isotope separation in CVD graphene-integrated PEMs, the domain remains characterized by notable ambiguities, discrepancies, and unresolved queries. It is within this context of established knowledge and existing gaps that the present dissertation situates itself, aiming to untangle complexities and pave the way for a clearer, more holistic understanding of the subject.

1.3 Research Motivation and Aims

1.3.1 Motivation

The advancement of knowledge in academia has historically oscillated between important discoveries and inherent challenges. Nowhere is this more evident than in the field of hydrogen isotope separation within graphene-integrated PEMs. The prevailing research presents a blend of key discoveries alongside areas that remain clouded in ambiguity. This duality forms the underpinning for our present inquiry.

The ongoing discourse on hydrogen isotope separation in PEMs, particularly in relation to the influence of graphene, reveals a split in findings. Initial research highlighted the promising potential of graphene, emphasizing its role in H/D separation[12]. However, subsequent investigations by Xue et al. (2022) presented contrasting views[13]. A perplexing element in this discourse is how isotope separation has been achieved by various researchers, even when acknowledging cracks and imperfections in CVD graphene. These discrepancies, exacerbated by difficulties in replicating the graphene-integrated PEM experiments conducted by a former group member, Dr. Saheed Bukola, who reported a H/D separation factor of 14[9], and the previously overlooked concern of unintentional cation introduction during graphene transfer, emphasize considerable gaps in our current understanding and underscore the need for further investigation.

1.3.2 Research Aims

- Investigating Cation Impacts: Our research aims to lead investigations into the unintentional presence and role of specific cations, namely ammonium and copper, and their potential impact on hydrogen isotope separation. These efforts

are intended to deepen our understanding of the subtleties in PEM performance.

- Evolving Standardized Evaluation Protocols: Given the diversity in existing evaluation mechanisms, our inquiry aims to curate and propose a harmonized, rigorous, and replicable assessment paradigm for graphene-integrated PEMs. Simultaneously, we wish to embark on the exploration of the long-term reliability of these separation techniques, addressing an evident gap in the literature.

- Temporal Assessment: A key facet of our study encompasses time-anchored evaluations to discern the persistence of observed selectivity—whether it remains transient or establishes permanence.

- Reassessing Graphene's Functionality: Amidst the array of interpretations, it becomes imperative to rigorously reevaluate graphene's efficacy and role in the hydrogen isotope separation spectrum within PEMs. Through meticulous examinations of pristine Nafion Graphene (NGN) membranes, we aim to present a holistic and grounded perspective on graphene's utility.

The present study intends to build on and challenge the current discourse on hydrogen isotope separation in PEMs, with a particular focus on the potential roles of graphene and introduced cations. Our study will be the first to specifically address the issue of unintentional cation introduction during graphene transfer. Furthermore, we aim to develop a reliable and reproducible method of evaluating graphene-deposited PEMs, thus addressing a significant gap in current research methodologies. In doing so, we hope to provide a more accurate understanding of hydrogen isotope separation within PEMs, correct misconceptions, and fill gaps in the current literature.

1.3.3 Anticipated Contributions

This research transcends mere academic exploration, poised to offer transformative insights. Through rigorous evaluations of graphene's contributions and the potential ramifications of inadvertent cation introductions, we anticipate furnishing the academic community with enhanced clarity and direction. Our endeavors also seek to harmonize prevailing research methodologies, fostering cohesiveness in future empirical studies. It is our aspiration that this comprehensive inquiry not only elucidates current understandings but also charts an informed trajectory for forthcoming studies within the domain.

1.4 Methodological Overview

The complexity and multifaceted nature of hydrogen isotope separation in PEMs require an interdisciplinary approach that straddles the boundaries of traditional scientific domains. This dissertation champions such an approach, merging insights and techniques from a range of scientific disciplines to offer a richer, more holistic understanding of the subject.

- Electrochemistry: At the core of our investigation lies electrochemistry, a pivotal discipline that provides the fundamental principles governing the behavior and interaction of charged particles within our chosen system. Through electrochemical techniques, we've been able to scrutinize the behavior of hydrogen isotopes during various processes, giving us valuable insights into their separative characteristics.

- Mass Spectrometry: Complementing our electrochemical analyses, mass spectrometry offers an analytical tool to discern the exact composition of our sam-

ples. This method allows for precise identification of the evolved gases from electrochemical reactions, ensuring our conclusions are firmly rooted in empirical data.

- Materials Science: The introduction and evaluation of materials like graphene and Nafion in our research necessitate an understanding of materials science. By diving into the structural and compositional attributes of these materials, we're better positioned to infer their roles in the isotope separation processes.

1.5 Dissertation Structure

Navigating through this dissertation, readers will embark on a structured journey that delves into the depths of hydrogen isotope separation within graphene-integrated PEMs. Here is a concise overview of the organization of this dissertation:

Chapter 2: "Kinetic Isotope Effects in the Electrolysis of Water and Heavy Water: A Comparative Study in Different Electrolyte Environments"

An introduction to the kinetic isotope effects observed during the electrolysis of water and heavy water, focusing on the differential environments in which this phenomenon occurs.

Chapter 3: "Development and Application of a Novel Electrochemical Hydrogen Pump Cell Technique for Accurate Through-Plane Proton Conductivity Measurements of Ionomer Membranes"

This chapter unveils a novel technique designed to gauge proton conductivity within PEMs, offering readers insight into an innovative approach with the potential to reshape fuel cell technology assessments.

Chapter 4: "Mitigating the Effects of Cation Contamination in Nafion Membranes for Improved Hydrogen/Deuterium Separation in Electrochemical Hydrogen

Pump Cell Experiments"

A deep dive into the implications of cation contamination in Nafion membranes during the graphene transfer process. This chapter not only highlights the significance of considering contamination during membrane preparation but also presents a novel post-treatment process to optimize hydrogen/deuterium pump cell experiments.

Chapter 5: "Reevaluating Graphene's Hydrogen-Deuterium Selectivity: An Investigation Using Decontaminated Membranes"

Here, we challenge established beliefs by rigorously reevaluating the role of graphene in hydrogen isotope selectivity. The insights gleaned from this investigation serve to redirect current understandings and chart a new trajectory for future explorations.

Chapter 6: "Real-Time Analysis of Electrochemically Evolved Gases: Design, Operation, and Applications of an Integrated OEMS System"

This chapter presents the comprehensive design, calibration, and application of an integrated EC-MS system, showcasing its potential contributions to the analysis of gases evolving from electrochemical reactions.

Chapter 7: "Impact of CVD Graphene-Embedded Nafion Membranes on Hydrogen Isotope Selectivity"

Building on previous insights, this chapter delves into the profound impact of CVD graphene on hydrogen isotope selectivity, offering a refined and evidence-backed perspective on this critical topic.

Collectively, these chapters enhance our understanding of hydrogen isotope separation in CVD graphene-embedded PEMs, offering an extensive exploration of this vital subject. This dissertation serves not only as a document of our research but as a platform for future inquiry into the fascinating and ever-evolving field of hydrogen isotope separation.

In addition to the studies discussed above, I collaborated on a published project involving electrochemical characterization of GADIPY (dipyrrin complexes of dichlorogallate) through cyclic voltammetry for Dr. Rhett Smith from the Department of Chemistry. The citation for the manuscript is as follows:

1. Wan, W.; **Silva, M. S.**; McMillen, C. D.; Creager, S. E.; Smith, R. C., Highly Luminescent Heavier Main Group Analogues of Boron-Dipyrromethene. Journal of the American Chemical Society 2019, 141 (22), 8703-8707.

I have also collaborated on published projects involving measuring through-plane proton conductivities of PFSA nanocomposites containing silica nanoparticles with Dr. Eric Davis from Department of Chemical and Biomolecular Engineering. The citations for these manuscripts are as follows:

1. Domhoff, A.; Martin, T. B.; **Silva, M. S.**; Saberi, M.; Creager, S.; Davis, E. M., Enhanced Proton Selectivity in Ionomer Nanocomposites Containing Hydrophobically Functionalized Silica Nanoparticles. Macromolecules 2021, 54 (1), 440-449.

2. Domhoff, A.; Wang, X.; **Silva, M. S.**; Creager, S.; Martin, T. B.; Davis, E. M., Role of nanoparticle size and surface chemistry on ion transport and nanostructure of perfluorosulfonic acid ionomer nanocomposites. Soft Matter 2022, 18 (17), 3342-3357.

These publications are not discussed further in this dissertation.

References

(1) Schumacher, U. *Naturwissenschaften* **2001**, *88*, 102–112.

(2) Zhu, P.; Gastol, D.; Marshall, J.; Sommerville, R.; Goodship, V.; Kendrick, E. *Journal of Power Sources* **2021**, *485*, 229321.

(3) Causey, R.; Brooks, J.; Federici, G. *Fusion Engineering and Design* **2002**, *61-62*, 525–536.

(4) Kim, J. Y.; Oh, H.; Moon, H. R. *Advanced Materials* **2019**, *31*, 1805293.

(5) Xu, J.; Li, R.; Yan, X.; Zhao, Q.; Zeng, R.; Ba, J.; Pan, Q.; Xiang, X.; Meng, D. *Nano Research* **2022**, *15*, 3952–3958.

(6) Ellehoj, M. D.; Steen-Larsen, H. C.; Johnsen, S. J.; Madsen, M. B. *Rapid Communications in Mass Spectrometry* **2013**, *27*, 2149–2158.

(7) Andreev, B. M. *Separation Science and Technology* **2001**, *36*, 1949–1989.

(8) Gao, R.; Lin, L.; Li, Z.; Liang, Y.; Gu, W.; Yang, J.; Yan, J.; Fan, J. In *Proceedings of the 23rd Pacific Basin Nuclear Conference, Volume 2*, ed. by Liu, C., Springer Nature Singapore, pp 654–667.

(9) Bukola, S.; Liang, Y.; Korzeniewski, C.; Harris, J.; Creager, S. *Journal of the American Chemical Society* **2018**, *140*, 1743–1752.

(10) Hu, S.; Lozada-Hidalgo, M.; Wang, F. C.; Mishchenko, A.; Schedin, F.; Nair, R. R.; Hill, E. W.; Boukhvalov, D. W.; Katsnelson, M. I.; Dryfe, R. A. W.; Grigorieva, I. V.; Wu, H. A.; Geim, A. K. *Nature* **2014**, *516*, 227–230.

(11) Lozada-Hidalgo, M.; Hu, S.; Marshall, O.; Mishchenko, A.; Grigorenko, A. N.; Dryfe, R. A. W.; Radha, B.; Grigorieva, I. V.; Geim, A. K. *Science* **2016**, *351*, 68–70.

(12) Lozada-Hidalgo, M.; Zhang, S.; Hu, S.; Esfandiar, A.; Grigorieva, I. V.; Geim, A. K. *Nature Communications* **2017**, *8*, 15215.

(13) Xue, X.; Chu, X.; Zhang, M.; Wei, F.; Liang, C.; Liang, J.; Li, J.; Cheng, W.; Deng, K.; Liu, W. *ACS Applied Materials amp; Interfaces* **2022**, *14*, 32360–32368.

(14) Yasuda, S.; Matsushima, H.; Harada, K.; Tanii, R.; Terasawa, T.-o.; Yano, M.; Asaoka, H.; Gueriba, J. S.; Diño, W. A.; Fukutani, K. *ACS Nano* **2022**, *16*, 14362–14369.

(15) Bukola, S.; Beard, K.; Korzeniewski, C.; Harris, J. M.; Creager, S. E. *ACS Applied Nano Materials* **2019**, *2*, 964–974.

Chapter 2

Kinetic Isotope Effects in the Electrolysis of Water and Heavy Water: A Comparative Study in Different Electrolyte Environments

2.1 Abstract

This study undertakes a comprehensive exploration of the impact of isotopic substitution on the kinetics of the Hydrogen Evolution Reaction (HER), Deuterium Evolution Reaction (DER), and Oxygen Evolution Reaction (OER) in acidic mediums. Experiments were conducted in two distinct electrochemical environments: regular water (H_2O) and heavy water (D_2O). Utilizing both three-electrode and two-electrode systems, we observed distinct reaction dynamics in these environments. Results indicated that both HER and DER operate under the Volmer-Heyrovsky mechanism, emphasizing the role of electrochemical desorption in hydrogen and deu-

terium evolution. Notably, a more pronounced overpotential difference was observed for OER in H_2O versus D_2O than between HER and DER at a given current density, highlighting the significant influence of the kinetic isotope effect on the OER's energy barrier. These findings have profound implications for the optimization of electrochemical systems, particularly in the domain of isotope separation and energy conversion technologies. The insights from this study serve as a foundation for advancing both theoretical understanding and practical applications in electrochemistry.

2.2   Introduction

The escalating global demand for energy, coupled with the urgent need to transition from fossil fuels to sustainable energy resources, has highlighted the critical importance of energy conversion and storage technologies[1][2][3][4]. Among various strategies, a particularly promising technique that has surfaced is the electrochemical splitting of water, a process that facilitates the transformation of electrical energy into chemical energy stored within hydrogen[4][5]. Hydrogen, an energy carrier par excellence, can be efficiently converted back into electricity in fuel cells, offering the prospect of a closed-loop, carbon-neutral energy cycle[6]. Moreover, hydrogen is a versatile chemical feedstock that has significant roles in various industrial processes, thereby making its generation via water splitting an essential aspect of the global sustainable energy landscape[7].

The application of water electrolysis also extends beyond clean energy generation. An intriguing and important facet of this process is the separation of hydrogen isotopes. Hydrogen has two stable isotopes, protium (H) and deuterium (D), the latter of which is used extensively in scientific research, nuclear power, and various industrial applications[8]. The efficient separation of these isotopes is therefore of

high value.

Water electrolysis involves two half-cell reactions: the HER at the cathode and the OER at the anode[7]. Despite the seemingly straightforward nature of these reactions, they encompass complex multi-electron-transfer processes that proceed via intricate intermediate species and pathways. Given their inherently slow kinetics, these reactions are typically accelerated by catalysts, with Platinum (Pt) and Iridium Oxide (IrO_2) recognized as the state-of-the-art for HER and OER, respectively[6]. While offering superior catalytic activity and stability, these materials are also associated with high costs. Consequently, extensive research has been dedicated to the design and synthesis of efficient, cost-effective catalysts[9][10][11][12][13].

Advancing water electrolysis systems necessitates not just superior catalysts but also an in-depth understanding of the intrinsic reaction mechanisms and kinetics. For instance, HER and OER proceed via specific pathways: the Volmer-Tafel or Volmer-Heyrovsky mechanisms in HER[14] and the formation of various surface-bound intermediate species in OER[6]. The overall kinetics of these reactions are dictated by the rate-determining step, the stage with the highest activation energy barrier.

The objective of this study is to investigate the KIEs in water and heavy water electrolysis in both liquid and solid electrolyte environments using a three-electrode cell with reference electrode to reveal the degree to which kinetic selectivity for H_2O vs D_2O electrolysis resides at the HER or OER electrode. We aim to highlight the isotopic effects at both the anode and cathode reactions and understand their implications on the overall isotope separation process. The insights from this study may serve to enhance the efficiency of hydrogen isotope separation and further our understanding of the fundamental processes involved in water electrolysis.

15

2.3 Materials and Methods

2.3.1 Catalyst Preparation

For this investigation, we carefully prepared the catalysts to ensure optimal catalytic performance. Drawing from a previously published procedure[10], we prepared the anode ink by mixing 25 mg of IrO_2 (FuelCellStore) with 152 μL of a 5 wt% Nafion solution (FuelCellStore), 1 mL of deionized water, and 3 mL of isopropyl alcohol. The cathode ink was prepared in a similar fashion, but with the use of 25 mg of 40% Pt on Carbon XC-72 (FuelCellStore) instead of IrO_2. These mixtures were sonicated for an hour to ensure a homogenous dispersion, resulting in a uniformly dispersed catalyst ink. We utilized Nafion as an ionomer to enhance the integrity of the catalyst layer, and chose isopropanol for its quick evaporation property, assisting in the drying process.

2.3.2 Electrode Preparation

The working electrodes for the three-electrode cell experiments were prepared using the catalyst inks described above. The process involved depositing the catalyst ink onto glassy carbon electrodes via direct casting. Precisely, a 5 μl volume of the catalyst ink was pipetted onto the polished surface of the glassy carbon electrode, which was then left to dry at room temperature. The loaded catalyst layer's thickness was kept constant across all the electrodes to maintain uniformity. (Active surface area of approximately 0.071 cm^2) It is noteworthy that this is the geometric area, and the actual active surface area might be significantly larger due to the nano-structured catalysts' high surface area-to-volume ratio. Nonetheless, the geometric surface area provided a reasonable basis for comparison across different experiments.

2.3.3 Electrochemical Experiments

We conducted electrochemical experiments using a three-electrode cell configuration, comprising a reversible hydrogen electrode (RHE, Gaskatel, HydroFlex) as the reference electrode (RE), a platinum wire as the counter electrode (CE), and our prepared catalyst-coated glassy carbon as the working electrode. For HER and OER, we utilized 0.2 M H_2SO_4 in H_2O as the electrolyte, while 0.2 M D_2SO_4 in D_2O was employed for DER and OER. We recorded polarization curves using PineResearch's WaveDriver 20 potentiostat with a scan rate of 5 mV/s, under ambient temperature and pressure conditions. All the potentials in three-electrode experiments were recorded with respect to the RHE.

For the two-electrode water and heavy water electrolysis, a proton-exchange membrane water electrolyzer (PEMWE) was assembled using a membrane electrode assembly (MEA). The MEA was composed of a 0.5 mg/cm^2 platinum electrode (Pt on C cloth, Pt/C) and a 2 mg/cm^2 iridium oxide electrode (IrO_2 on C cloth, IrO_2/C) affixed to two Nafion 211 membranes via a hot-press method (140 °C and 600 psi). The active area of the electrode was 0.49 cm^2. This MEA was then integrated into a custom-built, swage-style PEMWE that used titanium rods as current collectors. Both regular water and heavy water were fed through designated inlets using a peristaltic pump at a pump speed of 4 ($\sim$0.1 mL/s). Figure 2.1 shows how the rate of water varied with pump speeds.
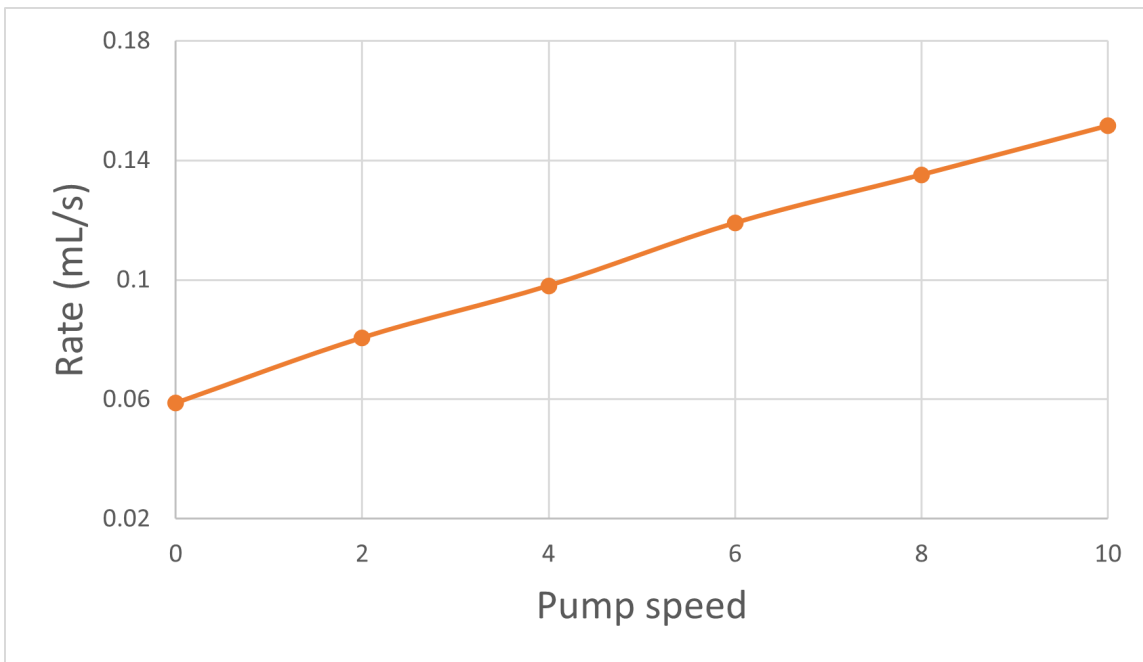
Figure 2.1: Actual water flow rates measured at various peristaltic pump speeds.

2.4 Results and Discussion

2.4.1 Hydrogen and Deuterium Evolution Reactions in liquid electrolytes utilizing in three-electrode cells

The central focus of our exploration in the three-electrode system was to elucidate the impact of isotopic substitution on the kinetics of the HER and OER in regular and heavy water, each contributing their unique influence on the experiment. As demonstrated in Figure 2.2, the polarization curves at the Pt/C electrode exhibited distinct variations during the HER and DER. While the initiation of both HER and DER displayed similar patterns in the low overpotential stages, a noticeable divergence was observed at higher overpotentials. Notably, HER presented higher current levels compared to DER for similar overpotentials. Our examinations revealed differences in the overpotentials for HER and DER at a current density of 10 mA/cm^2;
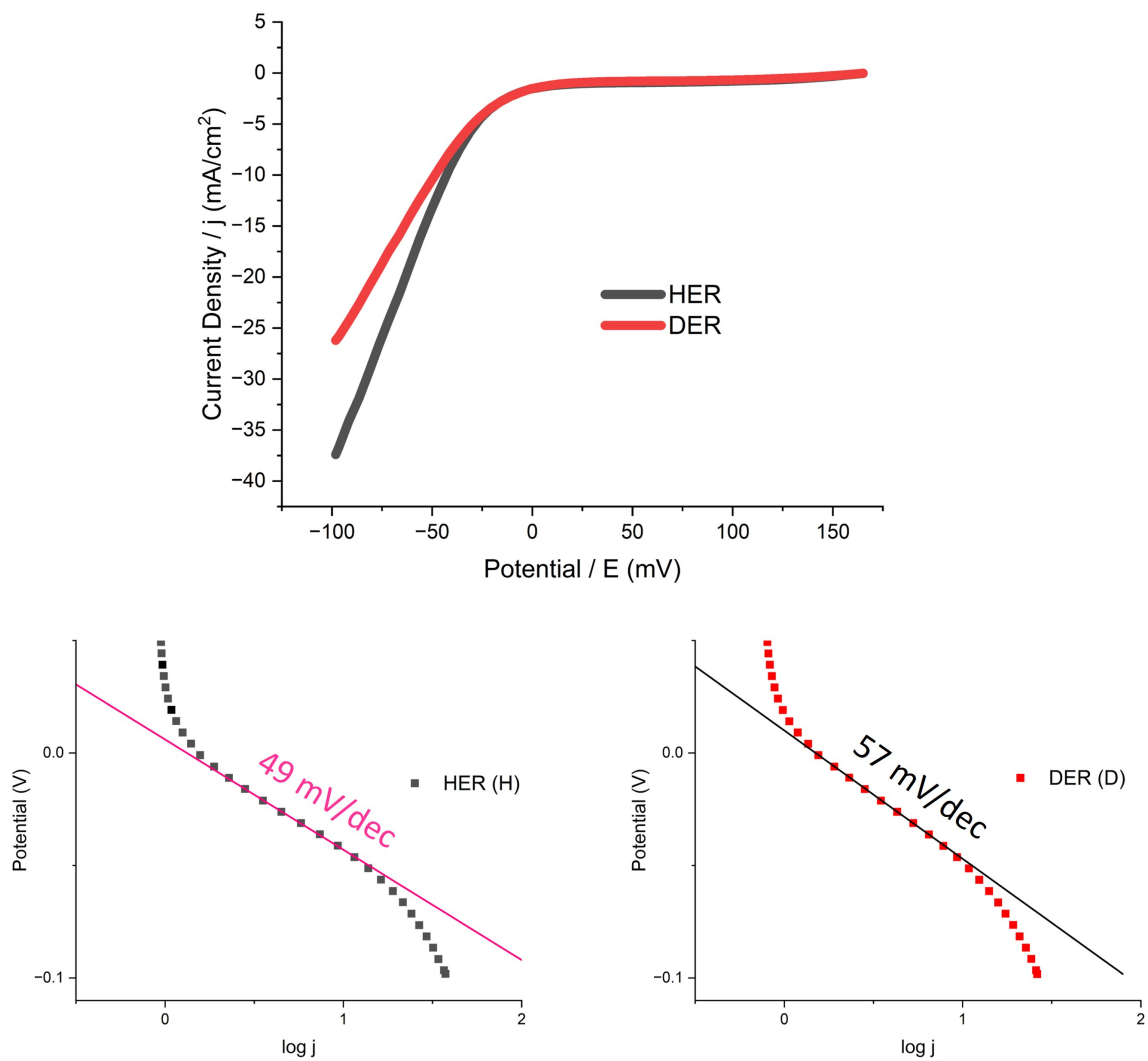
Figure 2.2: Polarization curves and Tafel plots highlighting the different electrochemical behaviors of the Hydrogen and Deuterium Evolution Reactions.

we observed 43.2 mV in the H_2SO_4 solution (0.2 M in H_2O) for HER and 48.8 mV in the D_2SO_4 solution (0.2 M in D_2O) for DER. These findings are indicative of a slightly increased energy barrier in the evolution reaction when it involved the heavier isotope, deuterium.

The Tafel slopes for the reactions, also shown in Figure 2.2, mirrored these observations. We recorded a Tafel slope of 49 mV/dec for HER and 57 mV/dec for DER, representing a difference of 8 mV/dec. The observed Tafel slope values appear to corroborate the predominance of the Volmer-Heyrovsky mechanism in both HER and DER. As shown in Figure 2.3, the concerted electrochemical reduction/desorption of hydrogen or deuterium gas is the rate-determining step in these processes. This conclusion is in harmony with the theoretical Tafel slope for HER under acidic conditions (Tafel slope of 40 mV/dec at low current densities and of 120 mV/dec at high current densities), as proposed by Prats et al., when the reaction mechanism proceeds via the Volmer and Heyrovsky steps, with the latter being rate-determining[15]. This finding reinforces the universal applicability of the Volmer-Heyrovsky mechanism in both HER and DER[16].

2.4.2 Examination of OER in H_2O and D_2O in acidic conditions Utilizing Three-Electrode Cells

We also undertook a comprehensive investigation of the OER in both H_2O and D_2O under acidic conditions. The results of this exploration are depicted graphically in Figure 2.4. The polarization curves demonstrate that OER demands greater overpotentials than HER. However, within OER, the overpotential for H_2O is notably less than for D_2O. This suggests that the reaction progresses more efficiently in H_2O. In our detailed analysis, we recorded an overpotential of 394.2 mV for OER in a
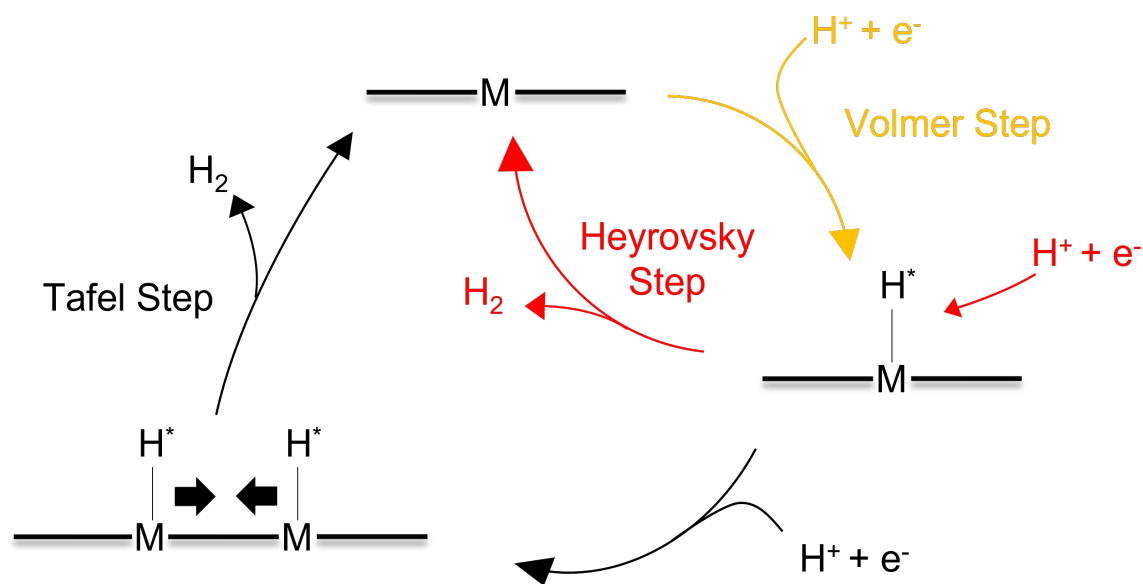
Figure 2.3: HER mechanism for acidic conditions[17]. The Volmer-Heyrovsky mechanism involves a single electron, faster Volmer step to produce a surface M-H species followed by a concerted Heyrovsky step involving a second proton reduction coupled with H-H bond separation and H_2 release.

H_2SO_4 solution (0.2 M in H_2O at a current density of 10 mA/cm^2. By contrast, we observed a much higher overpotential of 454.46 mV for OER in a D_2SO_4 solution (0.2 M in D_2O at the same current density. The distinct discrepancy observed between the overpotentials in H_2O and D_2O for OER, as compared to those of HER versus DER, emphasizes the influence of the isotopic pattern on the reaction rate for both electrode reactions.

The evidence suggests that the reaction involving D_2O is marked by a slower rate-determining step as compared to its counterpart involving H_2O. This insight underscores the profound influence of isotopic substitution on the kinetic behavior for water electrolysis.

This kinetic influence of isotopic substitution is further manifested in the distinct Tafel slopes calculated for each system. We recorded a Tafel slope of 77 mV/dec
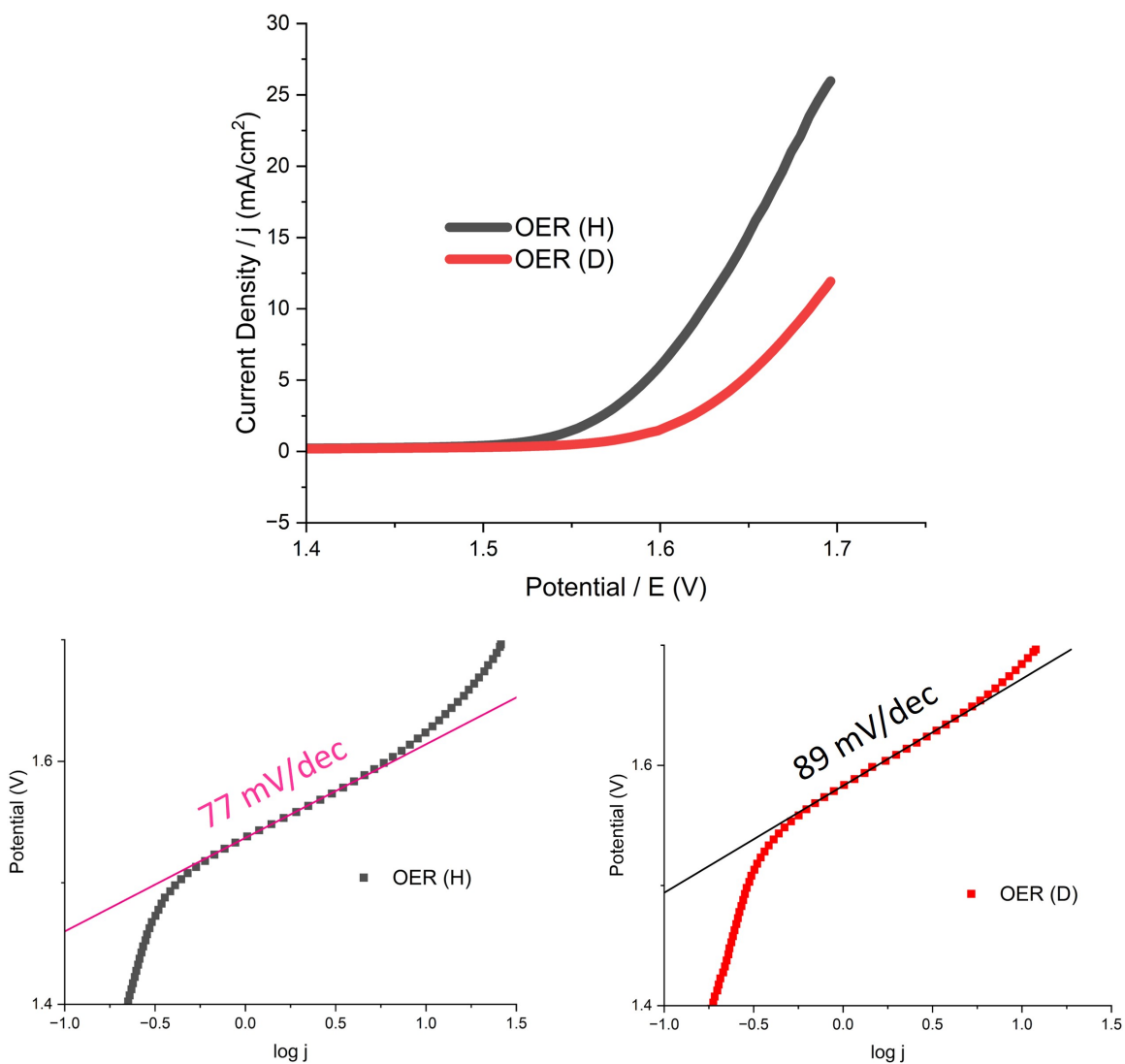
Figure 2.4: Polarization curves and Tafel plots illustrating the performance of the OER in H_2O and D_2O.

for H_2O and a relatively elevated value of 89 mV/dec for D_2O, thus demonstrating a difference of 12 mV/dec. Interestingly, this higher Tafel slope for OER in D_2O as opposed to H_2O can be directly attributed to the kinetic isotope effect. This effect arises due to the variation in zero-point energy between the isotopes, culminating in a slower reaction rate for the heavier isotope, which is D_2O in this context. The Tafel slope increase to 89 mV/decade in D_2O is due to the slower transfer of the deuteron compared to the proton, making the rate-determining step even more sluggish and thus affecting the observed Tafel slope. This type of kinetic isotope effect is a valuable tool in mechanistic studies as it provides direct evidence for the involvement of protons/deuterons in the rate-determining step. This further highlights the relationship between isotopic substitution and the kinetic behavior of electrochemical reactions.

2.4.3 Examination of Water and Heavy Water Electrolysis in PEMWE

A parallel experimental investigation was carried out to analyze water electrolysis in a PEMWE, with the results being presented in Figure 2.5. Importantly, we observed an overall higher current density for similar applied potentials in the PEMWE system compared to the three-electrode system. This disparity can be attributed to several factors, including the more efficient cell design, superior electrolyte conductivity, rapid gas diffusion, larger effective reaction area, and optimal mass transport in PEMWE. Each of these features collectively enables a PEMWE to facilitate faster reaction rates, leading to higher current densities.

Throughout these trials within the PEMWE, we noted that the overpotential required to reach a current density of 10 mA/cm^2 was 350.9 mV for regular water electrolysis, compared to a significantly higher value of 417.6 mV for heavy water
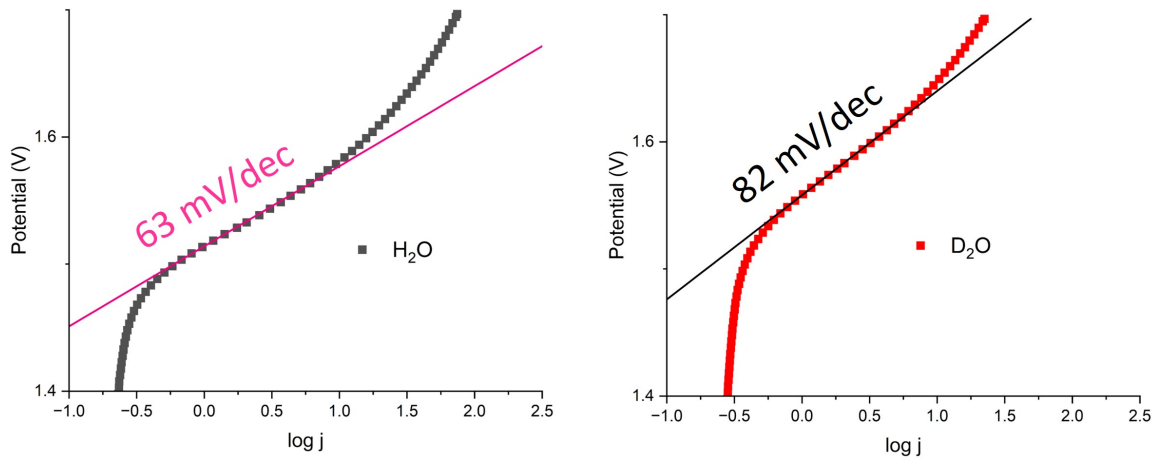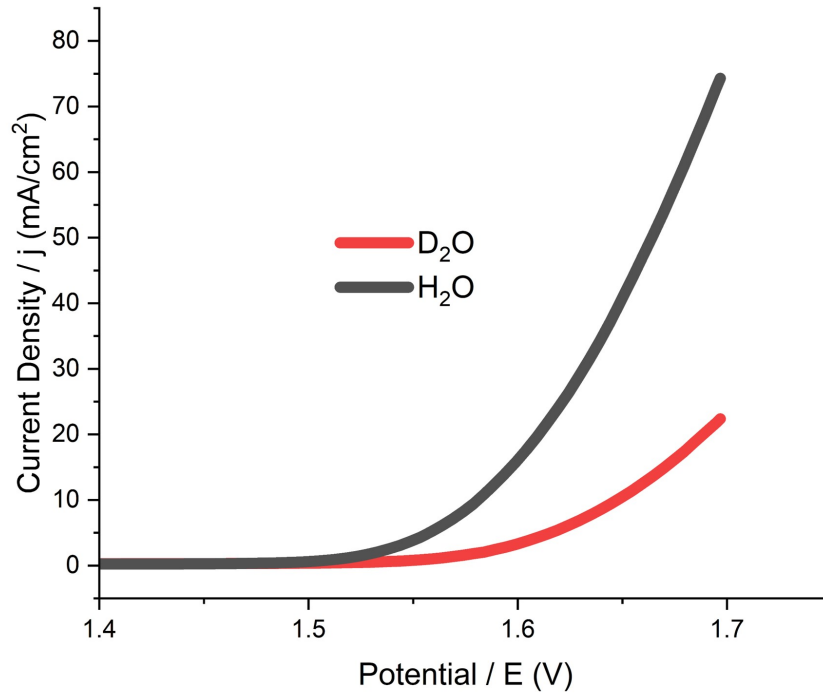
Figure 2.5: Polarization curves and Tafel plots for water and heavy water electrolysis in PEMWE.

electrolysis, suggesting a more significant energy barrier for the latter process.

Adding this understanding to our previous observations, we can conclude that the Tafel slopes, which were 63 mV/dec for H_2O and 82 mV/dec for D_2O in our PEMWE system, provide further confirmation of the influence of isotopic substitution on reaction kinetics. In particular, the steeper Tafel slope for D_2O electrolysis signifies slower kinetics, which can be traced back to the kinetic isotope effect and the associated differences in zero-point energy between hydrogen and deuterium. Notably, the Tafel slope for water electrolysis agrees with the typical Tafel slope of 60 mV/dec for commercial IrO_2 under OER in acidic conditions[11]. In our study, we observed a Tafel slope of 63 mV/dec for the OER. This value is closely aligned with the theoretical prediction from the literature, where a Tafel slope of 60 mV/dec is expected when the rate-determining step is a chemical reaction following a one-electron transfer[9].

Together, the measurements from our three-electrode and two-electrode system investigations converge to provide a comprehensive portrait of the kinetic isotope effects in water and heavy water electrolysis, paving the way for optimized isotope separation strategies and more efficient water electrolysis techniques.

2.4.4   Examination of Kinetic Isotope Effects

This observed difference in rates for light and heavy water electrolysis is indeed an exhibition of the kinetic isotope effect (KIE). The KIE is generally described as the change in the rate of a chemical reaction when one of the atoms in the reactants is replaced by one of its isotopes. In our case, replacing H with D led to a slower reaction rate for mainly OER, resulting in increased overpotentials. This can be attributed to the increased mass of deuterium. Deuterium has an atomic mass of 2.014 u, double

Figure 2.6: A condensed representation of the OER on a metal catalyst surface, denoted as 'M'[9]. While the conventional mechanism typically involves an OH* intermediate, here, we depict a direct conversion of water to the O* species for clarity of presentation. The subsequent steps, involving coordinated electron and proton transfers, culminate in the evolution of molecular oxygen.

that of hydrogen's 1.008 u. Therefore, it engages in vibrational movements at a reduced frequency upon forming bonds with other atoms, compared to when protium forms analogous bonds. This reduction in vibrational frequency consequently induces a deceleration in the reaction rates when deuterium is a constituent. Additionally, the bonds involving deuterium exhibit a lower zero-point energy which results in a higher activation energy required for bond cleavage compared to those involving hydrogen[8]. Zero-point energy refers to the minimum amount of energy that a quantum mechanical physical system may possess. Essentially, this means that heavier isotopes, such as deuterium, possess a lower zero-point energy than lighter isotopes like hydrogen. This difference in zero-point energy leads to heavier isotopes exhibiting slower reaction rates because they must overcome a greater energy barrier to react.

Therefore, in the case of our PEMWE system, the slower kinetics for the OER in D_2O can be largely attributed to the rate-determining step of the OER, which involves the breaking of the O-H bonds in H_2O or the stronger O-D bonds in D_2O. Given that the O-D bond is stronger due to its lower zero-point energy, it requires more energy to break, thereby necessitating a higher overpotential to achieve the same current density during the OER in D_2O

The notable differences in overpotential for H_2O and D_2O electrolysis suggest that the anodic (OER) reaction is more significantly affected than the cathodic (HER) reaction by hydrogen isotope substitution. The substantial impact may be attributed to the OER being a four-electron process, which involves breaking O-H/O-D bonds, a process that is particularly influenced by isotopic substitution due to the kinetic isotope effect. This suggests that in the pursuit of enhanced hydrogen isotope separation via water electrolysis, there may be great promise in optimizing anodic, and to a lesser extent, cathodic materials. These findings highlight important avenues for future research aiming to develop more efficient isotope separation techniques, indi-

cating a particular focus on the improvement and optimization of anode materials might provide substantial gains in efficiency.

2.4.5 Implications and Potential Applications

The findings of this study significantly contribute to our understanding of the role played by anode and cathode in heavy water electrolysis and hence, in hydrogen isotope separation. The implications of our study are far-reaching, not only enriching the current scientific understanding of the kinetics of electrochemical reactions in isotope-rich environments, but also potentially paving the way for impactful practical applications. Understanding these reaction dynamics is crucial for the scientific community, especially those engaged in research related to energy conversion and storage, as it can help in designing more efficient and effective electrochemical systems. Moreover, the significant differences observed in the overpotentials of H_2O and D_2O for OER and HER versus DER in different electrolysis systems underscores the substantial effect of isotopic substitution. This knowledge could be a critical factor in the design and optimization of anodic and cathodic materials in electrochemical systems. Finally, from a practical standpoint, our results have significant implications in the domain of isotope separation. Efficient isotope separation is of great interest in various fields such as nuclear energy, environmental monitoring, and biomedical research. Given the large overpotential differences observed for H_2O and D_2O electrolysis, particularly in the PEMWE system, our findings suggest that with appropriate optimization of anode materials, water electrolysis could be a promising avenue for more efficient isotope separation techniques.

2.5   Conclusion

In conclusion, this study provides valuable insights into the kinetic isotope effects in water and heavy water electrolysis. The use of both three-electrode and two-electrode (PEMWE) systems allowed for a comprehensive exploration and comparison of the reaction dynamics. Our investigations revealed that the rate-determining step in both HER and DER aligns with the Volmer-Heyrovsky mechanism, wherein the electrochemical desorption of hydrogen or deuterium is the pivotal process. Furthermore, we noted a pronounced rate difference in H_2O versus D_2O for OER as compared to HER versus DER, suggesting the kinetic isotope effect significantly influences the energy barrier of the OER. Our findings bear substantial implications for future studies, particularly those focused on designing more efficient electrochemical systems for energy conversion and storage, as well as those aiming at optimized isotope separation techniques. Our observations underscore the influence of isotopic substitution on reaction kinetics, highlighting potential optimization targets, particularly the anode materials in water electrolysis systems. In essence, this study provides new and valuable insights into the role that isotopic environments play in the kinetics of fundamental electrochemical reactions, offering a foundation for future scientific research and technological advancements in the field of electrochemistry.

References

(1) Bogdanov, D.; Ram, M.; Aghahosseini, A.; Gulagi, A.; Oyewo, A. S.; Child, M.; Caldera, U.; Sadovskaia, K.; Farfan, J.; De Souza Noel Simas Barbosa, L.; Fasihi, M.; Khalili, S.; Traber, T.; Breyer, C. *Energy* **2021**, *227*, 120467.

(2) Shiva Kumar, S.; Lim, H. *Energy Reports* **2022**, *8*, 13793–13813.

(3) Burton, N. A.; Padilla, R. V.; Rose, A.; Habibullah, H. *Renewable and Sustainable Energy Reviews* **2021**, *135*, 110255.

(4) Sebbahi, S.; Nabil, N.; Alaoui-Belghiti, A.; Laasri, S.; Rachidi, S.; Hajjaji, A. *Materials Today: Proceedings* **2022**, *66*, 140–145.

(5) Mazzeo, D.; Herdem, M. S.; Matera, N.; Wen, J. Z. *Renewable Energy* **2022**, *200*, 360–378.

(6) Wang, S.; Lu, A.; Zhong, C.-J. *Nano Convergence* **2021**, *8*, 4.

(7) Shih, A. J. et al. *Nature Reviews Methods Primers* **2022**, *2*, 84.

(8) Kopf, S.; Bourriquen, F.; Li, W.; Neumann, H.; Junge, K.; Beller, M. *Chemical Reviews* **2022**, *122*, 6634–6718.

(9) Suen, N.-T.; Hung, S.-F.; Quan, Q.; Zhang, N.; Xu, Y.-J.; Chen, H. M. *Chemical Society Reviews* **2017**, *46*, 337–365.

(10) Faustini, M.; Giraud, M.; Jones, D.; Rozière, J.; Dupont, M.; Porter, T. R.; Nowak, S.; Bahri, M.; Ersen, O.; Sanchez, C.; Boissière, C.; Tard, C.; Peron, J. *Advanced Energy Materials* **2019**, *9*, 1802136.

(11) Jin, H.; Joo, J.; Chaudhari, N. K.; Choi, S.-I.; Lee, K. *ChemElectroChem* **2019**, *6*, 3244–3253.

(12) Wu, H.; Wang, Y.; Shi, Z.; Wang, X.; Yang, J.; Xiao, M.; Ge, J.; Xing, W.; Liu, C. *Journal of Materials Chemistry A* **2022**, *10*, 13170–13189.

(13) McCrory, C. C. L.; Jung, S.; Ferrer, I. M.; Chatman, S. M.; Peters, J. C.; Jaramillo, T. F. *Journal of the American Chemical Society* **2015**, *137*, 4347–4357.

(14) Skúlason, E.; Karlberg, G. S.; Rossmeisl, J.; Bligaard, T.; Greeley, J.; Jónsson, H.; Nørskov, J. K. *Physical Chemistry Chemical Physics* **2007**, *9*, 3241–3250.

(15) Prats, H.; Chan, K. *Physical Chemistry Chemical Physics* **2021**, *23*, 27150–27158.

(16) Kichigin, V. I.; Shein, A. B. *Journal of Electroanalytical Chemistry* **2020**, *873*, 114427.

(17) Walter, C.; Menezes, P. W.; Driess, M. *Chemical Science* **2021**, *12*, 8603–8631.

Chapter 3

Development and Application of a Novel Electrochemical Hydrogen Pump Cell Technique for Accurate Through-Plane Proton Conductivity Measurements of Ionomer Membranes

3.1   Abstract

This study presents a novel approach to measuring proton conductivity in Polymer Electrolyte Membranes (PEMs), with specific emphasis on Nafion N117, N211 and N212 membranes commonly utilized in fuel cells. The method combines Linear Sweep Voltammetry (LSV) and corrected resistance analysis to accurately

measure steady-state DC currents and through-plane proton conductivity. A distinct feature of this approach is its capacity to compensate for contact resistance without necessitating a 4-point probe cell, thereby streamlining the procedure, and improving its accessibility. In the experimental validation, we demonstrated that this method not only aligns with the established ranges for proton conductivity but also reveals the relationship between resistance and membrane thickness. This approach allowed for an in-depth understanding of the electrochemical properties of the membranes, paving the way for the strategic utilization of Nafion membranes in fuel cells and related device applications. The novel method's utility extends beyond fuel cells; it was also employed to assess proton conductivity in PEMs synthesized for use in vanadium flow batteries by a separate research group. This diversified application further validates the versatility and potential of our novel method. This study has the potential to significantly impact the field of fuel-cell technology, providing a precise, accessible, and cost-effective method for assessing PEMs. Future research should explore its applicability in other electrochemical systems, thereby expanding its scope and paving the way for further refinements and improvements.

3.2 Introduction

Ionomer membranes play a crucial role in the functioning of fuel cells, particularly in Proton Exchange Membrane Fuel Cells (PEMFCs), which are prominent in several applications ranging from portable electronics to automotive power systems. While there have been developments in various alternate polymer membranes, Nafion remains a reference point and is often used as a standard for comparison[1][2][3]. These membranes serve as the centerpiece of the cell, facilitating the transfer of protons from the anode to the cathode, while also providing a barrier to separate the

reactant gases[4]. The study of proton transport, which has been a topic of interest for over a century due to its significance in chemical and electrochemical systems. The proton's mobility is notably greater than other similarly sized ions, largely due to the Grotthuss mechanism. This mechanism emphasizes that proton transport relies more on the swift formation of hydrogen bonds between hydronium ions and water molecules rather than the slower collective migration of hydronium ions, known as the vehicular mechanism[5]. Therefore, the accurate measurement of proton conductivity is paramount.

Proton conductivity, a measure of a material's ability to conduct protons, is a defining characteristic of ionomer membranes. Its accurate measurement is pivotal in evaluating the performance and efficiency of fuel cells. As the performance of a fuel cell depends directly on the rate at which protons can move through the membrane, it follows that higher proton conductivity generally translates to higher cell efficiency[6]. In the pursuit of measuring proton conductivity, Electrochemical Impedance Spectroscopy (EIS) has emerged as a highly regarded and most common method[7][8][9][10][11][12]. In addition, Giffin et al. have employed an alternate method known as broadband electric spectroscopy (BES). This technique offers the distinctive advantage of distinguishing between the bulk and interfacial conductivity of polymer membranes, as well as polymer membranes that incorporate organic fillers[13].

Through-plane proton conductivity is a critical parameter for assessing the performance of ionomer membranes in fuel cells, but its measurement presents significant challenges. Most conventional methods primarily measure in-plane conductivity due to the inherent configuration and geometry of these techniques, which do not reflect the actual working conditions in a fuel cell. The through-plane conduction, which is integral to the operation of the fuel cell, can differ substantially from the in-plane

34

conduction due to the anisotropic nature of the ionomer membranes. Thus, measurements that exclusively focus on in-plane conductivities may lead to an inaccurate representation of the overall membrane performance[1][6][14].

Another key challenge is the accounting of cell resistance in traditional measurement techniques. Cell resistance, including electrode-membrane contact resistance and any resistance introduced by the measurement apparatus, can substantially influence the observed proton conductivity, thereby leading to overestimations or underestimations of the actual value. Most traditional techniques require complex correction procedures or sophisticated four-point probe cells to account for these resistances, adding to the intricacy and potential sources of error in the measurement process[10].

Moreover, traditional methods often involve the use of alternative current (AC) techniques, such as EIS, which necessitates the use of equivalent circuit models to interpret the data[7]. These models often involve assumptions that may not hold under all conditions, particularly for complex ionomer membranes, leading to possible inaccuracies in the derived proton conductivities.

Furthermore, these AC-based methods are unable to distinguish between protonic and electronic conduction or the presence of other ions, thus the derived conductivity values may not represent pure proton conductivity. This can be particularly problematic when evaluating novel ionomer membranes with added functionalities, where additional conductive species may be present[14]. Therefore, the development of a method that accurately measures through-plane proton conductivity and effectively accounts for cell resistance, while circumventing the shortcomings of traditional techniques, is a key step towards more reliable and accurate characterization of ionomer membranes.

To address the challenges identified in conventional methods and to enable

accurate through-plane proton conductivity measurements, this work introduces a novel technique utilizing a miniaturized electrochemical hydrogen pump cell. This innovative method is specifically designed to overcome the limitations of traditional techniques and offers several advantages that make it a reliable tool for evaluating the performance of ionomer membranes in fuel cells. One of the most compelling features of this method is its ability to measure through-plane resistance, which in turn provides a pathway for determining through-plane proton conductivity. Through-plane conductivity is particularly significant as it is a crucial factor affecting the efficiency of ionomer membranes in fuel cells. By facilitating this measurement, the novel technique allows for a more comprehensive evaluation of membrane performance under conditions that closely resemble real-world fuel cell operations.

This method also implements a reliable approach to account for cell resistance without requiring a complex four-point probe cell, thereby simplifying the measurement process. By using the electrochemical hydrogen pump cell, cell resistance can be accurately measured and subtracted from the total resistance, ensuring that the derived proton conductivity values are not influenced by extraneous resistances. Additionally, the novel technique emphasizes the measurement of steady-state direct current (DC) instead of AC. This allows the method to bypass the need for equivalent circuit assumptions, which are often a source of inaccuracies in AC-based techniques. Lastly, this method is tailored to measure pure proton conduction, effectively filtering out any potential interference from other ions or electronic conduction. This is particularly useful when studying novel ionomer membranes with additional functionalities, as it ensures the measured conductivity is representative of proton conduction alone. The new method thus addresses the major challenges of traditional proton conductivity measurement techniques, opening up new avenues for accurate, reliable, and uncomplicated assessment of ionomer membranes in fuel cells.

3.3 Materials and Methods

3.3.1 Preparation of Electrodes and Membranes

Prior to use, all the proton exchange membranes selected for this study (Nafion N117, N211, and N212) underwent a pre-treatment process as detailed in subsection 3.1 of Chapter 4. This involved immersion in a 3% H_2O_2 solution, heated to 80°C, for a one-hour duration. Subsequent to this, the membranes were briefly rinsed with deionized water (DI water). An acid treatment ensued, where the membranes were submerged in a 0.5 M H_2SO_4 solution, also at 80°C, for an additional hour followed by a final rinse with DI water. The Pt/C gas diffusion electrodes (GDEs) used, featuring a platinum catalyst loading of 2 mg/cm^2, were sourced from Fuelcellstore. Sandwiches with 1, 2, 3, and 4 layers were assembled by positioning them between the electrodes. A gentle compression was then applied using a bar clamp.

3.3.2 Cell Assembly Procedure

The membrane electrode assembly (MEA) was incorporated into a swage-style electrochemical hydrogen pump cell constructed with graphite current collectors. A conductive carbon-based adhesive was utilized to attach the GDEs to the current collectors, ensuring a reliable electrical connection. The electrodes were cut into disk shapes with areas of 0.18 cm^2 and 0.50 cm^2 respectively to avert potential edge effects. (True active area is 0.18 cm^2)

3.3.3 Experimental Operating Conditions

The experiments were conducted under meticulously controlled environmental conditions. The cell operated with humidified hydrogen gas at a flow rate of 20 SCCM,
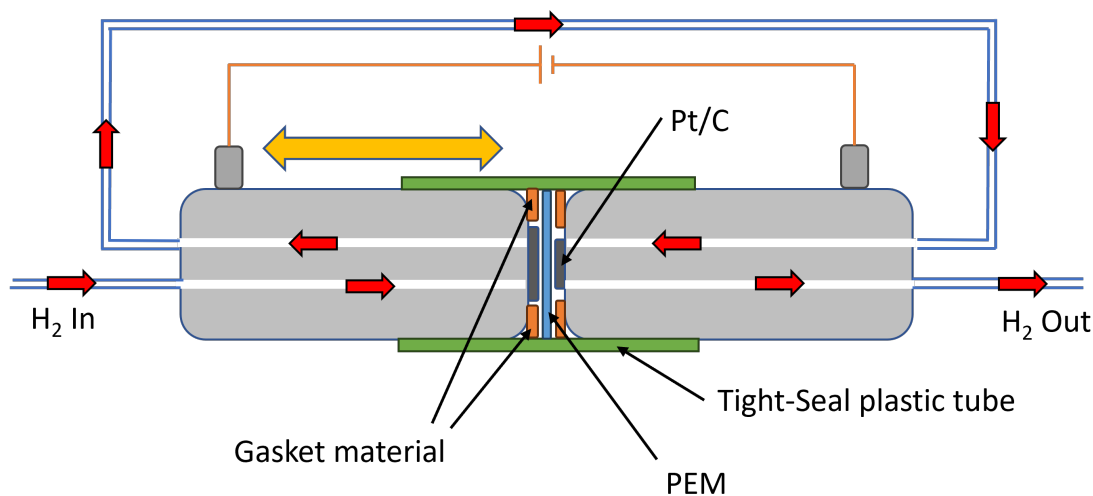
Figure 3.1: Schematic of the modified and miniaturized symmetric hydrogen pump cell. Research-grade H_2 gas, stored in a tank, was employed in this study. Prior to introduction into the cell, the H_2 gas was humidified by being bubbled through deionized water. The hydrogen pump cell was assembled in a symmetric configuration, enabling hydrogen feed from both ends. This was facilitated by the anode side outlet being connected to the cathode side inlet via a looping tube.

maintaining a relative humidity above 95% throughout the experiment. The system temperature was consistently held at ambient room temperature which is typically between 20 °C and 25 °C. For safety considerations, the hydrogen pump cell was securely housed within a fume hood.

3.3.4 Electrochemical Analysis

The electrochemical behavior of Nafion N117, N211, and N212 membranes was assessed using LSV. For this study, we varied the number of membrane layers stacked together to obtain resistance values at different thicknesses. LSV curves were generated under identical experimental conditions for all membrane configurations. The LSV tests were performed on a PineResearch WaveDriver 20 electrochemical workstation, using a voltage window from -25 mV to 25 mV at a scan rate of 1 mV/s.

3.3.5 Determination of Resistance and Proton Conductivity

The resistance of the membrane was inferred from the slope of the LSV curves, which varied according to the membrane thickness. Concurrently, the intercept of the resistance vs. membrane thickness plots yielded residual resistances, representing the sum of all contributions except those from bulk membrane resistance. The total resistance of the cell, measured experimentally, incorporated these residual resistances. To achieve a more representative depiction of the membrane resistance, we subtracted the residual resistances from the total resistance.

Subsequently, proton conductivity was computed using the corrected resistance values, adhering to Ohm's Law and taking into account the geometric dimensions of the membrane. The resultant proton conductivity values, indicated in mS/cm, provide a measure of the through-plane proton conductivity of the ionomer membrane under specified experimental conditions.

3.4 Results and Discussion

The LSV curves for Nafion N117, N211, and N212 membranes indicate a clear correlation between the number of layers and the measured resistance values, with observable distinctions among the three membrane types. Notably, an increase in the number of layers led to heightened resistance across all three membrane types (Nafion N117, N211, and N212). This trend suggests an extended path length for proton conduction due to layer augmentation, resulting in a corresponding rise in overall resistance.
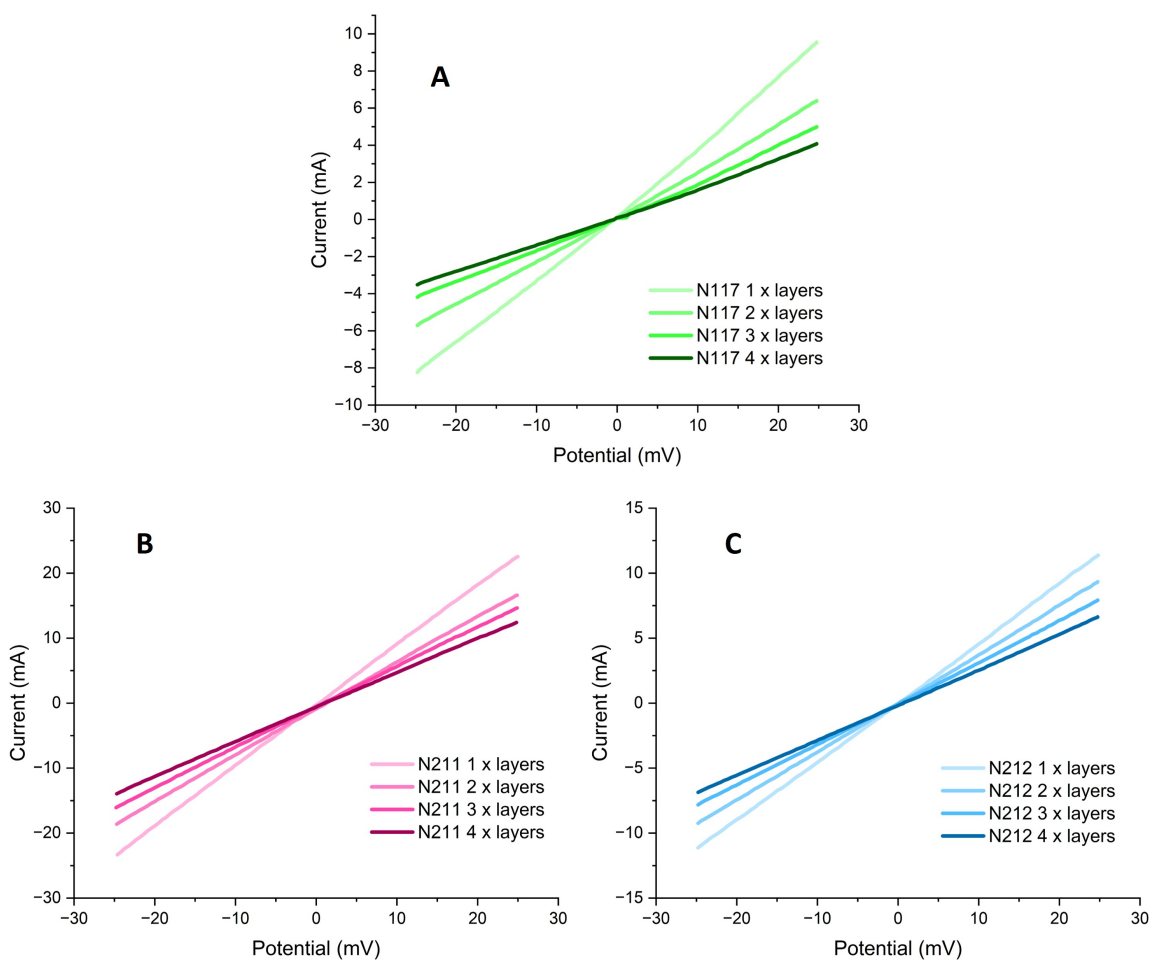
Figure 3.2: Comparative LSV plots for varying layers of Nafion N117(A), N211(B), and N212(C). These graphs illustrate the LSV curves recorded for 1, 2, 3, and 4 layers of each Nafion membrane type under identical experimental conditions in an electrochemical hydrogen pump cell.

Table 3.1: Summary of proton conductivity calculation.

Membrane Type	Number of Layers	Sample Thickness (μm)	Total Resistance (Ω)	Cell Resistance (Ω)	Corrected Resistance R (Ω)	1/R	t/A	Conductivity (mS/cm)
	1	196.5	2.80	1.53	1.27	0.79	11.04	87.2
	2	392.0	4.13	1.53	2.59	0.39	22.02	84.9
Nafion 117	3	584.5	5.46	1.53	3.92	0.25	32.84	83.7
	4	777.5	6.61	1.53	5.08	0.20	43.68	86.0
	1	27.0	1.08	0.84	0.23	4.27	1.52	64.7
	2	55.0	1.40	0.84	0.56	1.78	3.09	55.1
Nafion 211	3	82.0	1.62	0.84	0.77	1.30	4.61	59.7
	4	110.0	1.88	0.84	1.04	0.96	6.18	59.5
	1	55.0	2.20	1.67	0.53	1.88	3.09	58.2
	2	110.0	2.67	1.67	1.00	1.00	6.18	61.5
Nafion 212	3	164.0	3.17	1.67	1.50	0.67	9.21	61.5
	4	215.0	3.69	1.67	2.02	0.49	12.08	59.8

3.4.1 Corrected Resistance Analysis

3.4.2 Overview of Corrected Resistance Findings for Nafion N117, N211 and N212

Our analysis necessitated accurate measurements of the conductivity and resistance of the various membranes (Nafion N117, N211, and N212), an endeavor for which we employed a symmetric electrochemical H_2 pump. This arrangement allowed for H_2 to be fed to both electrodes simultaneously. We chose to conduct our voltage scans across the zero-voltage region, ranging from -25 mV to +25 mV. This method was selected due to the symmetrical nature of our setup, as scanning across the zero region enabled the generation of a linear curve for the IV (current-voltage) curve.

The slope of this IV curve proved to be critical, providing valuable information regarding the resistance of the membrane. We recorded the IV curves layer by layer, up to four layers, thereby obtaining four data points representing resistance versus thickness. Subsequent to recording these four data points for each membrane type, we

were able to plot Resistance vs Thickness and extrapolate these plots to zero thickness. This extrapolation granted us an estimation of the residual resistance, meaning all contributions to resistance except those to bulk ionomer membrane resistance. By subtracting this residual resistance from each data point, we could then ascertain the true resistance for each membrane.

The relationship between resistance (R), resistivity (ρ), and conductivity (κ) was governed by the formula R = ρL/A, where L represents the length and A represents the area. Rearranging this formula yielded the equation for conductivity as κ = L/RA. Given that the inverse of resistance, 1/R, represented the slope of each membrane's IV curve, and the active area was known to be 0.18 cm^2, we were able to solve for κ for each membrane. This analysis allowed us to calculate an average κ, with 95% confidence interval (CI), for each membrane type, providing crucial insights into their electrochemical behaviors. A comprehensive summary of these findings is presented in Table 3.1.

The proton conductivities of the Nafion N117, N211, and N212 membranes were calculated by employing their corrected resistance values in conjunction with their geometric properties. Among the three, Nafion N117 exhibited the highest conductivity, measuring at approximately 85 mS/cm. In contrast, both N211 and N212 showed a comparably lower conductivity, hovering around 60 mS/cm. These results underscore the intrinsic disparities in proton conductive properties between the first-generation Nafion N117 and its second-generation counterparts, N211 and N212.

As shown in Figure 3.4, Nafion 117 boasts the most substantial conductivity, approximately 85.46 mS/cm, with a 95% CI of ±2.38. This high degree of certainty in measurement underscores its robust conductivity. This obtained conductivity agrees with the recorded conductivity of 78 mS/cm for N117 using a four-electrode AC
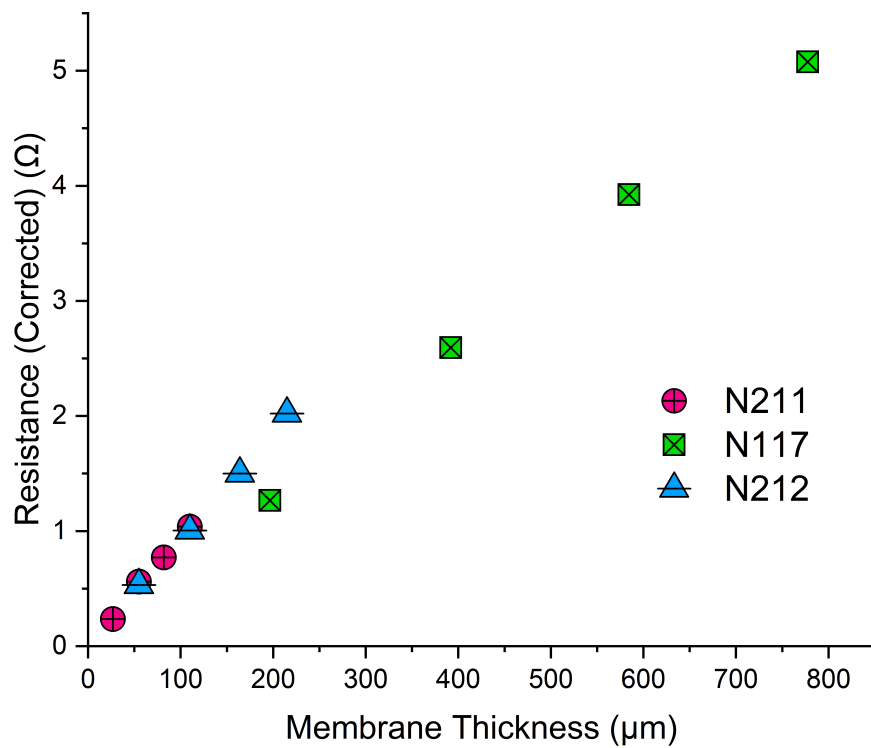
Figure 3.3: Membrane resistance (corrected) with increasing thickness/layers. The membrane's real resistance was calculated from cell/residual resistance subtracted from the total resistance measured.
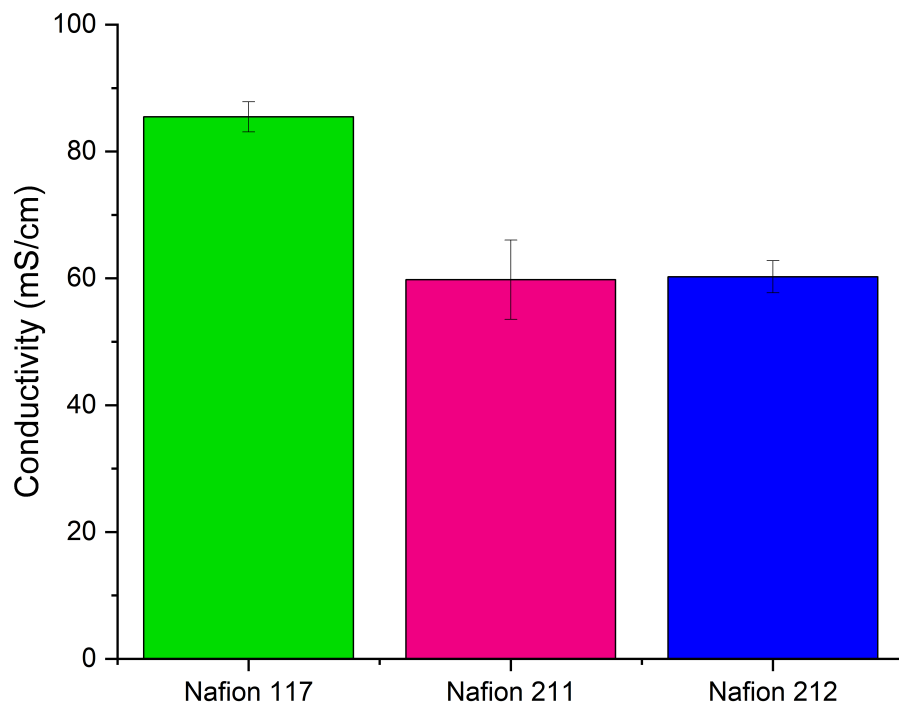
Figure 3.4: The conductivity of each Nafion membrane type with 95% confidence intervals.

impedence method by Sone et al[8]. The impressive performance of Nafion 117 is likely attributable to its thicker structure and larger equivalent weight, which facilitate increased water uptake and thereby enhance proton transportation.

In contrast, Nafion 211 and 212 demonstrate lower proton conductivities. Specifically, Nafion 211 registers approximately 59.78 mS/cm with a larger 95% CI of ±6.25, implying a slightly reduced precision in these measurements. This value agrees with the reported value of 50-60 mS/cm for a single Nafion 211 membrane by Bukola et al. in 2018[15]. Nafion 212, with a conductivity of around 60.24 mS/cm and a 95% CI of ±2.53, exhibits similar conductivity to Nafion 211. This value agrees with the reported 54 mS/cm value for proton conductivity of N212 at 100% RH[16]. The thinner structures and lower equivalent weights of Nafion 211 and 212, relative to Nafion 117, may have led to diminished water uptake, and consequently, decreased proton transportation. This comparison underscores the critical role of matching conductivity requirements with specific application needs in the selection of suitable Nafion membranes.

The different physical characteristics of Nafion membranes, primarily thickness and equivalent weight, directly impact their proton conductivity capabilities. Nafion 117, with its superior structure, emerges as the most promising candidate when high proton conductivity is the primary concern. However, it's essential to note that the right choice of membrane will invariably hinge on the specific requirements of the application at hand. For tasks where maximal conductivity isn't paramount, Nafion 211 and 212 might offer other advantages such as reduced thickness, potentially leading to decreased system resistance and improved mechanical properties. Researchers and practitioners should therefore weigh the trade-offs associated with each membrane variant in the context of their unique operational demands, ensuring the most effective and efficient outcomes.

The experimental method deployed in this study effectively achieved its intended objectives. The analysis of LSV curves successfully revealed variations in electrochemical behavior corresponding to different membrane thicknesses and types, as exemplified in Figures 3.2A-C. Further evidence of this sensitivity was apparent in the plots of corrected resistance against thickness in Figure 3.3, which distinctly captured differences between membranes of varying thickness and resistance characteristics. In the context of proton conductivity measurements, our method demonstrated a noteworthy capability to distinguish proton conduction from other ion conductivities, thereby affording a more accurate understanding of membrane behavior. The proton conductivities of Nafion N117, N211 and N212 membranes, as illustrated in Figure 3.4, underscored this capacity. Moreover, the associated 95% CI levels highlighted the method's robustness in reliably measuring true steady-state DC currents, thereby further validating the efficacy of our approach.

3.4.3 Implications of Methodological Contributions

The methodological advances presented in our study bear significant implications for the broader field of electrochemical research. This study serves as a springboard for several impactful applications and future research directions, particularly emphasizing our method's versatility, reliability, and potential for further refinement.

1. Benchmarking Proton Conductivity: Our methodology serves as an invaluable tool for measuring the proton conductivity of various types of membranes. As such, it could be employed as a benchmark for comparison in subsequent studies exploring similar or diverse membrane types.

2. Versatility of the Method: The distinct capability of our approach to segregate proton conduction from other ion conductivities underpins its extensive appli-

cability. This versatility extends beyond studies involving Nafion membranes, proving instrumental in any research necessitating precise measurements of specific ion conductivities.

3. Reliability in Resistance Measurement: Our method's ability to reliably measure true steady-state DC currents and resistance is a crucial development. This reliability, as corroborated by the low standard deviations observed in our data, recommends our method for broad use in various electrochemical studies.

4. Potential for Further Refinement: The proficiency of our method in distinguishing between membranes of varying thickness and resistance characteristics opens avenues for further refinement and optimization. Future research endeavors could seek to enhance the sensitivity of our method or expand its applicability to investigate membranes of diverse materials or under different operational conditions.

5. Broad Impact on Electrochemical Research: In summary, our study's methodological contribution has the potential to impact electrochemical research significantly. By introducing a reliable and adaptable method to examine membrane properties and behaviors, we pave the way for more refined and insightful inquiries in the future.

3.5   Conclusions and Future Directions

Our study presented a robust and sensitive method for evaluating the electrochemical properties of Nafion membranes particularly involving proton conduction, demonstrating its effectiveness through an examination of Nafion N117, N211, and N212 membranes. The method's ability to accurately measure proton conductivity

and resistances, segregate proton conduction from other ion conductivities, and discern between membranes of varying thickness and resistance characteristics showcases its vast potential applicability in electrochemical research. Conclusively, Nafion N117 exhibited the highest proton conductivity, while Nafion 211 and 212 demonstrated similar, albeit slightly lower conductivities. These differences underline the inherent variations in proton conductive properties between the 1st and 2nd generation of Nafion membranes, thereby affecting their respective suitability for fuel cell applications. While our method marks a significant step forward in assessing Nafion membranes, it also opens the door for further research directions:

1. Expanding the scope: Future studies could extend the use of this method to other membrane types, exploring its effectiveness in measuring specific ion conductivities beyond proton conduction.

2. Refining the method: Efforts can also be invested in enhancing the sensitivity of our method or extending its applicability to diverse operational conditions. This might include exploring the influence of temperature or humidity changes on the electrochemical properties of the membranes.

3. Material Modifications: Future research could delve into assessing modified Nafion membranes or hybrid membranes, enabling a deeper understanding of how such modifications impact the electrochemical behavior and proton conductivity.

4. Performance analysis in actual devices: An interesting area for future work could be to assess the implications of our findings in real-world fuel cell applications. This would involve using our method to characterize membranes in operating fuel cells and link the observed electrochemical properties to the overall device

performance.

In summary, the method proposed in this study signifies a substantial contribution to electrochemical research, offering a reliable tool for evaluating membrane behaviors while stimulating further inquiries in the field.

3.6 Real World Applications

The methodology presented in this study is not limited to Nafion membranes or fuel cell applications. It is a versatile tool with broader applications in evaluating the properties of various PEMs, with the ability to expand its utility to other electrochemical energy systems. As a case in point, our method has been successfully employed to calculate the through-plane proton conductivity of synthesized membranes developed by Dr. Eric Davis's research group at Clemson University. These PEMs, specifically designed for vanadium redox flow batteries (VRFBs), represent an exciting frontier in the quest for advanced energy storage solutions. Our findings pertaining to these novel PEMs have contributed to the body of knowledge in the field, with results published in several peer-reviewed journals. As such, this method demonstrates its substantial potential to facilitate research and development across a spectrum of electrochemical systems, contributing to advancements in energy conversion and storage technologies. A list of these publications featuring our method's application to these Clemson University membranes is provided in the table below for reference:

These results further validate the versatility and potential of the method developed in this study. By providing an accurate and sensitive method to measure membrane resistances and proton conductivities, our work is instrumental in guiding the selection and development of suitable PEMs for various real-world applications.

Table 3.2: Proton conductivities of sample membranes measured under hydrated conditions at room temperature using the developed method.

PEM Name	Proton Conductivity (mS/cm)	Publication
100% PFTOS immediate-cast	40	Allison et al. 2021[17]
100% PFTOS stir-cast	41	
Naf-UF-10	94	
Naf-UF-100	72	
Naf-UF-200	77	
Naf-UF-dried	68	
Naf-AA-10	66	
Naf-AA-100	66	Allison et al. 2022[18]
Naf-AA-200	59	
Naf-AA-dried	54	
Naf-AS-10	77	
Naf-AS-100	52	
Naf-AS-200	57	
Naf-AS-dried	60	
3hSPEEK	104	
5LMW-3hSPEEK	199	
15LMW-3hSPEEK	121	
25LMW-3hSPEEK	74	
5HMW-3hSPEEK	181	
15HMW-3hSPEEK	75	
25HMW-3hSPEEK	63	
		Xueting et al. 2023 (Submitted)
4hSPEEK	97	
5LMW-4hSPEEK	174	
15LMW-4hSPEEK	123	
25LMW-4hSPEEK	109	
5HMW-4hSPEEK	129	
15HMW-4hSPEEK	76	
25HMW-4hSPEEK	67	

This includes fuel cells, redox flow batteries, and potentially beyond, signifying the wider relevance and impact of our study.

References

(1) Mauritz, K. A.; Moore, R. B. *Chemical Reviews* **2004**, *104*, 4535–4586.

(2) Matos, B. R.; Goulart, C. A.; Santiago, E. I.; Muccillo, R.; Fonseca, F. C. *Applied Physics Letters* **2014**, *104*, DOI: `10.1063/1.4867351`.

(3) Lin, K.; Wang, C.; Qiu, Z.; Yan, Y. *Polymers* **2022**, *14*, 1283.

(4) Ahmad, S.; Nawaz, T.; Ali, A.; Orhan, M. F.; Samreen, A.; Kannan, A. M. *International Journal of Hydrogen Energy* **2022**, *47*, 19086–19131.

(5) Choi, P.; Jalani, N. H.; Datta, R. *Journal of The Electrochemical Society* **2005**, *152*, E123.

(6) Ryu, S.; Kim, J.-H.; Lee, J.-Y.; Moon, S.-H. *Journal of Materials Chemistry A* **2018**, *6*, 20836–20843.

(7) Guo, J.-W.; Wang, J.-L.; Jiang, S.-k.; Li, L. *Materials Chemistry and Physics* **2023**, *303*, 127824.

(8) Sone, Y.; Ekdunge, P.; Simonsson, D. *Journal of The Electrochemical Society* **1996**, *143*, 1254.

(9) Kuwertz, R.; Kirstein, C.; Turek, T.; Kunz, U. *Journal of Membrane Science* **2016**, *500*, 225–235.

(10) Cahan, B. D.; Wainright, J. S. *Journal of The Electrochemical Society* **1993**, *140*, L185.

(11) Lee, C. H.; Park, H. B.; Lee, Y. M.; Lee, R. D. *Industrial Engineering Chemistry Research* **2005**, *44*, 7617–7626.

(12) Silva, R. F.; De Francesco, M.; Pozio, A. *Journal of Power Sources* **2004**, *134*, 18–26.

(13) Giffin, G. A.; Haugen, G. M.; Hamrock, S. J.; Di Noto, V. *Journal of the American Chemical Society* **2013**, *135*, 822–834.

(14) Cooper, K. R. *Journal of The Electrochemical Society* **2010**, *157*, B1731.

(15) Bukola, S.; Liang, Y.; Korzeniewski, C.; Harris, J.; Creager, S. *Journal of the American Chemical Society* **2018**, *140*, 1743–1752.

(16) Aziz, M. A.; Shanmugam, S. *Journal of Materials Chemistry A* **2017**, *5*, 16663–16671.

(17) Domhoff, A.; Martin, T. B.; Silva, M. S.; Saberi, M.; Creager, S.; Davis, E. M. *Macromolecules* **2021**, *54*, 440–449.

(18) Domhoff, A.; Wang, X.; Silva, M. S.; Creager, S.; Martin, T. B.; Davis, E. M. *Soft Matter* **2022**, *18*, 3342–3357.

Chapter 4

Mitigating the Effects of Cation Contamination in Nafion Membranes for Improved Hydrogen/Deuterium Separation in Electrochemical Hydrogen Pump Cell Experiments

4.1 Abstract

This chapter provides an in-depth investigation into the effects of ammonium and copper cations on the resistances experienced in hydrogen/deuterium (H/D) electrochemical pump cell experiments using Nafion membranes. We found that conventional procedures in the literature, which omit a reprotonation/redeuteration step

post copper etching, could led to significant cation contamination. Such contamination was evidenced to considerably increase resistance in H/D pump cell experiments, hindering the efficacy of the proton or deuteron transport. To mitigate this issue, a new post-treatment process was proposed that includes an additional reprotonation/redeuteration step after the copper etching stage. The implementation of this improved procedure substantially lowered resistances in H/D pump cell experiments, thereby demonstrating its effectiveness. These findings not only reveal the necessity of considering cation contamination during Nafion membrane preparation but also provide a novel methodology to improve H/D pump cell experiment efficiency significantly. Furthermore, this chapter lays a critical groundwork for subsequent investigations into the role of graphene in H/D separation, the focus of the next chapter.

4.2   Introduction

Nafion, a perfluorinated sulfonic acid (PFSA) ionomer, has attracted significant attention in the advanced materials sector due to its unique and multifaceted properties. Not only does it exhibit impressive proton conductivity and remarkable chemical stability, but it also demonstrates exceptional attributes such as considerable water uptake, ion exchange capacity, low gas permeability, and robust electrochemical stability[1][2][3]. These combined characteristics make Nafion a preferred material for a myriad of applications. In the field of energy, it plays a pivotal role in proton-exchange membrane fuel cells (PEMFCs)[4][5][6], where its conductive capabilities facilitate the optimized transfer of protons. This characteristic directly contributes to the high energy efficiency and performance of these devices. Furthermore, Nafion's chemical stability enables it to withstand harsh operating conditions, enhancing the

$$\left[\left[CF_2\!\!-\!\!CF_2 \right]_x \!\!CF_2\!\!-\!\!CF \right]_n$$
$$O\!-\!CF_2\!\!-\!\!CF\!-\!O\!-\!CF_2\!\!-\!\!CF_2\!\!-\!\!SO_3^-M^+$$
$$CF_3$$
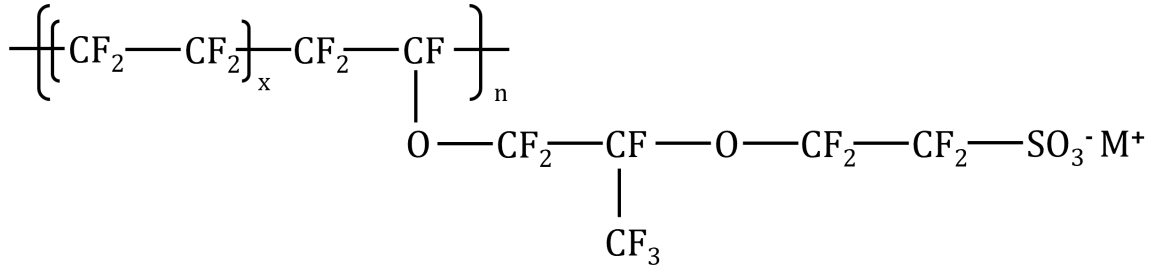
Figure 4.1: Structure of Nafion ($M^+ = H^+$, Na^+, K^+ etc.)

longevity of devices in which it's incorporated[6]. Apart from fuel cells, Nafion also finds use in a broad spectrum of applications, from water electrolysis[7], flow batteries[8][9][10] to act as a binder in polymer-modified electrodes[11][12].

While Nafion's attributes have made it an indispensable material in these and other applications, they also present a particular challenge that this study intends to address. Ion exchange membranes like Nafion can be considerably influenced by surrounding cations in a solution[13][14][15][16]. This is primarily due to the presence of negatively charged sulfonic acid groups within Nafion that can readily exchange protons (H^+) with other cations in solution. When these ion-exchange sites encounter certain cations in solution, they can preferentially absorb these cations, causing changes in the overall membrane properties[17]. Such absorption alters the ionic conductivity, mechanical durability, and chemical stability of the membrane, and hence, the performance of the device that uses it[18][19].

There are many studies conducted on cation-exchanged Nafion membranes. Han et al. observed dramatic decrease in proton conductivity with increase of cobalt level in Nafion films[18]. Hongsirikarn et al. investigated the impact of Na^+, Ca^{2+}, Fe^{3+} cations on the conductivity of Nafion membranes under conditions akin to PEM-FCs, revealing that cation contamination significantly reduces conductivity compared to the purely protonic form[20]. They further probed the impact of NH_4^+ on Nafion

membrane conductivity, revealing a significant decrease in both liquid and gas phases, especially under varying humidity conditions[21]. Tandon et al. demonstrated that the thermal stability of Nafion membranes improves with the exchange of larger ionic radius cations, particularly sodium, with the effect attributed to reduced water content and enhanced sulfonate-cation interaction[22]. Martí-Calatayud et al. studied how chromic acid and nickel sulfate concentrations impact the transport properties of a cation-exchange membrane, with significant competition between Ni^{2+} and H^+ ions, which impacts the membrane's transport properties[23]. Lage et al. conducted thermogravimetric analysis of Nafion in acid and salt forms, showing similar thermal decomposition profiles across different atmospheres and alkali counter-cations after the membranes were treated with various alkali chloride solutions[24]. Yeager et al. examined the self-diffusion coefficients of sodium ion, cesium ion, and water in Nafion 120 membranes, revealing distinct diffusional properties compared to conventional polystyrene sulfonates and suggesting cations may exist in two distinct regions in the polymer, dependent on ion size and charge density, a conclusion supported by a proposed structural model of Nafion[25].

The integration of other advanced materials with Nafion, to further enhance its capabilities presents an exciting research direction. A particular area of focus has been the use of Graphene — Nafion composite membranes for H/D isotope separation. In a significant portion of the current literature, including our group's work, the preferred technique for creating these composite membranes involves depositing graphene onto copper sheets via Chemical Vapor Deposition (CVD), followed by transferring the graphene layer onto Nafion[26][27][28]. A commonly employed etchant for removing the copper is ammonium persulfate (APS), and post-etching, the membranes are usually rinsed with deionized (DI) water. However, during this process, Nafion's cation sites can easily be exchanged with ammonium ions and etched

Cu^{2+} ions, potentially impacting proton and deuteron transport across the membrane. Such unintended cation incorporation can significantly influence the membrane's performance. It often leads to increased resistances during H/D pump cell experiments, which could subsequently reduce the efficiency of processes such as isotope separation or energy generation. The current body of literature inadequately addresses the need for thorough removal of these cations post-etching, a limitation that motivates the work presented in this chapter.

The principal focus here is the exploration of the effects of residual ammonium and copper cations in Nafion membranes, particularly on H/D pump cell resistances. This investigation aims to furnish compelling evidence highlighting the limitations of current procedures, leading to the proposition of an enhanced protocol designed to effectively mitigate these issues. This revised protocol, which will be introduced and evaluated, involves a robust reprotonation/deuteration process designed to effectively remove cation contamination. By doing so, we hope to lay the foundation for enhanced membrane preparation methods that maintain optimal Nafion performance in various applications, particularly those involving H/D separation. In essence, this chapter is a crucial step towards addressing overlooked problems in the preparation and use of Graphene — Nafion composite membranes and paves the way for a comprehensive study of the electrochemical behavior of graphene in H/D separation processes. This gap in the existing literature and protocols calls for a thorough investigation and an updated procedure that mitigates these issues, thereby enhancing the overall efficiency of H/D pump cell experiments.

4.3   Materials and Methods

4.3.1   Membrane Preparation

The membrane preparation process began with a preliminary pretreatment of Nafion membranes to yield two distinct types: H-Nafion and D-Nafion. The untreated Nafion membranes were first cleaned by submersion in a 3% H_2O_2 solution held at 80°C for one hour. This was followed by a thorough rinse with deionized water to remove residual H_2O_2 solution. The resulting cleaned membranes were then subjected to an acid treatment; H-Nafion membranes were immersed in a 0.5 M H_2SO_4 in H_2O solution, and D-Nafion membranes were submerged in a 0.5 M D_2SO_4 in D_2O solution. Both these treatments were conducted at 80°C for one hour, ensuring sufficient acid exposure. Post acid treatment, a rinse was performed wherein the H-Nafion membranes were washed with deionized water, while D-Nafion membranes were rinsed with D_2O. This rinse further ensured the removal of excess acid and prepared the membranes for subsequent steps.

AC-Nafion membranes were produced by hot-pressing 1 cm x 1 cm pure copper sheets (without graphene) onto Nafion 211 membranes. These were then immersed in a 0.3 M Ammonium persulfate solution for 8 hours and subsequently rinsed with DI water. Here, 'AC' in AC-Nafion denotes that the Nafion 211 membrane has undergone an eight-hour immersion in an Ammonium-Copper solution.

4.3.2   Fabrication of Membrane-Electrode Assemblies (MEAs)

The MEA fabrication process consisted of hot-pressing Nafion 211 membranes together with Pt/C cloth electrodes, forming a sandwich-like assembly. Either one or two Nafion 211 membranes were selected based on the specific requirements of

the planned experiments. Two disk-shaped Pt/C cloth electrodes, each with an area of 0.18 cm^2, were aligned on either side of the chosen Nafion membrane(s). The assemblage was then hot-pressed under 140 °C and 600 psi for 3 minutes to yield a compact MEA with secured electrode-membrane interfaces.

4.3.3   Proton Exchange Membrane (PEM) Cell Assembly

The PEM cell was custom-built in a swage-style design, which allowed for easy integration of the fabricated MEAs. To facilitate efficient electron conduction and uniform distribution of reactant gases across the MEA surface, two Titanium current collectors were incorporated. Sandwiched between these current collectors and the MEAs were two AvCarb P50 Gas Diffusion Layers (GDLs) to optimize gas diffusion. For the H-pump and D-pump experiments, research-grade H$_2$ and D$_2$ gases were used, respectively. These gases were prepared by maintaining their flow rates at 20±2 SCCM and humidifying them by bubbling through deionized water and D$_2$O respectively. The prepared humidified gases were then introduced into the PEM cell for five minutes to equilibrate before the start of the electrochemical experiments.

4.3.4   Controlled-Potential Amperometric Analysis

Amperometric analysis was carried out with the objective of further investigating the resistance behavior of the membranes. Using the NN (two layers of Nafion 211) MEAs, the potential was held constant at -70 mV throughout the experiment. An alternating gas feed strategy was employed to minimize the effects of potential mounting errors in the membrane or other experimental inconsistencies. Switching between humidified deuterium and hydrogen gases as input feeds, the amperometric response of the membranes was recorded and analyzed. Data collected from these
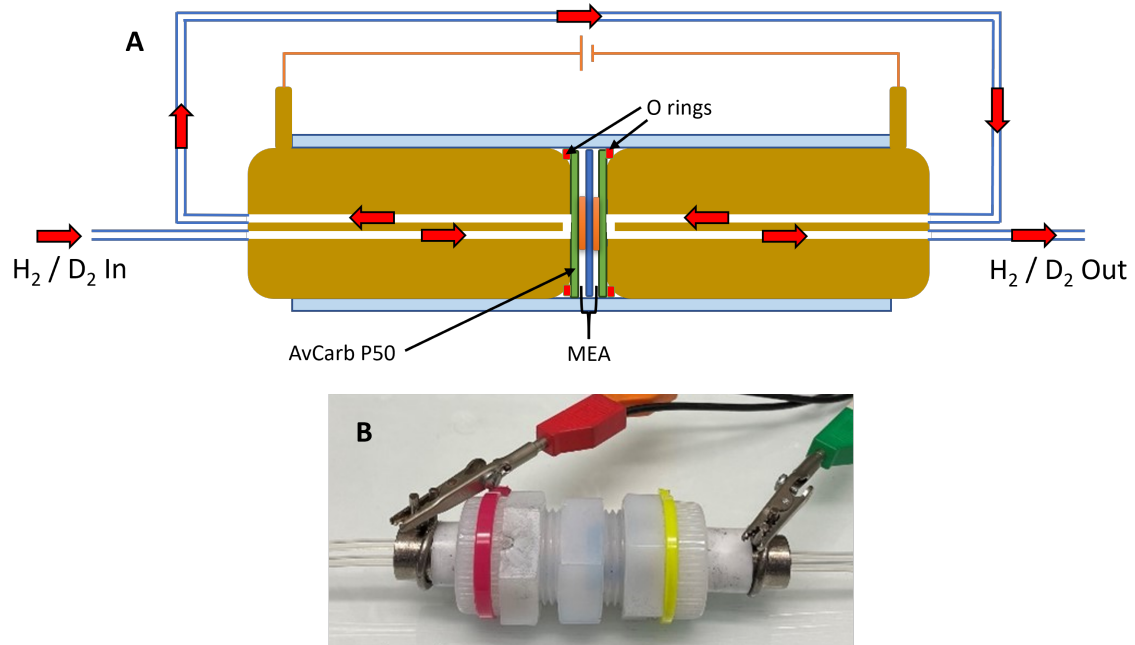
Figure 4.2: A. Schematic Diagram and B. Real-World Image of the PEM Cell Assembly. The A. diagram delineates the arrangement of various components of the swage-style fuel cell used for our experiments. The cell incorporates two Titanium current collectors two AvCarb P50 GDLs and two O' rings. The MEAs, fabricated in prior steps, are nestled between these GDLs. B. depicts a real-world image of the assembled electrochemical pump cell, visually illustrating the compact and integrated design of the PEM cell assembly.

experiments were used to plot resistance versus time graphs, providing a dynamic view of the membrane's response to alternating gas feeds.

4.3.5   Deuterium-Pump and Hydrogen-Pump Experiments

Separate MEAs were prepared for D-pump and H-pump experiments. The D-pump experiments utilized D-Nafion and AC-Nafion MEAs, whereas H-Nafion and AC-Nafion MEAs were used for the H-pump experiments. The implementation of these distinct MEAs facilitated a systematic investigation of the effects of Ammonium and Copper contamination on the proton and deuteron transport properties of the Nafion membranes.

4.3.6   Electrochemical Analysis

Electrochemical characterization was achieved through Linear Sweep Voltammetry (LSV) on a PineResearch WaveDriver 20 electrochemical workstation. The system, under an atmosphere of humidified hydrogen gas, was scanned within a voltage range of -70 mV to 70 mV at a scan rate of 1 mV/s. The resulting LSV curves were recorded meticulously for subsequent analysis, revealing valuable insights into the electrochemical behavior of the ionomer membranes.

4.3.7   Reprotonation/Redeuteration

To counter the contamination of ammonium and copper in the membranes, a reprotonation process was implemented. AC-Nafion membranes were submerged in a 0.5 M H_2SO_4 in H_2O solution for six hours. This treatment transformed the AC-Nafion back into their original H-form, simultaneously reducing the effects of the contaminants. Redeuteration was accomplished similarly using 0.5 M D_2SO_4 solution

in D_2O.

4.3.8   Post-Treatment Validation

Upon completion of the reprotonation/redeuteration treatment, further LSV and Energy-Dispersive X-ray spectroscopy (EDX) analyses were carried out to assess the effectiveness of the treatment. LSV tests were run on AC-Nafion MEAs under the H-pump setup, comparing the performance of the treated and untreated membranes. Simultaneously, EDX analyses were employed to detect the presence or absence of ammonium and copper ions in the treated and untreated samples. This robust method of validation provided comprehensive insights into the success of the remediation process.

4.4   Results and Discussion

Previously, our team conducted H-pump and D-pump experiments separately using multiple Membrane Electrode Assemblies (MEAs) that were fed by either humidified H_2 or D_2. However, the primary measurement in these experiments was resistance, which can be easily affected by the conditions within the cell. To avoid potential errors associated with re-mounting and using a separate MEA for comparison, we decided to alternate the gas feeds between humidified D_2 and humidified H_2 while maintaining the MEA within the cell intact.

Figure 3 displays how the resistance varied with time for the NN MEA. This data was derived from chronoamperometry measurements taken during alternating feeds of H_2 and D_2 to the symmetric cell and subsequently converted to resistance values. The NN MEAs demonstrate rapid stabilization to a steady-state behavior. Distinct resistance 'spikes' are observed each time there's a transition in the gas feed.
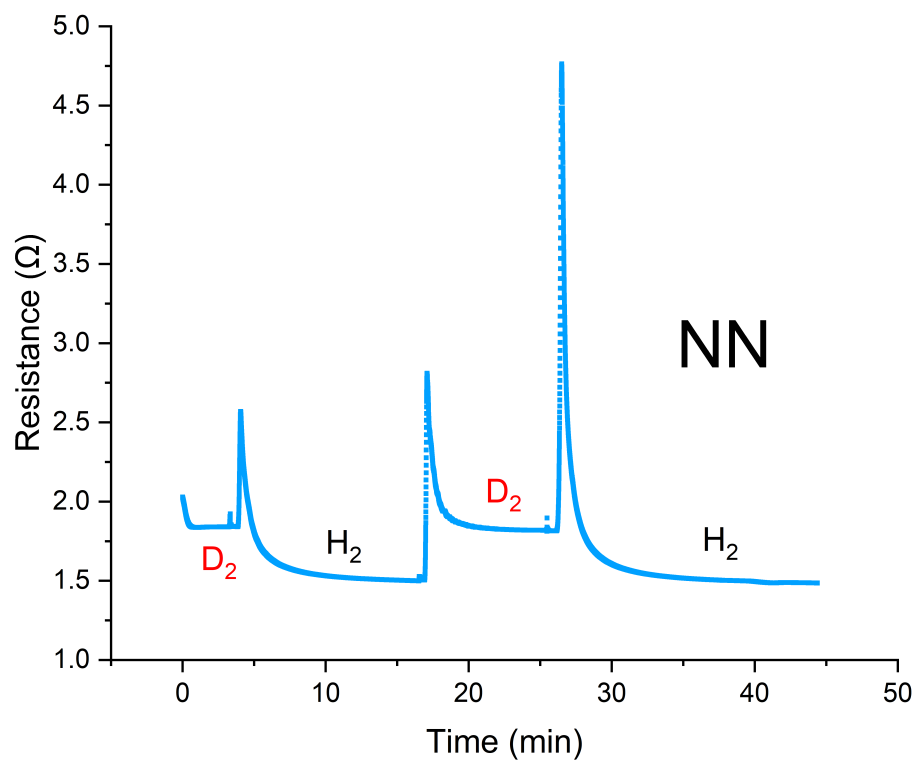
Figure 4.3: Resistance Analysis of NN MEA under Alternating Feed Gas Strategy. The graph depicts the resistance fluctuations of the NN MEA during chronoamperometry at a fixed potential of -70 mV.

These spikes arise from the temporary air gap between H_2 and D_2 (and vice versa) due to a slight delay when switching the gases. Lower resistances were observed for H^+ transport compared to D^+. This difference in resistance for proton and deuteron transport could be attributed to slight variations in ion transport rates for H^+ and D^+ in the PEM. The findings indicate a more consistent and faster achievement of steady-state behavior in NN membranes compared to similar experiment conducted on NGN (Nafion—Graphene—Nafion) in Chapter 5.

We executed a set of control experiments analogous to those with CVD graphene-incorporated Nafion membranes. Notably, both Dr. Saheed Bukola, a former member of our group, and Lozado-Hidalgo's group have previously demonstrated the potent isotope separation capabilities of these membranes when integrated with CVD graphene. For their control studies, both teams utilized two layers of pure Nafion, devoid of graphene. We contend that a better control experiment would have combined one layer of H or D-Nafion with one layer of AC-Nafion. This recommendation arises from noting that during the copper-etching phase, a Nafion membrane was subjected to a prolonged exposure to ammonium and copper cations in the APS solution.

Figures 4.4A and 4.4B delve into the electrochemical behavior of different MEA configurations using LSV tests for H-pump (A) and D-pump (B) conditions, respectively. Both figures examine three MEA variations: two layers of either H or D-Nafion, a combination of one layer of H or D-Nafion with one layer of AC-Nafion, and two layers of AC-Nafion.

For the H-pump (Figure 4.4A) and D-pump (Figure 4.4B) tests, the dual-layer AC-Nafion setup consistently displays the lowest current, suggesting the highest resistance due to likely ammonium and copper contamination. In contrast, the dual-layer of either H or D-Nafion indicates the least resistance with its elevated current, reflecting optimal proton or deuteron transport properties in uncontaminated membranes.
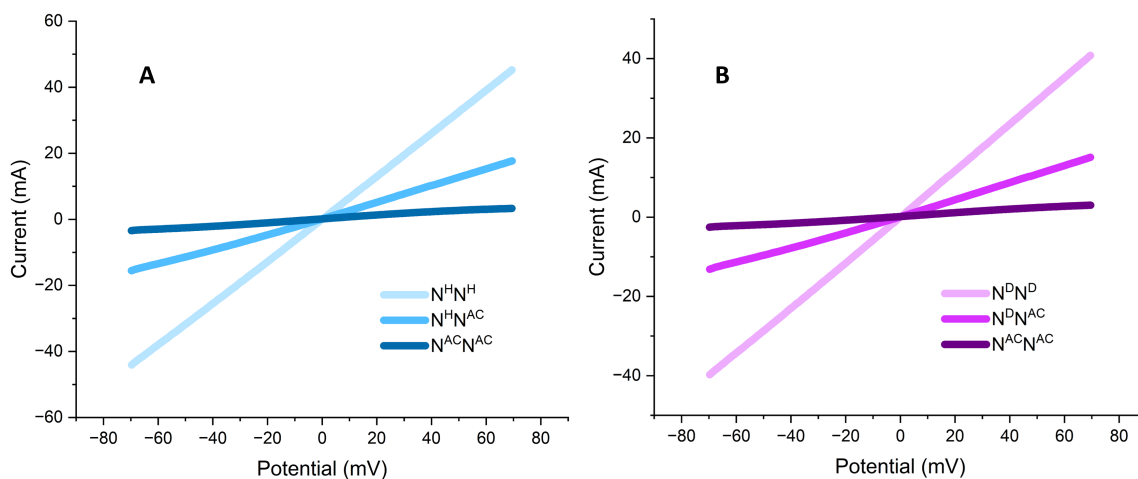
Figure 4.4: Electrochemical profiles from LSV tests on different MEA configurations for H-pump (A) and D-pump (B) conditions. Variations include two layers of either H or D-Nafion, a hybrid of one layer of H or D-Nafion with one layer of AC-Nafion, and two layers of AC-Nafion. The results highlight the influence of ammonium and copper contamination on the resistance to hydrogen isotope transport across the tested MEAs.

The hybrid configurations (combining one layer of either H or D-Nafion with AC-Nafion) render an intermediate current level, underscoring the negative impact of these contaminants on ion transport.

This pattern indicates that ammonium and copper cations increase resistance in H/D pump cell experiments. Such findings underscore the critical role these contaminants play in hydrogen isotope transport, emphasizing the importance of rigorous contamination control during MEA fabrication.

In an effort to address the aforementioned challenges pertaining to the ammonium and copper contamination of Nafion membranes during fabrication, a post-treatment procedure was proposed and implemented. This involved immersing the NN MEAs in a 0.5M H_2SO_4 in H_2O or 0.5M D_2SO_4 in D_2O solution for 6 hours, followed by a thorough wash with DI water or D_2O, depending on the desired form of the membrane.
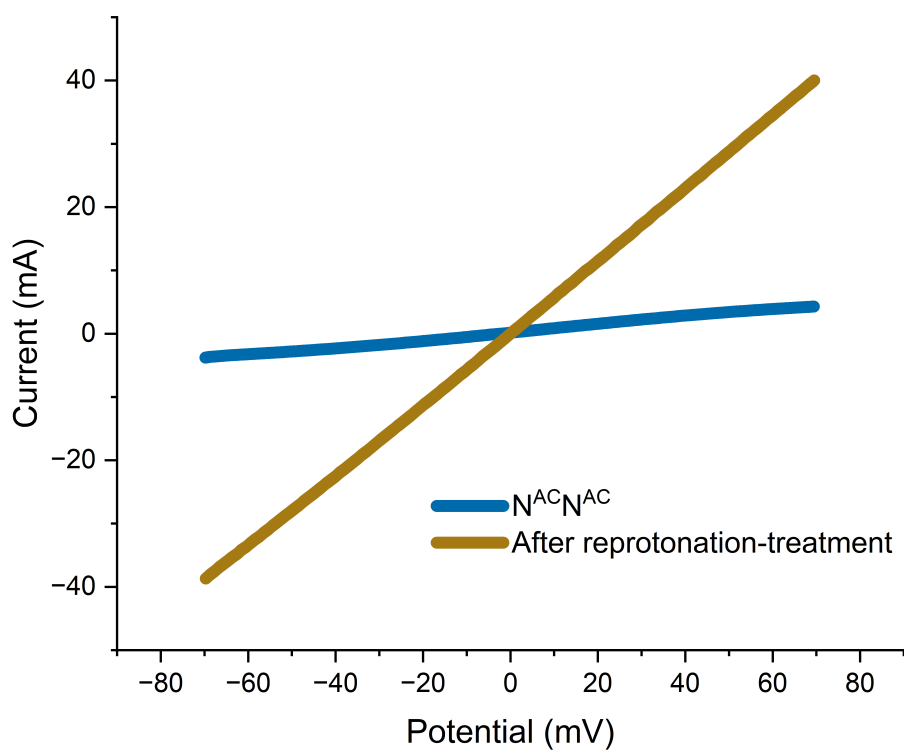
Figure 4.5: Comparison of LSV curves obtained for ammonium and copper contaminated NN membrane before and after reprotonation treatment in H-pump conditions.

Our objective in subjecting the MEAs to this treatment was to eliminate potential contaminants and revert the membrane to its intended H or D form. This procedure facilitated the successful replacement of ammonium and copper cations with the original hydrogen or deuterium ions at the ion exchange sites of the PEM. It offered a simple yet effective solution to the ammonium contamination issue that has clouded previous research, thereby improving the reliability and validity of the observed isotope separation results. Furthermore, this post-treatment process may pave the way for improved and standardized practices for membrane fabrication in future research.

Figure 4.5 provides a comparative analysis of LSV curves for an ammonium and copper-contaminated NN membrane, both before and after a reprotonation treatment (acid wash), in the context of H-Pump conditions. Two distinct lines demarcate the LSV curves of the contaminated and post-treated membranes, providing a clear comparative visualization of their resistances for proton transport across the membrane. The LSV curve corresponding to the contaminated membrane demonstrates a significantly higher resistance compared to that of the post-treated membrane. This decrease in resistance, to a level comparable with non-contaminated NN membranes, is a direct consequence of the reprotonation treatment. It thereby underlines the efficacy of the post-treatment process in not only eliminating contaminants but also in restoring the membrane's optimal performance.

In addition, EDX analysis was conducted to verify the elemental composition of the membranes post-treatment. EDX is a powerful tool for detecting the presence of specific elements, including trace amounts of contaminants. In Figures 4.6A and 4.6B, we present the elemental composition of membranes both before and after the post-treatment process, as revealed through EDX analysis. Figure 4.6A reveals that prior to post-treatment, the membranes contain not only their principal elements
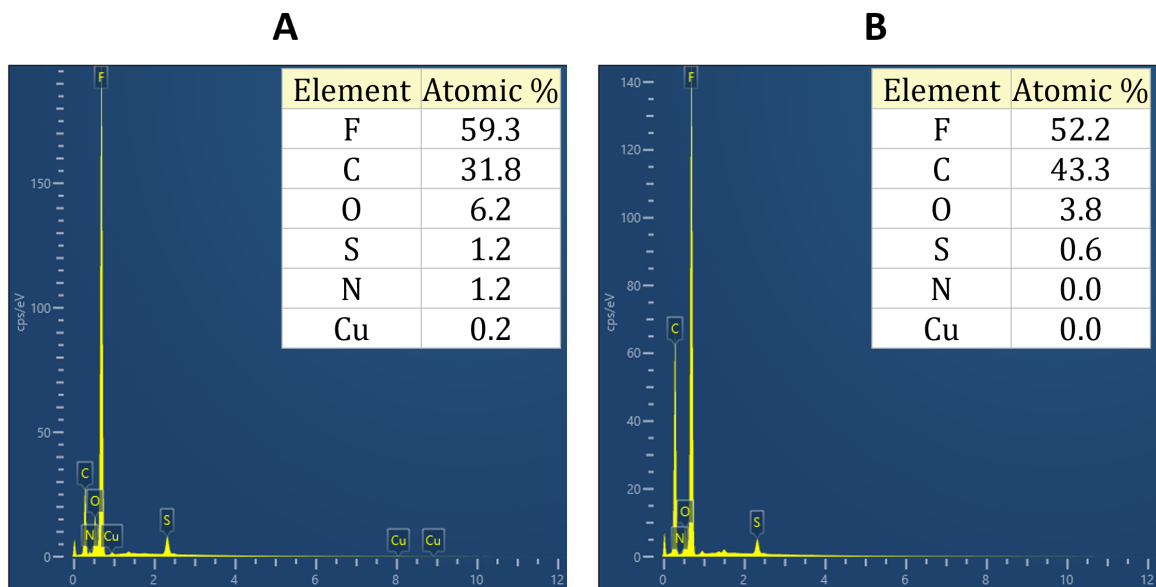
Figure 4.6: EDX analysis of membranes prepared via two distinct methods. (A) presents the EDX results for a membrane treated with the previously documented etching and DI water rinsing procedure, highlighting the presence of ammonium, copper ions, and other elements. (B) showcases the EDX outcomes for a membrane prepared using the modified etching technique, which includes the recommended re-protonation step.

but also detectable amounts of ammonium and copper, with atomic percentages of approximately 1.1% and 0.2%, respectively. These unintended contaminants are indicative of the inefficacy of the previous etching and DI water rinsing method in fully purifying the membrane.

In contrast, Figure 4.6B demonstrates the effectiveness of our proposed post-treatment procedure in membrane decontamination. Following the treatment, the EDX analysis shows no traces of either ammonium or copper, suggesting a complete conversion of the contaminated membrane back to its original form. The complete absence of these atomic percentages implies a successful elimination of contaminants, underlining the efficacy of the post-treatment in preparing cleaner, more reliable membranes for hydrogen isotope separation.

Our findings clearly demonstrate a marked increase in resistance in the H/D pump cell experiments conducted using membranes prepared following conventional protocols. These protocols, as found in the literature, involve a copper etching step using an APS solution but do not incorporate a reprotonation/redeuteration step post-etching. As depicted in Figures 4.4A-B, the LSV curves obtained from these experiments reveal significantly higher resistances compared to those observed for membranes that underwent our additional post-treatment step, as shown in Figure 4.5.

Interestingly, our results do not align perfectly with the expected outcomes based on previous literature. While prior reports suggest that simply washing membranes with water or D_2O after immersing them in APS solution effectively removes residual cations, our findings starkly challenge this notion. Our data indicates that this rinsing method does not fully eliminate the ammonium and copper cations. Upon implementing our additional treatment step, involving reprotonation/redeuteration of the Nafion membranes, we observed a significant decrease in the resistance during H

70

pump cell experiments. This further validates our hypothesis and underscores the importance of an additional treatment step to remove cation contamination effectively.

In summary, our study highlights a significant oversight in the conventional preparation of Nafion membranes for H/D pump cell experiments. The presence of ammonium and copper cations, if not adequately addressed, can have a substantial impact on the resistance experienced in these experiments, and by extension, the overall efficiency of the process.

4.5 Proposed Standard Procedure for Evaluating CVD Graphene Deposited Membranes

In light of the discoveries made during this investigation, we propose an improved post-treatment process to mitigate the impact of cation contamination on H/D pump cell resistances. The purpose of this process is to efficiently remove any ammonium and copper cations that have exchanged with the cation exchange sites of the Nafion during the previous etching step with APS solution.

The proposed process involves a further reprotonation/redeuteration step following the conventional copper etching process described more detail in subsection 3.2 of Chapter 5. This involves immersing the Nafion membranes in a 0.5 M H_2SO_4 in H_2O or 0.5 M D_2SO_4 in D_2O solution. Through this process, the ion-exchange sites of the Nafion undergo re-exchange, replacing ammonium or copper cations with protons or deuterons, respectively. After this immersion, the membranes are thoroughly rinsed with water or D_2O respectively to remove any residual acid solution.

In addition to removing cation contamination, this additional step also reconverts the membranes back to their original H or D form. This is a significant improve-

ment on previous protocols, which do not include this reprotonation/redeuteration step after the copper etching stage. Our expectation is that this proposed post-treatment process will substantially improve the performance of the membranes in H/D pump cell experiments. As shown in our findings, implementing this additional step resulted in significantly lower resistances, suggesting more effective proton or deuteron transport through the Nafion membrane. This process could be instrumental in analyzing the efficiency and effectiveness of graphene-integrated PEMS for H/D separation.

For those foregoing, the recommended post-acid wash treatment after the CVD graphene transfer onto Nafion, the H/D separation factors arising from those membranes should not be compared to two layers of pure Nafion. Instead, the appropriate control MEA, consisting of either H or D-Nafion paired with one layer of AC-Nafion, should be used for comparison.

In conclusion, this proposed acid wash treatment to the already established procedure presents a promising solution to the problems associated with cation contamination in Nafion membranes. It is our hope that this new process will contribute significantly to advancing the current understanding and practices in the field of CVD graphene-integrated PEM for H/D separation.

4.6 Conclusions

The investigation presented in this chapter provided an in-depth analysis of the effects of ammonium and copper cations on the resistances in H/D pump cell experiments using Nafion membranes. The key discovery highlighted that without a reprotonation/redeuteration step after the copper etching phase in the CVD graphene transfer to Nafion process leads to significant cation contamination. This contami-

nation, in turn, increases the resistances during H/D pump cell experiments, thereby diminishing the accuracy of proton or deuteron transport measured through the membranes.

To address this issue, a new post-treatment process was proposed and tested that involves an additional reprotonation/redeuteration step after the copper etching process. The implementation of this process was found to result in significantly lower resistances in H/D pump cell experiments, demonstrating the feasibility and effectiveness of this approach. These findings underscore the importance of considering and mitigating cation contamination in the preparation of Nafion membranes for H/D pump cell experiments.

These findings form a critical foundation for Chapter 5 of this dissertation. Having established the importance of the post-treatment process in mitigating cation contamination and reducing resistances, Chapter 5 will focus on evaluating the effectiveness of CVD graphene-integrated Nafion in H/D separation. The proposed post-treatment process will be integral to preparing the Nafion membranes for these experiments, ensuring the integrity and reliability of the results. Thus, the work conducted in this chapter not only provides critical insights into the issues associated with cation contamination in Nafion membranes, but also sets the stage for further investigations into strategies for efficient H/D separation.

References

(1) Jalani, N. H.; Datta, R. *Journal of Membrane Science* **2005**, *264*, 167–175.

(2) Sigwadi, R.; Dhlamini, M. S.; Mokrani, T.; emavhola, F.; Nonjola, P. F.; Msomi, P. F. *Heliyon* **2019**, *5*, e02240.

(3) Kreuer, K. D. In *Handbook of Fuel Cells.*

(4) Kim, D. J.; Jo, M. J.; Nam, S. Y. *Journal of Industrial and Engineering Chemistry* **2015**, *21*, 36–52.

(5) Vishnyakov, V. M. *Vacuum* **2006**, *80*, 1053–1065.

(6) Okonkwo, P. C.; Ben Belgacem, I.; Emori, W.; Uzoma, P. C. *International Journal of Hydrogen Energy* **2021**, *46*, 27956–27973.

(7) Mališ, J.; Mazúr, P.; Paidar, M.; Bystron, T.; Bouzek, K. *International Journal of Hydrogen Energy* **2016**, *41*, 2177–2188.

(8) Jiang, B.; Wu, L.; Yu, L.; Qiu, X.; Xi, J. *Journal of Membrane Science* **2016**, *510*, 18–26.

(9) Domhoff, A.; Wang, X.; Silva, M. S.; Creager, S.; Martin, T. B.; Davis, E. M. *Soft Matter* **2022**, *18*, 3342–3357.

(10) Domhoff, A.; Martin, T. B.; Silva, M. S.; Saberi, M.; Creager, S.; Davis, E. M. *Macromolecules* **2021**, *54*, 440–449.

(11) Lee, S. J.; Mukerjee, S.; McBreen, J.; Rho, Y. W.; Kho, Y. T.; Lee, T. H. *Electrochimica Acta* **1998**, *43*, 3693–3701.

(12) Sasikumar, G.; Ihm, J. W.; Ryu, H. *Electrochimica Acta* **2004**, *50*, 601–605.

(13) Vijayakumar, M.; Govind, N.; Li, B.; Wei, X.; Nie, Z.; Thevuthasan, S.; Sprenkle, V.; Wang, W. *Frontiers in Energy Research* **2015**, *3*, DOI: 10.3389/fenrg.2015.00010.

(14) Volkov, V. I.; Chernyak, A. V.; Golubenko, D. V.; Tverskoy, V. A.; Lochin, G. A.; Odjigaeva, E. S.; Yaroslavtsev, A. B. *Membranes* **2020**, *10*, 272.

(15) Volkov, V. I.; Slesarenko, N. A.; Chernyak, A. V.; Avilova, I. A.; Tarasov, V. P. *Membranes* **2023**, *13*, 518.

(16) Volkov, V. I.; Chernyak, A. V.; Slesarenko, N. A.; Avilova, I. A. *International Journal of Molecular Sciences* **2022**, *23*, 5011.

(17) Kamcev, J.; Paul, D. R.; Freeman, B. D. *Journal of Materials Chemistry A* **2017**, *5*, 4638–4650.

(18) Han, A.; Fu, C.; Yan, X.; Chen, J.; Cheng, X.; Ke, C.; Hou, J.; Shen, S.; Zhang, J. *International Journal of Hydrogen Energy* **2020**, *45*, 25276–25285.

(19) Schalenbach, M.; Keller, L.; Janotta, B.; Bauer, A.; Tempel, H.; Kungl, H.; Bonnet, M.; Eichel, R. A. *Journal of The Electrochemical Society* **2022**, *169*, 094510.

(20) Hongsirikarn, K.; Goodwin, J. G.; Greenway, S.; Creager, S. *Journal of Power Sources* **2010**, *195*, 7213–7220.

(21) Hongsirikarn, K.; Goodwin, J. G.; Greenway, S.; Creager, S. *Journal of Power Sources* **2010**, *195*, 30–38.

(22) Iwai, Y.; Yamanishi, T. *Polymer Degradation and Stability* **2009**, *94*, 679–687.

(23) Martí-Calatayud, M. C.; García-Gabaldón, M.; Pérez-Herranz, V.; Ortega, E. *Journal of Membrane Science* **2011**, *379*, 449–458.

(24) Lage, L. G.; Delgado, P. G.; Kawano, Y. *Journal of Thermal Analysis and Calorimetry* **2004**, *75*, 521–530.

(25) Yeager, H. L.; Steck, A. *Journal of The Electrochemical Society* **1981**, *128*, 1880.

(26) Bukola, S.; Liang, Y.; Korzeniewski, C.; Harris, J.; Creager, S. *Journal of the American Chemical Society* **2018**, *140*, 1743–1752.

(27) Lozada-Hidalgo, M.; Zhang, S.; Hu, S.; Esfandiar, A.; Grigorieva, I. V.; Geim, A. K. *Nature Communications* **2017**, *8*, 15215.

(28) Bukola, S.; Beard, K.; Korzeniewski, C.; Harris, J. M.; Creager, S. E. *ACS Applied Nano Materials* **2019**, *2*, 964–974.

Chapter 5

Reevaluating Graphene's Hydrogen-Deuterium Selectivity: An Investigation Using Decontaminated Membranes

5.1   Abstract

This chapter presents a comprehensive reevaluation of the hydrogen/deuterium (H/D) isotope selectivity of graphene used in proton exchange membranes incorporated into electrochemical hydrogen pump cells. Existing literature reports high H/D selectivity ratios for graphene, up to factors of 8 and 14. We revisited these claims using fully protonated/deuterated Nafion-graphene-Nafion (NGN) membranes to eliminate potential artifacts from ionic contamination during the graphene transfer process. Our results fundamentally challenge the prevailing understanding of graphene's H/D selectivity. Through meticulous analysis, we calculated the graphene's area conduc-

77

tance to be 27 Scm^{-2} for H transport and 23 Scm^{-2} for D transport, which yielded a H/D selectivity of approximately 1.1-1.2. These findings suggest that previous high selectivity values could be due to experimental contamination rather than an inherent feature of graphene. This revised understanding of graphene's H/D selectivity could have profound implications for its usage in proton exchange membranes and stimulate new avenues of research in related fields.

5.2 Introduction

Hydrogen isotope separation has a profound impact across a multitude of industrial and scientific applications, such as nuclear power, isotope labeling, and medical diagnosis[1][2][3]. These sectors demand high precision and efficiency, and hence, the quest for innovative and practical methodologies for hydrogen isotope separation is a matter of crucial importance. Membrane technology, in this context, has surfaced as a highly promising technique due to its notable advantages of simplicity, cost-effectiveness, and scalability[4][5].

Graphene, a two-dimensional, single-layered lattice of carbon atoms, has elicited significant interest due to its exceptional electronic, mechanical, and thermal properties[6][7]. The relatively high surface area and low thickness of graphene confer it a high degree of utility across a broad spectrum of applications, including but not limited to high-frequency and high-speed electronic devices[8][9], photocatalysts[10][11], sensors[12][13], and protective coating[14][15].

Several studies have highlighted the possible benefits of using exfoliated graphene as a sieving layer to enhance hydrogen isotope separation[16][17]. In order to scale up, various strategies have been proposed for employing chemical vapor deposition (CVD) graphene in membrane applications, including the deposition of graphene on polymer

supports such as Nafion[4][5][18][19]. Several studies have reported significant hydrogen isotope selectivity using this approach, and this membrane configuration has been suggested as a potential candidate for industrial-scale applications. In 2017, a landmark study by Lozado-Hidalgo et al. focused on the separation of hydrogen isotopes proton and deuteron. The study demonstrated that a composite membrane composed of CVD graphene-embedded Nafion could efficiently separate these isotopes, exhibiting a remarkable separation factor of approximately 8 despite cracks and imperfections[5]. This study served as a catalyst, propelling further research in this domain. One such notable contribution was made by Bukola et al. in 2018, who reported a hydrogen/deuterium separation factor of about 14 using Nafion — Graphene — Nafion sandwich membranes in an electrochemical pump cell[4]. Recently Satoshi et al. reported a maximum H/D separation factor of ∼25 at 0.15 V using a heterogeneous electrode made of graphene and palladium[18]. However, none of these studies utilized decontaminated membranes after the transfer of graphene to Nafion membranes. Instead, they all followed the rinsing-after-etching procedure reported by Lozada-Hidalgo in 2017[5]. In Chapter 4 of this dissertation, we highlighted the potential for cation contamination if the membranes are not properly reprotonated or redeuterated. As we move forward, it is crucial to emphasize the importance of this step. Improper or incomplete reprotonation/redeuteration can lead to inaccuracies in H/D separation efficacy and overall membrane performance.

Despite the compelling nature of these results, they were met with substantial skepticism within the scientific community. The reproducibility and validity of the reported hydrogen isotope separation performance by CVD graphene were challenged by Xue et al. They contended that CVD graphene itself did not present any noticeable hydrogen isotope selectivity. Instead, they suggested that the observed selectivity was a consequence of the kinetic isotope effect at the catalyst layer[20].

A detailed review of the methodologies employed in these studies reveals potential complications. One of the significant concerns is the possible contamination of the membrane, particularly with copper and ammonium ions. The conventional fabrication process of graphene involves the use of copper foils, which are later removed, potentially leaving behind residual copper ions. As discussed in Chapter 4, this unintentional exchange of ammonium-copper ions can considerably affect the conductivity of Nafion membranes. As revealed in Chapter 4 of this dissertation, such contamination could significantly modify the membrane's transport properties and increase resistance towards H/D transportation across the membrane.

Also, the time-dependent behavior of proton/deuteron transport and the impact of defects and holes commonly associated with CVD graphene have been largely overlooked. These defects and holes can disrupt the uniformity and continuity of the graphene lattice, potentially compromising the selectivity and efficiency of proton/deuteron transport. Indeed, a comprehensive study by Unwin and colleagues established that the majority of the CVD graphene—Nafion membrane does not conduct protons, and when proton transmission does occur, it is primarily localized at specific sites which are believed to be the result of defects in the graphene layer[21]. Such insights underscore the importance of a thorough reevaluation of graphene's H/D selectivity using decontaminated membranes. This chapter aims to undertake this critical reevaluation, employing NGN membranes that have been meticulously decontaminated by the reprotonation/redeutearation step suggested in Chapter 4. By doing so, we aim to eliminate any confounding effects of cation contamination and provide a more accurate representation of the intrinsic properties and potential of graphene for hydrogen isotope separation.

5.3 Materials and Methods

5.3.1 Preparation of Nafion—Graphene—Nafion MEAs

All membranes utilized in this study underwent pretreatment following the procedure outlined in subsection 3.1 of Chapter 4. The NGN and Nafion—Nafion (NN) membrane assemblies were prepared using a method previously published[4]. For the NGN assembly, graphene deposited on copper sheets via CVD was procured from ACS Materials LLC. These copper—graphene sheets were placed on Nafion 211 and hot-pressed at 140 °C and 600 psi pressure for 3 minutes. Following hot-pressing, the copper—graphene—Nafion membrane composites were submerged in a 0.3 M Ammonium Persulfate (APS) solution for 8-10 hours for copper etching. After etching, the membranes were rinsed with Deionized Water (DI water) or D_2O and allowed to dry at room temperature. A second piece of Nafion 211 (in H or D form) was then hot-pressed onto the graphene-containing Nafion membrane under the same conditions to form the desired sandwich-like structure.

For the NN assembly, the preparation was simpler: two Nafion 211 membranes (in H or D form) were hot-pressed together under the same conditions. Once the sandwich-like membranes were ready, they were converted into MEAs by hot-pressing two 0.178 cm^2 disk-shaped Pt/C cloth electrodes onto either side of each membrane. This process sealed the membrane between the two electrodes under the same hot-pressing conditions, thus completing the MEA preparation.

5.3.2 Preparation of Decontaminated NGN MEAs

The preparation of decontaminated NGN membranes forms a crucial part of our methodology. To eliminate the possibility of residual copper and ammonium con-
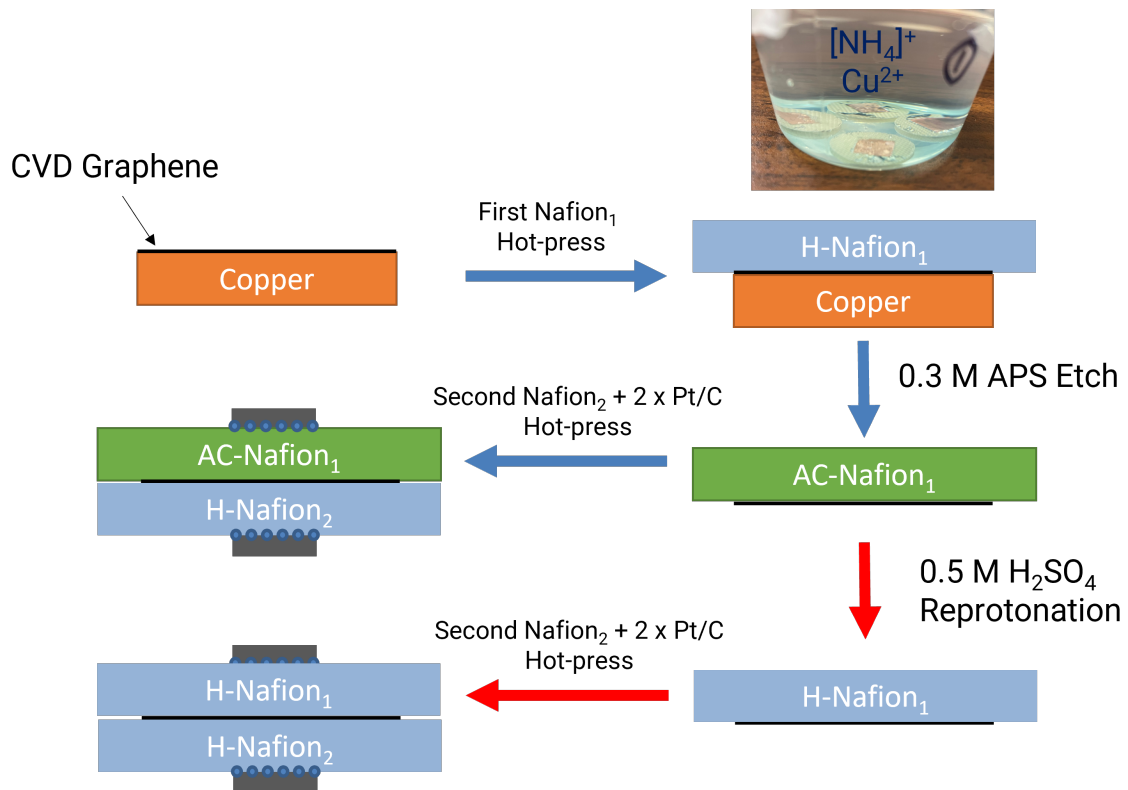
Figure 5.1: NGN Fabrication Method: A comparison of the procedure outlined by Bukola et al.[4] with the supplementary steps proposed in Chapter 4.

tamination from the preparation processes, we executed a cation exchange procedure to reprotonate or redeuterate the membranes. Post copper etching and rinsing with H_2O/D_2O, as described in subsection 3.1 of this chapter, the Graphene—Nafion membrane composites were immersed in either a 0.5 M H_2SO_4 in H_2O solution or a 0.5 M D_2SO_4 in D_2O solution for 8 hours. After being immersed in either solution, the composites were rinsed with H_2O/D_2O to remove any residual acid. They were then air-dried at room temperature. Subsequently, a second piece of Nafion was attached, along with Pt/C electrodes, to fabricate the MEAs, following the same procedure as in subsection 3.1 of this chapter.

5.3.3   Proton Exchange Membrane (PEM) Cell Assembly

The procedure for the assembly of the PEM cell is detailed in subsection 3.3 of Chapter 4. It involves the integration of the prepared MEAs into a custom-built, swage-style fuel cell and the preparation of reactant gases for H-pump and D-pump experiments.

5.3.4   D-Pump Time-Dependent Resistance Analysis

Multiple cyclic voltammetry (CV) scans were conducted at a rapid scan rate of 20 mV/s on both NGN and NN membranes in the D-pump cell. Our findings revealed a higher initial resistance to deuteron transport in the NGN membranes as compared to the NN ones. Moreover, while the resistance in NN membranes remained relatively steady over time, the resistance in NGN membranes displayed a gradual decrease as more CV scans were performed, suggesting a time-dependent behavior.

5.3.5 Amperometric Analysis under Interchanging Hydrogen and Deuterium Feed Gases

This step, detailed in subsection 3.4 of our Chapter 4, involves conducting amperometric analysis on both NGN and NN MEAs with an alternating feed gas strategy. The interchanging of humidified deuterium and hydrogen gases as input feed helped to scrutinize the dynamic resistance behavior of our membranes.

5.4 Results and Discussion

In an effort to assess the performance of our membranes under realistic operating conditions, we strictly adhered to the experimental procedure detailed by Bukola et al. with a particular emphasis on the D-pump setup. After replicating this procedure and performing CV measurements, as illustrated in Figure 5.2, we observed a higher initial resistance (manifested as lower current) for deuteron transport through the NGN membrane. In contrast, the NN membrane exhibited lower resistance (resulting in a higher current). This finding is consistent with the observations reported in Bukola et al.'s original study[4].

In subsequent CV segments, we noted that the resistance values for the NN membrane remained relatively constant. However, in the case of the NGN membrane, we observed a notable increase in current with each additional CV segment. This suggests an interesting enhancement in the transport properties of the NGN membrane over time. We took a step further to investigate the time-dependent resistance changes in the membranes, a crucial aspect that was not previously addressed in the literature.

Amperometric experiments conducted at a fixed applied potential of -70 mV
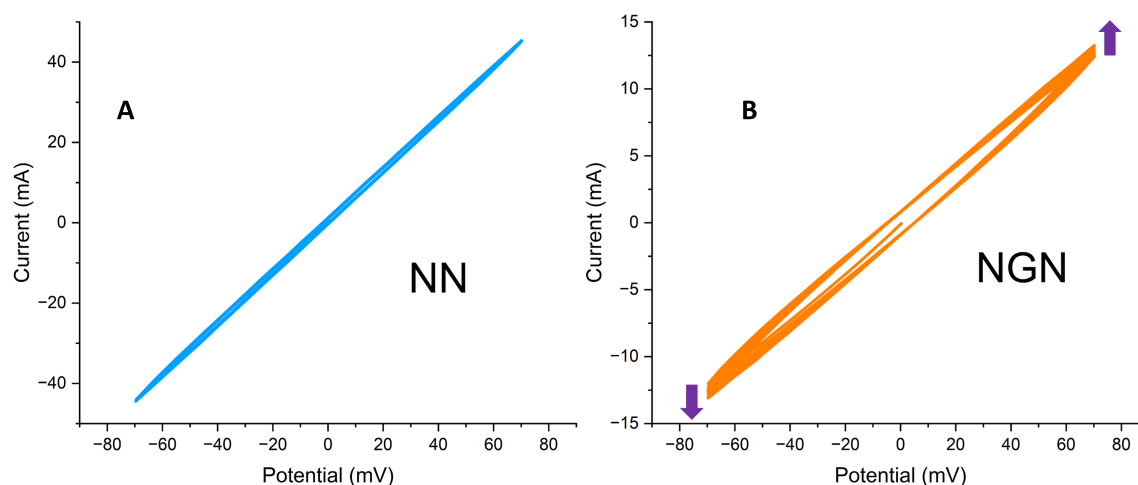
Figure 5.2: CV Scan Comparisons Between NN and NGN Membranes (prepared using the conventional procedure) for D-pumping: These side-by-side graphs represent the CV scans conducted on both NN and NGN membranes at a rapid scan rate of 20 mV/s. A. presents the results for NN membranes, where the consistent current indicates steady resistance to deuteron transport over time. In contrast, B. demonstrates the outcomes for NGN membranes. Here, multiple segments portray a time-dependent behavior, with a gradual increase in current and a corresponding decrease in resistance over time.

on NGN MEA prepared following the previous procedures provided further insights. These tests were executed while alternating between deuterium and hydrogen feed gases. As shown in figure 5.3, higher resistances were observed for both D and H transport in the NGN membrane compared with the similar experiment conducted NN membrane in Chapter 4, with an especially high initial resistance observed for deuterium transport. This initial resistance progressively decreased over time. A transition to a hydrogen gas feed resulted in a sharp drop in resistance to a steady-state resistance of approximately 3.1 ohms. Interestingly, when switching back to a deuterium gas feed, the resistance increased but did not revert to the initially elevated level. In contrast to similar amperometric experiment discussed in Chapter 4 for NN membrane, the NGN membranes displayed a different pattern of resistance. Higher resistances were observed for both D and H transport in the NGN membranes as
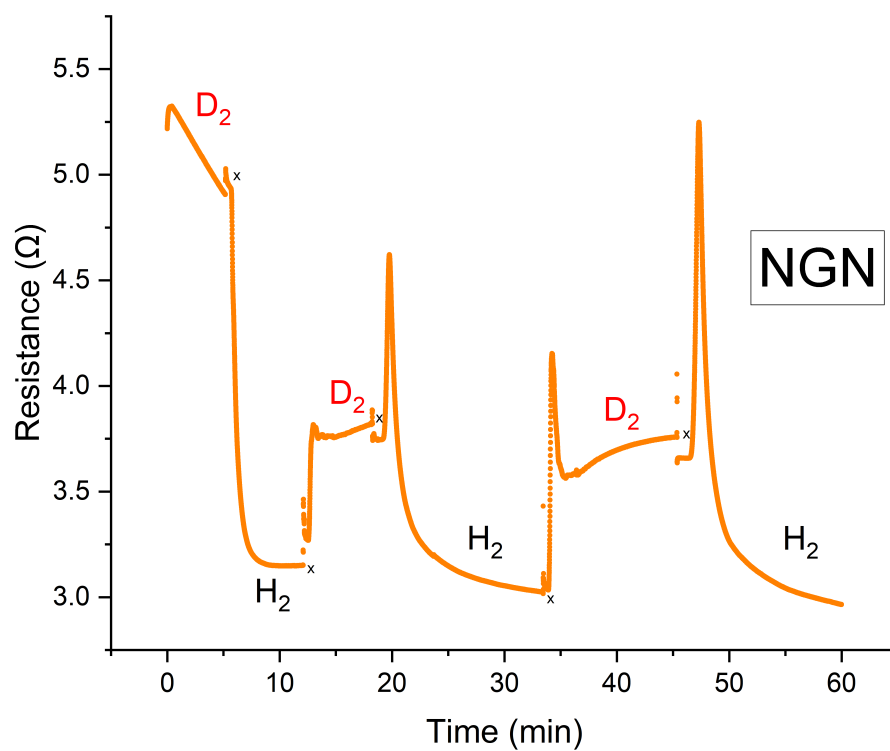
Figure 5.3: Amperometric Resistance Analysis of NGN MEA under Alternating Feed Gas Strategy. This graph illustrates the changes in resistance of NGN MEA subjected to chronoamperometry at a fixed potential of -70 mV.
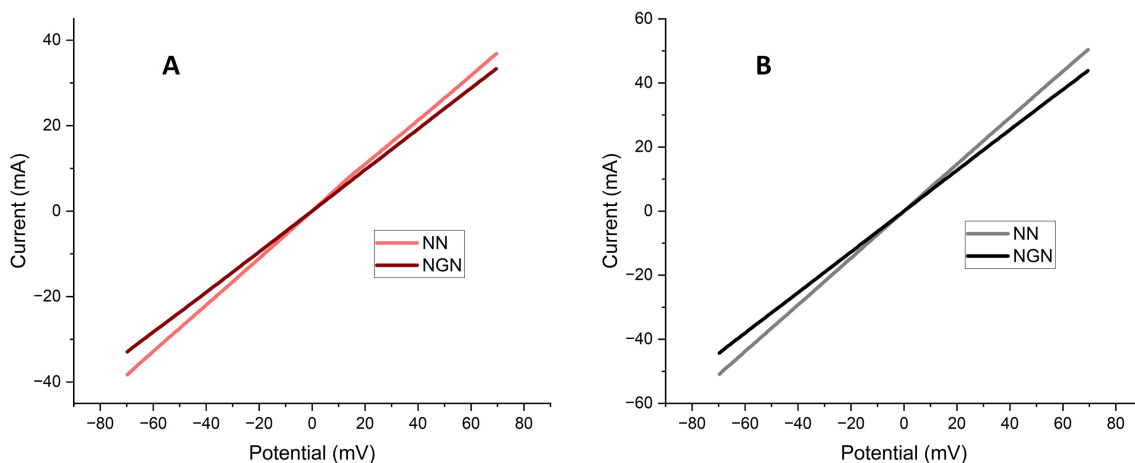
Figure 5.4: Comparative Analysis of Post-Treated Linear Sweep Voltammetry (LSV) Curves for H-Pump and D-Pump Experiments Using NGN and NN MEAs. These side-by-side graphs illustrate the LSV curves of post-treated NGN and NN MEAs under both H-pump and D-pump conditions, highlighting changes in resistance and, consequently, conductance. A. shows the comparison for D-pump conditions, with distinct lines representing the LSV curves for NGN and NN MEAs. Similarly, B. depicts the comparison for H-pump conditions, using unique lines to differentiate the LSV curves for NGN and NN MEAs.

compared to the NN ones.

Subsequent measurements of graphene's H/D areal conductance ratio from NGN and NN amperometric data (calculated similarly to the method represented in Table 5.1) at steady-state conditions revealed a value of approximately 1.1, indicative of a transient isotope selectivity in these MEAs. This observation, combined with our temporal analysis of deuteron transport resistance, suggests that a critical reassessment of the efficacy and selectivity of graphene-embedded Nafion membranes for hydrogen isotope separation is warranted.

"In Figure 5.4, we present LSV curves recorded for both NGN and NN MEAs after undergoing reprotonation/redeuteration treatment, aiming to evaluate their performance concerning isotope selectivity. We derived resistance values for each MEA from these LSV curves, as depicted in Figure 5.5. This allowed us to systematically
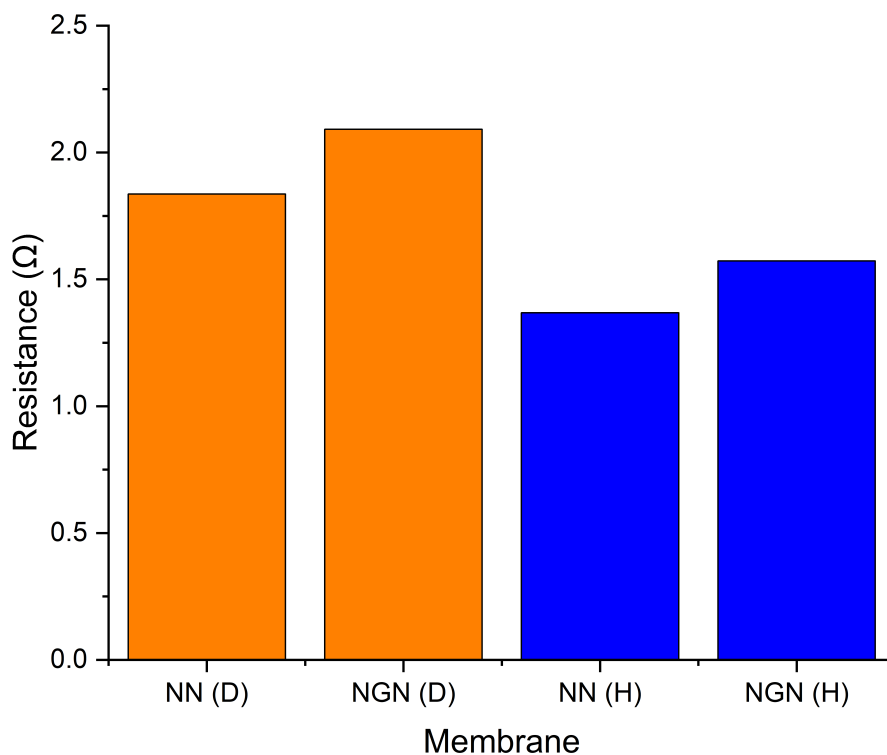
Figure 5.5: Comparison of Calculated Resistances for Post-Treated NGN and NN MEAs in H-Pump and D-Pump Experiments. This graph presents the calculated resistances derived from the LSV curves of post-treated NGN and NN MEAs under both H-pump and D-pump conditions.

Table 5.1: Determination of Graphene's Area Conductance for Proton and Deuteron Transport. This table compiles resistance data derived from the LSV curves presented in Figures 5.4A and 5.4B, comparing the performance of NN and NGN membranes in both H and D forms. The graphene's resistance is calculated by subtracting the resistance of NN from that of NGN. The active area of the electrode is used to derive the area resistance and area conductance of the graphene.

	Sample	Resistance Ω	Graphene's Resistance Ω	Graphene area resistance Ω cm^2	Graphene area conductance S cm^{-2}
Proton form	NN	1.37			
	NGN	1.58	0.21	0.03738	27
Deuteron form	NN	1.85			
	NGN	2.1	0.25	0.0445	23

88

discern the graphene's impact on both H and D transport and thereby ascertain its specific role in the proton exchange membrane. Comprehensive calculations are provided in Table 5.1. This evaluation entailed subtracting the resistances of NN from the NGN under both H-pump and D-pump scenarios. We then transformed these resistance values into conductance metrics, as outlined in Table 5.1. Our findings indicate the area conductance of graphene to be approximately 27 S cm^2 for H transport and 23 S cm^2 for D transport. In comparison, Bukola et al. reported values of 29 S cm^2 for H transport and a notably lower 2 S cm^2 for D transport for a similar experiment in 2018[4].

Our findings led us to a significant reevaluation of H/D isotope selectivity. Unlike previous studies, which reported substantial isotope selectivity factors of 8[5] and 14[4] for CVD graphene integrated with Nafion in H/D separation, we observed a lower selectivity factor of approximately 1.2 suggesting that NGN membranes do not favor the transport of H over D. Significantly, our results are based on membranes treated with a reprotonation/redeuteration process to remove potential cations like ammonium and copper introduced during the graphene transfer onto Nafion—a step not considered in earlier reports. Our results intimate that the H/D selectivity for CVD graphene in past research might have been inadvertently influenced by the presence of ammonium and copper cations within Nafion's ion exchange sites. The omission of an additional acid wash might allow residual cations to exchange within the Nafion layer, potentially elevating the resistance values measured for both H and D transport. Moreover, as detailed in subsection 5.3 of Chapter 7, the imperfections and cracks introduced during the etching process could significantly influence H/D transport across the membrane, allowing both to pass without any preferential treatment.

Our findings call into question the prevailing perception of CVD graphene's

Table 5.2: Comparison of Experimental Results for H/D Separation by the Graphene Sieving Membrane

Reference	Membrane	Graphene Scale	Cathodic Electrode	SF (H/D)	Measurement Method
Geim's group 2016[17]	N—G—N	Exfoliation, 2-10 μm circle	Decorated 2 nm Pt	$\sim$10	Electrical Conductivity
Geim's group 2016[17]	N—G	Exfoliation, 50 μm circle	Decorated 2 nm Pt	$\sim$10	QMS
Geim's group 2017[5]	N—G	CVD, 1 sq. inch	Decorated 2 nm Pt	$\sim$8	QMS
Bukola et al. 2018[4]	N—G—N	CVD, 0.178 cm^2	Ink-coated Pt	$\sim$14	Electrical Conductivity
Xue et al. 2022[20]	N—G	CVD, 4 cm^2	Decorated 2 nm Pt	$\sim$1.15	OA-ICOS
Xue et al. 2022[20]	N—G—N	CVD, 4 cm^2	Ink-coated Pt	$\sim$1.08	OA-ICOS
Present work (Chapter 5)	N—G—N	CVD, 0.178 cm^2	Ink-coated Pt	$\sim$1.1-1.2	Electrical Conductivity
Present work (Chapter 7)	N—G—N	CVD, 0.178 cm^2	Ink-coated Pt	$\sim$1.0-1.2	QMS

proton selectivity. The high H/D selectivity championed in current literature may be more attributable to inadvertent cation contamination during membrane preparation than to an intrinsic property of CVD graphene. Consequently, our data stress the paramount importance of maintaining purity during membrane preparation and fabrication. This revelation has profound real-world implications, emphasizing the need for meticulous experimentation and robust control measures when investigating the transport behavior of H and D in graphene-embedded Nafion membranes.

Hence, our research advocates for a thoughtful reevaluation of the current methodologies used in graphene-based proton-deuterium separation, underscoring the need for efficient decontamination approaches. We anticipate that our findings will prompt the scientific community to revisit protocols that involve graphene in such applications, leading to a more elaborate comprehension of its role.

5.5 Conclusions

Our study provides critical insights into the proton transport behavior of graphene-embedded Nafion membranes, particularly in the context of hydrogen isotope separation. We meticulously analyzed the performance and characteristics of

NGN membranes, contrasting them with standard NN membranes under various conditions, including H-pump and D-pump settings.

One of the crucial findings of our research revolves around the often-overlooked factor of contamination during membrane fabrication. We discovered that the presence of ammonium and copper cations in the membranes, an inadvertent byproduct of previous experimental protocols, significantly impacts the performance and apparent properties of the graphene layer in the membrane. By developing and implementing a post-treatment procedure, we effectively removed these contaminants from the membrane, reverting it back to its intended hydrogen or deuterium form.

Upon decontamination, we observed a drastic shift in the performance characteristics of the NGN membranes. When we subtracted the resistance values of the NN membranes from the NGN membranes under H-pump and D-pump conditions and converted these to conductance values, we measured the graphene's area conductance to be 27 S cm^2 for H transport and 23 S cm^2 for D transport. This resulted in an H/D isotope selectivity of approximately 1.17, starkly contrasting the previously reported selectivity factors of 8 and 14.

These findings fundamentally challenge the prevailing understanding of the proton selectivity of graphene within proton exchange membranes. The previously reported high H/D selectivity ratios for graphene could be an artifact of experimental contamination rather than an inherent feature of graphene.

Our research underscores the need for comprehensive control experiments in studies of this nature, particularly given the sensitivity of graphene-embedded Nafion membranes to cationic contamination. Furthermore, the results suggest a need to reevaluate the perceived superiority of graphene's proton selectivity in these membranes. This is crucial for the development of more accurate and efficient methodologies in the field of hydrogen isotope separation and, by extension, in the broader

realm of sustainable energy solutions.

In conclusion, this study contributes significantly to our understanding of the actual proton transport behavior in graphene-embedded Nafion membranes. We hope these findings will encourage further rigorous experimentation and innovation in this field, fostering deeper insights and advances in membrane technology for hydrogen isotope separation.

References

(1) Kim, J. Y.; Oh, H.; Moon, H. R. *Advanced Materials* **2019**, *31*, 1805293.

(2) Liu, M. et al. *Science* **2019**, *366*, 613–620.

(3) Oh, H.; Savchenko, I.; Mavrandonakis, A.; Heine, T.; Hirscher, M. *ACS Nano* **2014**, *8*, 761–770.

(4) Bukola, S.; Liang, Y.; Korzeniewski, C.; Harris, J.; Creager, S. *Journal of the American Chemical Society* **2018**, *140*, 1743–1752.

(5) Lozada-Hidalgo, M.; Zhang, S.; Hu, S.; Esfandiar, A.; Grigorieva, I. V.; Geim, A. K. *Nature Communications* **2017**, *8*, 15215.

(6) Geim, A. K.; Novoselov, K. S. *Nature Materials* **2007**, *6*, 183–191.

(7) Tiwari, S. K.; Sahoo, S.; Wang, N.; Huczko, A. *Journal of Science: Advanced Materials and Devices* **2020**, *5*, 10–29.

(8) Sun, Z.; Chang, H. *ACS Nano* **2014**, *8*, 4133–4156.

(9) Liao, L.; Lin, Y.-C.; Bao, M.; Cheng, R.; Bai, J.; Liu, Y.; Qu, Y.; Wang, K. L.; Huang, Y.; Duan, X. *Nature* **2010**, *467*, 305–308.

(10) Li, X.; Yu, J.; Wageh, S.; Al-Ghamdi, A. A.; Xie, J. *Small* **2016**, *12*, 6640–6696.

(11) Li, X.; Shen, R.; Ma, S.; Chen, X.; Xie, J. *Applied Surface Science* **2018**, *430*, 53–107.

(12) Yoon, H. J.; Jun, D. H.; Yang, J. H.; Zhou, Z.; Yang, S. S.; Cheng, M. M.-C. *Sensors and Actuators B: Chemical* **2011**, *157*, 310–313.

(13) Li, W.; Geng, X.; Guo, Y.; Rong, J.; Gong, Y.; Wu, L.; Zhang, X.; Li, P.; Xu, J.; Cheng, G.; Sun, M.; Liu, L. *ACS Nano* **2011**, *5*, 6955–6961.

(14) Guo, F.; Silverberg, G.; Bowers, S.; Kim, S.-P.; Datta, D.; Shenoy, V.; Hurt, R. H. *Environmental Science Technology* **2012**, *46*, 7717–7724.

(15) Prasai, D.; Tuberquia, J. C.; Harl, R. R.; Jennings, G. K.; Bolotin, K. I. *ACS Nano* **2012**, *6*, 1102–1108.

(16) Hu, S.; Lozada-Hidalgo, M.; Wang, F. C.; Mishchenko, A.; Schedin, F.; Nair, R. R.; Hill, E. W.; Boukhvalov, D. W.; Katsnelson, M. I.; Dryfe, R. A. W.; Grigorieva, I. V.; Wu, H. A.; Geim, A. K. *Nature* **2014**, *516*, 227–230.

(17) Lozada-Hidalgo, M.; Hu, S.; Marshall, O.; Mishchenko, A.; Grigorenko, A. N.; Dryfe, R. A. W.; Radha, B.; Grigorieva, I. V.; Geim, A. K. *Science* **2016**, *351*, 68–70.

(18) Yasuda, S.; Matsushima, H.; Harada, K.; Tanii, R.; Terasawa, T.-o.; Yano, M.; Asaoka, H.; Gueriba, J. S.; Diño, W. A.; Fukutani, K. *ACS Nano* **2022**, *16*, 14362–14369.

(19) Bukola, S.; Beard, K.; Korzeniewski, C.; Harris, J. M.; Creager, S. E. *ACS Applied Nano Materials* **2019**, *2*, 964–974.

(20) Xue, X.; Chu, X.; Zhang, M.; Wei, F.; Liang, C.; Liang, J.; Li, J.; Cheng, W.; Deng, K.; Liu, W. *ACS Applied Materials amp; Interfaces* **2022**, *14*, 32360–32368.

(21) Bentley, C. L.; Kang, M.; Bukola, S.; Creager, S. E.; Unwin, P. R. *ACS Nano* **2022**, *16*, 5233–5245.

Chapter 6

Real-Time Analysis of Electrochemically Evolved Gases: Design, Operation, and Applications of an Integrated OEMS System

6.1   Abstract

This chapter presents a comprehensive guide on the design and utilization of an online electrochemical cell coupled with a quadrupole mass spectrometer system for the real-time analysis of electrochemically evolved gases with an emphasis on hydrogen gases. The importance and the pivotal role of such systems in the field of energy technology and environmental science are outlined, highlighting the significance of studying evolved gases from electrochemical reactions. We describe the

95

components of our system, their functions, and the rationale behind their selection and configuration. A detailed account of our experimental setup and calibration procedures, as well as the safety measures taken, provides the reader with a firm grasp of the operational details. Emphasizing the real-time data acquisition capability of our OEMS system, we further explore the data analysis techniques employed and the subsequent results obtained. The analysis revealed consistent and accurate results, demonstrating the system's proficiency and robustness. The potential of this system to contribute to hydrogen-based technologies and renewable energy is also examined. We conclude with a contemplative discussion on the system's limitations, suggesting areas for future work and novel applications, ultimately underlining the OEMS system's promising potential in this research field.

6.2 Introduction

Electrochemical processes, foundational in disciplines such as chemistry, biology, and energy, yield essential metrics like potential and current. However, the inherent intricacy of these reactions necessitates more sophisticated instruments to elucidate molecular details. Mass spectrometry (MS) complements this need with its quick detection and structural discernment capabilities[1][2]. The innovative blend of these techniques, Electrochemical Mass Spectrometry (EC-MS), facilitates real-time reaction insights. Its origins date back to 1971[3], with later developments like the differential electrochemical mass spectrometry (DEMS) method in 1984 bolstering its capabilities[4]. As the field evolved, a plethora of EC-MS (including DEMs and OEMS) devices surfaced, expanding its applicability[5][6][7][8][9][10][11].

In a world gravitating towards efficient and sustainable energy solutions, the ability to monitor and interpret gaseous products in real time has gained paramount

96

importance. Such evolved gases often provide insights into underlying reaction mechanisms and potential efficiency bottlenecks[12]. Coupling electrochemistry with tools like GC[13][14], HPLC[15], FTIR[16][17], and MS[18][19] has proven instrumental, especially in identifying gases and volatiles during electrochemical reactions.

Traditional analytical techniques, effective in their own right, sometimes struggle to capture the complex dynamics of electrochemical gas evolution. The fusion of EC and MS offers an unparalleled insight into this realm. While methods such as gas chromatography and infrared spectroscopy face constraints related to time and complexity, one of EC-MS's standout attributes is its ability for real-time, in-situ monitoring of reaction products[20]. This eliminates the cumbersome step of transferring samples to external analytical instruments, thus reducing risks like sample contamination or loss and bolstering measurement reliability. This negates the need for cumbersome external transfers to analytical instruments, minimizing risks like sample contamination or loss, and enhancing the reliability of measurements. One of its most distinct benefits is the capability for real-time data acquisition. By capturing swift changes in gas evolution, EC-MS provides a unique perspective on reaction kinetics, highlighting transient events that might be overlooked by other methods[21].

When an electrochemical hydrogen pump cell is paired with a quadrupole mass spectrometer, the resulting OEMS demonstrates unparalleled sensitivity to low-mass gases, positioning it as an ideal tool for analyzing H_2, D_2, and HD[22]. In essence, OEMS provides a dynamic, efficient, and profound avenue for understanding the complexities of electrochemically evolved hydrogen isotopes[23].

In this chapter, we delve deep into the design, operation, and applications of our custom-built OEMS system, tailored for the comprehensive analysis of electrochemically evolved hydrogen isotopes. Our OEMS system merges an electrochemical hydrogen/deuterium pump cell with the Extrel MAX300-CAT Quadrupole Mass

Spectrometer (QMS). This combination promises unparalleled precision in studying hydrogen isotopes (H_2, D_2, and HD), with its speed, sensitivity, and extensive mass range standing as its defining traits, capturing real-time reactions with unmatched clarity. With a detection limit of 50 ppb and the capability to measure changes in sample concentration in less than 300 ms, the system ensures reaction dynamics are captured in real-time, shedding light on every intricate detail. Furthermore, allowing data acquisition rates up to a staggering 1000 measurements per second enhances this real-time analysis capability[24].

In this chapter we present an overview of our OEMS system, highlighting its components and functionalities. We also delve into our calibration and experimental methodologies. Through this exposition, we aim to provide a clear understanding of our system's capabilities in real-time analysis of evolved hydrogen isotopes. We hope this insight offers a meaningful contribution to the ongoing discourse in hydrogen-based technologies, touching upon areas like energy storage, fuel cells, and the broader context of electrochemical synthesis.

6.3   Materials and Methods

6.3.1   Extrel MAX300-CAT Quadrupole Mass Spectrometer: Description, Operation, and Advantages

Our OEMS system prominently features the Extrel MAX300-CAT QMS, an instrument specifically designed for high-speed analysis of low-mass gasses such as H_2, D_2, and HD. It is equipped with an electron impact (EI) ionizer, facilitating the ionization of any gas or vapor sample, including low-mass gases. The QMS includes both Faraday and electron multiplier detectors. This instrument provides
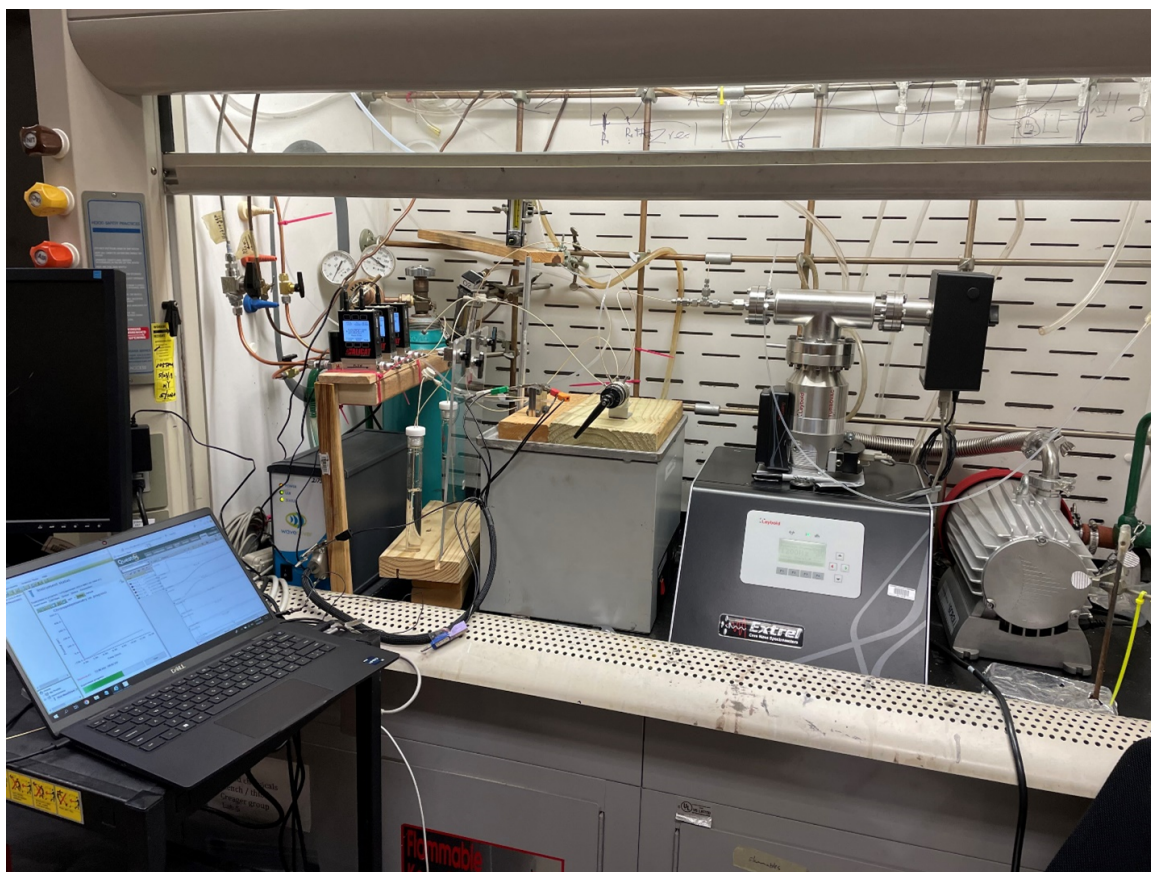
Figure 6.1: The photo provides a view of the integrated Online Electrochemical Mass Spectrometry (OEMS) system housed within the fume hood. Key components showcased include the Extrel MAX300-CAT Quadrupole Mass Spectrometer, the Pine Research WaveDriver 20 Potentiostat, the mass flow controllers (MFCs), and the electrochemical H/D pump cell, which are vital components for our real-time, continuous monitoring of hydrogen isotope evolution.
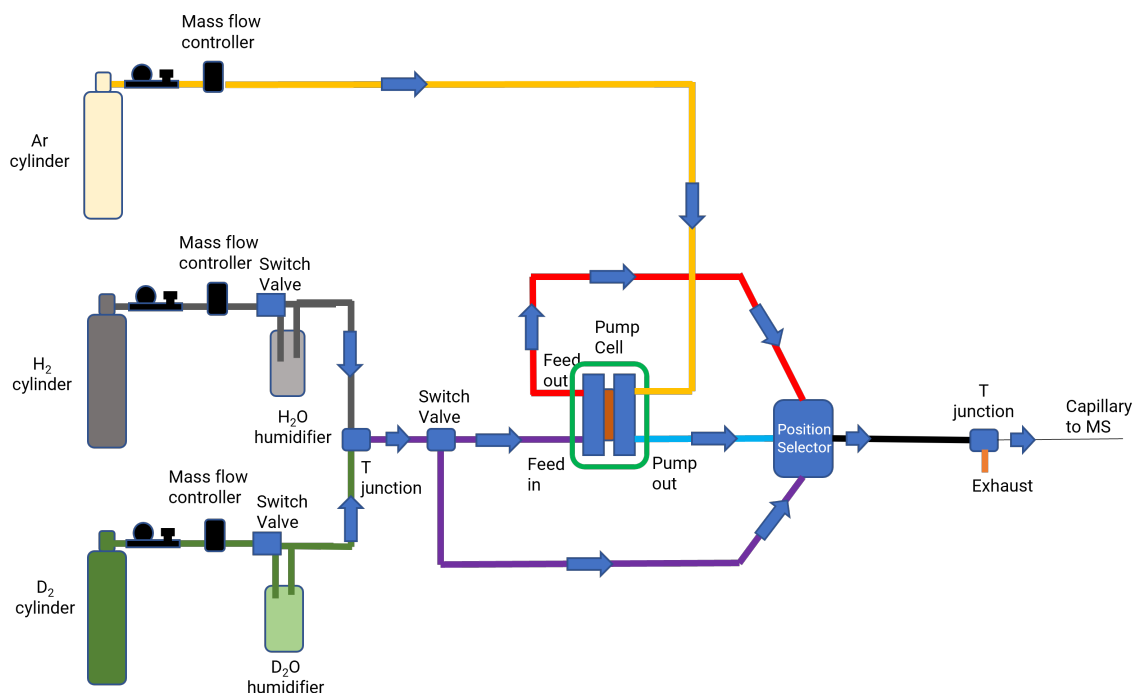
Figure 6.2: OEMS System: A Schematic Illustration of the Online Electrochemistry Mass Spectroscopy Setup.

a wide dynamic range, stretching from $1x10^{-6}$ to $5x10^{-13}$ Torr (100% to 0.5 ppm), with a low detection limit of 50 ppb. The broad detection range and high sensitivity ensure that even trace amounts of isotopes can be accurately identified and quantified in the gas mixtures. With the capacity to perform up to 1000 measurements per second, the MAX300-CAT is optimally suited for monitoring rapid, dynamic changes in gas evolution. This high-speed operation is essential for providing real-time data, contributing to a detailed understanding of reaction kinetics. The MAX300-CAT is impressively efficient, requiring a minimal sample volume of 10 μL/min. In addition, the ionization energy can be adjusted to reduce fragmentation, ensuring the integrity of the spectral data, and providing more reliable identification and quantification of our target gases.

With a 6 mm quadrupole mass filter, the MAX300-CAT offers mass range

options from 1-100 amu. This flexibility ensures high-resolution separation of a wide range of mass-to-charge ratios, including those of our target gases – H_2, D_2, and HD. In summary, the MAX300-CAT QMS provides a high-resolution, high-speed, and sensitive means to real-time analysis of low-mass gases, crucial for our studies of hydrogen isotope evolution.

6.3.2 Mass Flow Controllers and Tubing: Selection, Operation, and Benefits

Critical to our OEMS system, MFCs control the flow rates of gases, H_2, D_2, and Ar, into the electrochemical cell and QMS, ensuring experimental consistency. We selected Alicat MC-Series Gas Mass Flow Controllers for our setup, given their compatibility with H_2, D_2, and Ar gases, full-scale range of 0-20 SCCM accommodating our low flow rates, standard accuracy of $\pm 0.6\%$ of reading or $\pm 0.1\%$ of full scale, response time of 30 ms, and ease of integration. Alicat mass flow instruments primarily use laminar differential pressure technology to measure mass flow rates of gasses, converting turbulent flow to laminar, measuring the pressure drop, and then calculating both the volumetric and standardized mass flow rates[25].

To ensure reliable gas transfer, we used 1/16th-inch PEEK (polyetheretherketone) tubing, a chemically resistant, durable thermoplastic with low gas permeability. Its resistance to strong acids, bases, organic solvents, and low permeability are essential for transporting hydrogen and deuterium gases without risk of corrosion, chemical degradation, or sample loss. Its mechanical durability promises robust, long-lasting performance. The incorporation of Alicat MC-Series MFCs and PEEK tubing into our OEMS system enhances precision and reliability in our hydrogen isotope evolution investigations.

6.3.3 Electrochemical Cell: Design, Components, and Function

Our experiment utilizes a custom-built electrochemical cell for electrochemical hydrogen/deuterium pumping and MS analysis of evolved gases. It is a two-compartment design, separated by a proton exchange membrane (PEM), ensuring isolation of anode and cathode compartments. The anode and cathode are composed of 2 mg/cm^2 Pt/C and supported by AvCarb P50 Gas Diffusion Layer (GDL), facilitating uniform gas distribution and efficient reactions. These carbon-based Gas Diffusion Electrodes (GDEs) coated with platinum catalysts offer superior electrical conductivity, chemical stability, and catalytic activity. The Nafion 211 PEM facilitates proton transport while insulating electrons, which is crucial for separate electrochemical reactions at the anode and cathode. It was chosen for its excellent proton conductivity, chemical stability, and mechanical durability. Titanium plates act as current collectors, efficiently transporting electrical current due to their high electronic conductivity and corrosion resistance[26].

Gas inlets allow the controlled delivery of H$_2$ and D$_2$ gases at a flow rate of 10 SCCM each into the anode compartment. To enhance proton and deuteron conductivity, gases are bubbled through water and D$_2$O, respectively, to achieve a ~95% relative humidity condition. It takes roughly 5-7 minutes for humidified gases to be fed to the cell to achieve steady-state ion transport through the membrane. The high humidity promotes efficient electrochemical reactions by facilitating ion mobility through the electrolyte. The outlets are connected to the mass spectrometer for evolved gas analysis, and the output gas mixture is carried by 20 SCCM of Argon gas. In the experimental setup, we employed chronopotentiometry, applying a constant -40 mA current using the PineResearch WaveDriver 20. The application of constant

current in chronopotentiometry is used to maintain a constant flux of evolved gasses, which facilitates the use of MS to analyze the gas composition, offering reliable observations of gas evolution and invaluable insights into underlying reaction mechanisms.

In summary, the design, components, and functionality of the electrochemical cell are integral to the success of our evolved gas analysis, enhancing the system's overall capability and reliability.

6.3.4 Calibration Process, Role of Argon, and Its Importance for Data Accuracy

Table 6.1: Input H_2 and D_2 gas mixtures for the calibration of OEMS. The mixtures were created in different ratios (90:10, 80:20, 70:30, and so on, up to 10:90) using mass flow controllers. Each mixture maintained a total flow rate of 2 SCCM. For example, a 90:10 H_2:D_2 mixture was prepared by combining 1.8 SCCM of H_2 with 0.2 SCCM of D_2. A consistent flow of 20 SCCM Argon was used as a carrier gas to transport each of these mixtures to the QMS.

D_2 Flow Rate SCCM (±0.02)	H_2 Flow Rate SCCM (±0.02)	D_2 Concentration %	H_2 Concentration %
0.20	1.80	10	90
0.40	1.60	20	80
0.60	1.40	30	70
0.80	1.20	40	60
1.00	1.00	50	50
1.20	0.80	60	40
1.40	0.60	70	30
1.60	0.40	80	20
1.80	0.20	90	10

Our Extrel MAX300-CAT QMS was calibrated using varying mixtures of H_2 and D_2 gases, ranging from a 90:10 to a 10:90 H_2:D_2 ratio. During this process, we set the relative sensitivities for H_2 and D_2 as 0.44 and 0.35, respectively, based on standard values from the PFEIFFER VACUUM MS Catalog. All calibration

mixtures were transported to the MS using 20 SCCM of Argon gas. The gas mixtures were changed sequentially, starting from a 90:10 ratio and progressing to 10:90, as detailed in Table 6.1. Each mixture was switched to the next only after achieving steady-state signals for the relative intensity/concentration graphs displayed by the Questor 5 software. Relative Intensity and Concentration (%) vs Time plots were obtained from the Questor 5 software and are displayed in Figures 6.4A and 6.4B. The concentrations (%) shown in Figure 6.4B are automatically calculated/detected by the instrument based on the sensitivity values. Calibration curves (CCs) depicted in Figures 6.5A and 6.5B were derived from the known input gas values, specifically the flow rates of H_2 and D_2, which determine the concentration (%), plotted against the MS-detected Relative Intensity and Concentration (%).

Since we only had H_2 and D_2 gas tanks available, we used an alternative approach to estimate HD's sensitivity. The output gas mixtures emitted from the Pt/C - Nafion x 2 - Pt/C MEA mounted in an electrochemical hydrogen pump cell contained only HD, H_2, and D_2 gasses. As illustrated in Figures 6.5A and 6.5B, after accurately calibrating the H_2 and D_2 gases, we determined the HD percentage by computing the residual value: 100 - (H_2% + D_2%). Using a modeling approach, we derived a relative sensitivity value of 0.42 for HD. This value yielded the best-fit curve for the estimated HD%, which was also derived from 100 - (H_2% + D_2%).

$$A = \frac{RI^{H_2}}{0.44}, \qquad B = \frac{RI^{D_2}}{0.35}, \qquad C = \frac{RI^{HD}}{x}$$

$$100 = \left(\frac{A}{A+B+C}\right)100 + \left(\frac{B}{A+B+C}\right)100 + \left(\frac{C}{A+B+C}\right)100$$

$$m = \left(\frac{A}{A + B + C} \right) 100$$

$$n = \left(\frac{B}{A + B + C} \right) 100$$

$$o = \left(\frac{C}{A + B + C} \right) 100$$

In this model, RI^{H_2}, RI^{D_2}, and RI^{HD} represent the relative intensities of the peaks at 2, 4, and 3 m/z, respectively. As evident from Figures 6.6C, 6.6D, and 6.6E, we achieved the best-fit curves when x = 0.42.

These sensitivity values reflect the varying responses of the QMS to these gases, a crucial factor in the interpretation and accuracy of the data. The calibration curves developed for H_2 and D_2, adjusted for their specific sensitivities, enable precise determination of evolved gas compositions in our experiment. Argon, selected as the carrier gas for evolved gases due to its inertness and unique mass-to-charge ratio, was used at a flow rate of 20 SCCM. The calibration process and use of Argon as a carrier gas are crucial for data accuracy and system performance. By establishing a relationship between physical quantities and output signals, calibration allows us to interpret meaningful physical quantities from the QMS output. Furthermore, regular calibration accounts for potential drift due to temperature fluctuations, component aging, or changes in ambient conditions, ensuring consistent and accurate results, especially vital when dealing with low-concentration gas mixtures.

6.4 Data Acquisition and Safety Measures

6.4.1 Real-Time Data Acquisition

Real-time data acquisition played a critical role in the experiment, providing immediate feedback, facilitating dynamic alterations in the experiment parameters, and allowing continuous validation of data. This process enhanced the temporal resolution, enabling the monitoring of gas composition changes over time. If there were any discrepancies in the observed and expected gas concentrations, we were able to quickly identify and rectify the issue due to the real-time data acquisition.

6.4.2 Safety Measures and Considerations

Safety and data integrity were paramount during data acquisition. As Hydrogen and Deuterium are flammable and Argon is an asphyxiant, cylinders storing these gases were handled with caution and placed in well-ventilated areas. Their flow rates were carefully controlled to avoid hazardous situations. Further safety measures included housing the OEMS setup consistently within a fume hood, providing an additional layer of protection against potential gas emissions. All electrical equipment was properly grounded to prevent electrical hazards. The laboratory personnel were equipped with appropriate personal protective equipment (PPE) such as lab coats, gloves, and safety glasses during the handling of gases and operation of high-precision instruments. Regular calibration of the Quadrupole Mass Spectrometer was maintained to ensure accurate data acquisition. The data acquisition software was programmed to automatically record and save data at regular intervals, safeguarding against data loss in the event of a system crash or power loss. These safety and integrity measures ensured a safe experimental environment while maintaining reliable
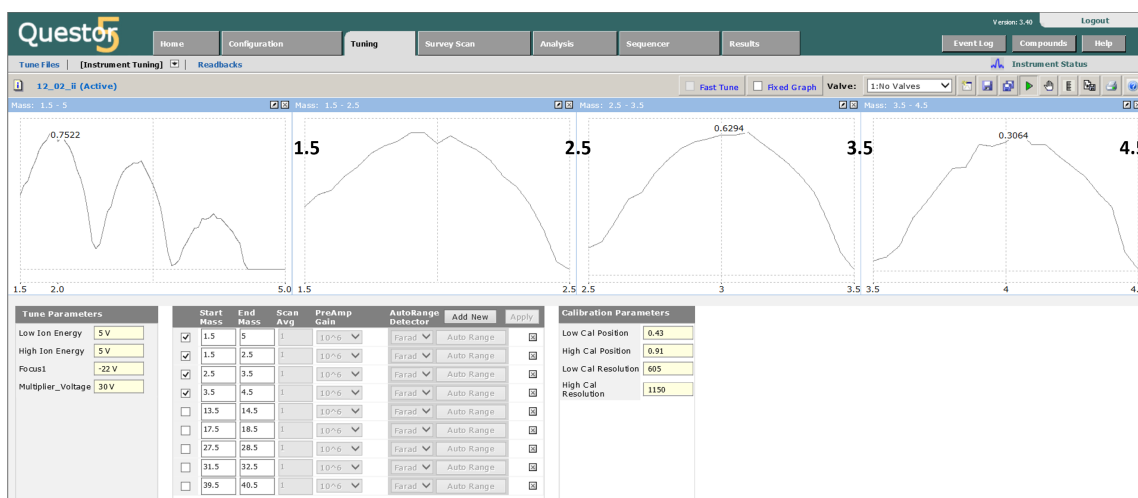
Figure 6.3: Display of the tuning screen in Questor 5 software, showcasing the peaks for H_2, HD, and D_2.

data acquisition.

6.5 Results and Discussion

Our research commenced with distinct objectives – to construct and assess an OEMS system capable of real-time, continuous monitoring and analysis of evolved gases, with a particular focus on hydrogen and deuterium gasses. Our experimental findings affirm that we have successfully achieved these goals. Our OEMS system effectively mapped the dynamics of the electrochemical isotopic exchange reactions, yielding comprehensive concentration-time profiles for H_2, D_2, and HD gases. Figure 6.3 showcases the capability of our QMS to distinctly resolve peaks at mass-to-charge ratios (m/z) of 2, 3, and 4, highlighting its precision in differentiating between molecular ions of close m/z values. This ability addresses our principal research question regarding real-time monitoring of these reactions. Our findings also showcased the sensitivity of our system to alterations in electrochemical parameters, thus highlighting its potential for optimization and adaptability to diverse research needs.
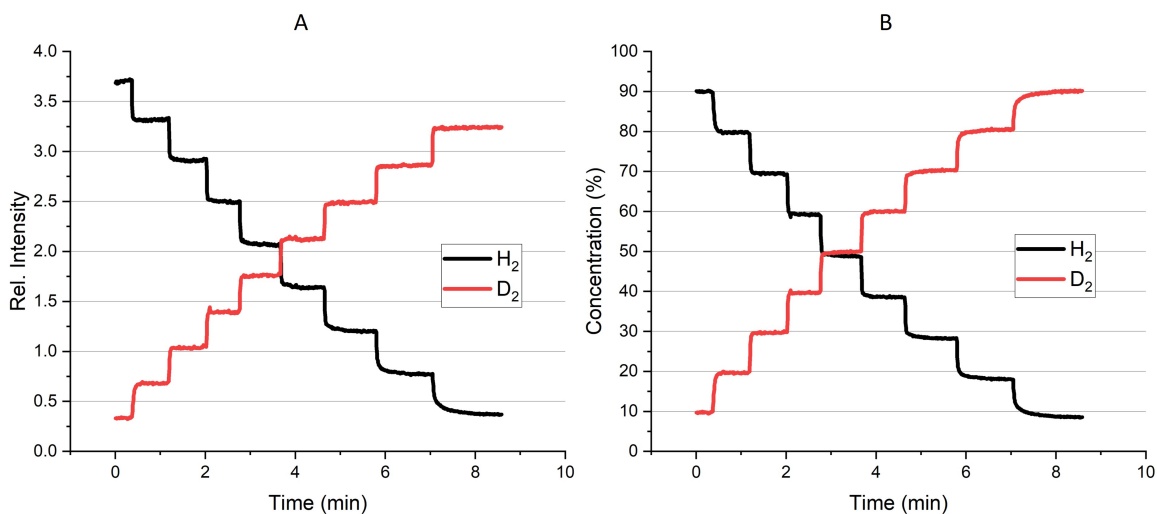
Figure 6.4: Time-resolved simultaneous recording of the relative intensities of H_2 (2 m/z) and D_2 (4 m/z) (A), alongside the instrument-detected concentration (%) of H_2 and D_2 for each calibration gas mixture (B), represented side by side. The gas mixtures were varied step-wise from a ratio of 90:10 to 10:90. The change in ratio was implemented once the system reached steady-state readings, demonstrating the system's response to changes in gas composition. This graph correlates the relative intensity measurements with the accurate detection and concentration determination of H_2 and D_2 in each mixture, providing a comprehensive visualization of the step-wise variation of gas ratios.

Our calibration protocol effectively demonstrates the accuracy and precision of our QMS setup in detecting and differentiating H_2 and D_2 under a variety of conditions. This accuracy was exemplified through a systematic series of experiments involving H_2 and D_2 mixtures, at concentrations varying from 90:10 to 10:90 (H_2:D_2) as outlined in Table 6.1. After achieving steady-state conditions in relative intensity and concentration, inlet gas flow was changed to the next gas mixture from MFCs. The reliability of our calibration approach is underscored by the system's consistent response to the shifts in gas composition (Figures 6.4A and 6.4B) and the observed correlation between actual and detected gas concentrations (Figures 6.5A and 6.5B). Actual gas concentration was calculated by comparing inlet H_2 and D_2 flow rates.

Upon employing similar calibration to correct the output gas concentrations
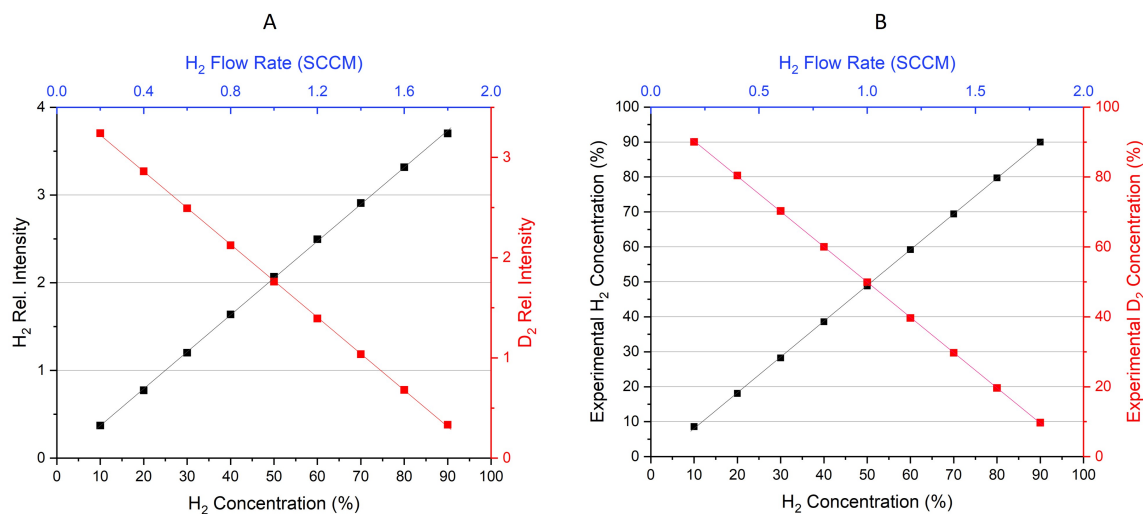
Figure 6.5: This combined multi-axial graph, split into A and B, represents the correlation between H_2 and D_2 relative intensities (A), and the instrument-detected concentrations (expressed as percentages) (B) against their corresponding flow rates and concentrations (dual X-axes). From the perspective of H_2, the X-axes extend from 0 to 2 sccm (flow rate) and 0 to 100% (concentration). In contrast, for D_2, the X-axes are interpreted in the reverse direction, from 2 to 0 sccm and 100 to 0%. This arrangement allows simultaneous evaluation of both H_2 and D_2 dynamics and the instrument's accuracy in recording H_2 and D_2 concentrations under varying flow rates and concentrations.

during a -40 mA chronopotentiometry test on a Membrane Electrode Assembly (MEA), the resulting relative intensities for H_2, D_2, and HD aligned well with their expected values. As depicted in Figure 6.6A, the QMS accurately identified and assigned the m/z values for H_2, D_2, and HD, consistently tracking their respective compositions over time (Figure 6.6B). HD concentration, intriguingly, was derived by subtracting the combined concentrations of H_2 and D_2 from 100%. The time-resolved concentration plots of the evolved gases (Figure 6.6) provided valuable insights into the isotopic exchange reaction kinetics, thereby attesting to our system's efficiency.

The accuracy and responsiveness of our instrument are clearly demonstrated by our calibration curves. With the assistance of 1/16-inch diameter PEEK tubing and a flow of 20 SCCM of Argon as the carrying gas, the input gas mixture is efficiently
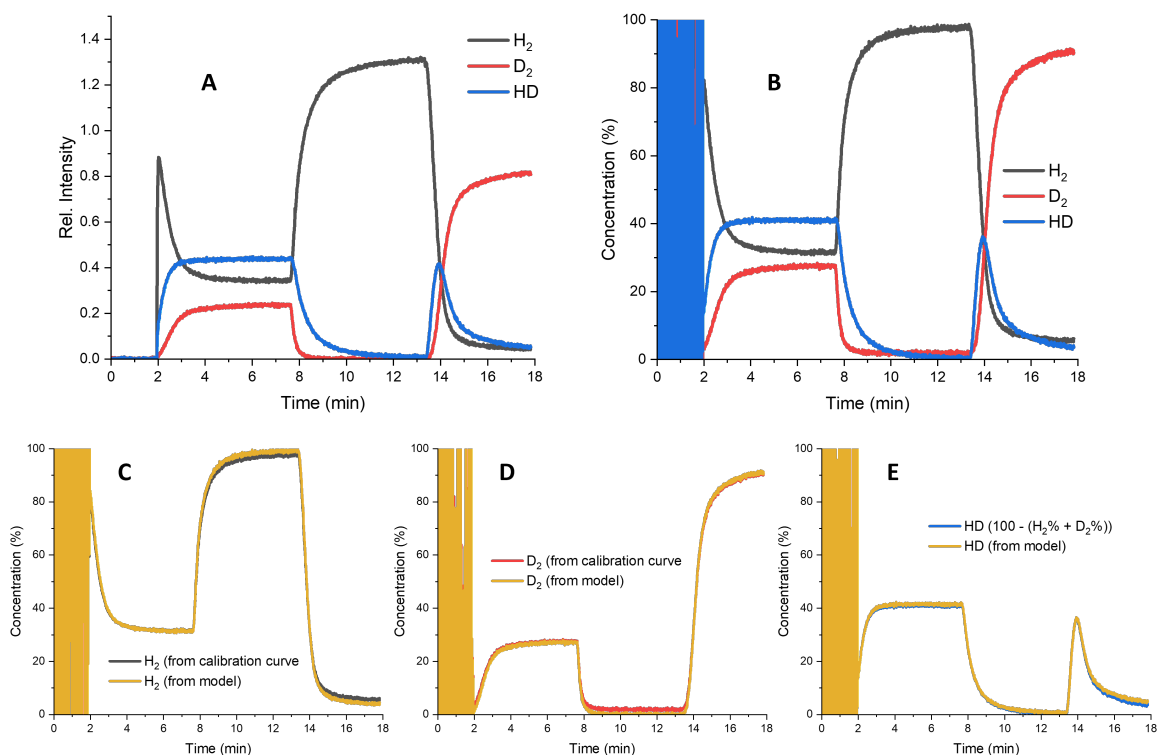
Figure 6.6: Gas output and calibration model validation over time in a NN membrane. (A) Temporal variation in relative intensities of output gas mixture from the electrochemical pump cell when humidified H_2 and D_2 were supplied. (B) Evolution of instrument-detected output gas concentrations over time. (C-E) Validation of calibration model with H_2, D_2, and HD respectively, comparing calculated (from CC) vs. modeled percentages (m, n, and o). Alterations in the feed gas mixture ratios and flow rates were made at the 8 and 13-minute marks.

transported to the mass spectrometer, minimizing dead volumes.

The data in Figure 6.6 offer insights into the behavior of the NN membrane under various feed conditions and the subsequent alterations in the output gas mixture. Figures 6.6A and 6.6B illustrate the evolution of relative intensities and detected concentrations, respectively, in the output gas mixture over time during a chronopotentiometry (CP) experiment set at -40 mA. Notably, this experiment commenced without pre-humidification, in contrast to the experiment depicted in Figure 6.7, which began (CP initiated) after pre-humidifying the membrane with a flow of 10

SCCMs of both H_2 and D_2 gases to the cell for five minutes. As depicted in Figure 6.6A-B, an initial high percentage of H_2 was observed, accompanied by lower percentages of HD, followed by D2. This transient effect diminished as the level of humidification in the cell increased, correlating with a growing influx of the humidified H2 and D2 mixture. After a couple of minutes, the output gas mixture reached a steady-state composition for this membrane, signaling the optimal condition of the MEA.

A dramatic change is observed when the feed gas mixture ratio is altered at the 8-minute mark from 50:50 to 100:0 (H_2:D_2), demonstrating the system's immediate response to changes in the input parameters. A subsequent change to a 0:100 H_2:D_2 ratio at the 14-minute mark further exemplifies the system's dynamic adjustment capability. Figure 6.6B represents the temporal changes in output gas concentration as the feed gas mixture is adjusted. It becomes evident that the concentrations of the output gases are heavily dependent on the input conditions and respond accordingly.

The validity of the proposed calibration model was assessed, as depicted in Figures 6.6C, 6.6D, and 6.6E. In these figures, the calculated concentrations of H_2 and D_2 (derived from the calibration curve) and HD (determined by 100 - (H_2 + D_2)) are contrasted with their modeled values (m, n, and o). Across all three gases, the plots display a strong correlation, underscoring the model's precision. Notably, when the relative sensitivities of H_2, D_2, and HD are set to 0.44, 0.35, and 0.42 respectively, an optimal fit is achieved for all gases, bolstering confidence in the model's robustness. In sum, the data in Figure 6.6 offer a comprehensive understanding of the behavior of the NN membrane in response to changes in the feed gas mixture and validate the proposed calibration model. This advances our knowledge in this area and could have implications for the optimization of similar systems in the future.

The steady-state isotopic composition of gases evolved from the electrochem-
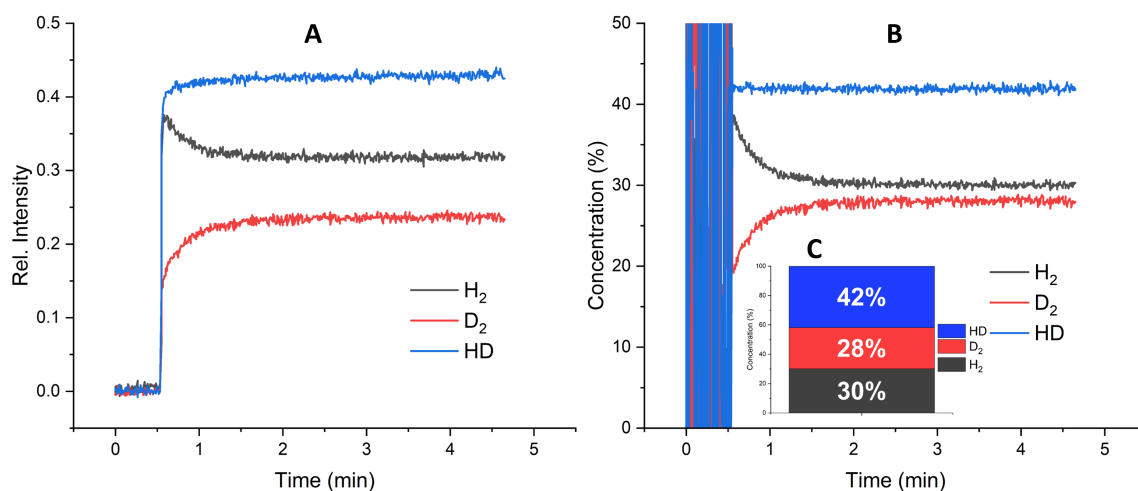
Figure 6.7: (A) A time-series graph displaying the relative intensities of m/z values 2, 3, and 4, corresponding to H_2, HD, and D_2 gases, detected by the QMS during a -40 mA chronopotentiometry test on an MEA [Anode (Pt/C) — Nafion 211 *2 — Cathode (Pt/C)] using a humidified 50:50 H_2 and D_2 mixture. (B) Time-dependent variations in concentrations of H_2, D_2, and HD, corrected using calibration curves. This offers insights into the changing composition of output gases transported by an Ar carrier over time. (C) A depiction of the steady-state concentration percentages of the gases when the system reaches equilibrium, providing a concise view of the gas mixture composition.

ical hydrogen pump cell is presented in Figures 6.7A, 6.7B, and 6.7C, effectively illustrating the outcomes of the electrochemical reactions. Unlike the experiment depicted in Figure 6.6, the MEA was humidified for 5 minutes before starting the CP. Interestingly, we didn't observe the initial transient selectivity that was apparent with the non-humidified membrane, indicating that such selectivity is primarily influenced by the MEA's hydration level. This insight highlights the system's capability to monitor isotopic exchange reactions. Precisely detecting and quantifying H_2, D_2, and HD gas compositions across a range of conditions is crucial for enhancing our understanding of electrochemical pump operations and advancing high-efficiency fuel cell systems. In conclusion, our findings emphasize the capacity of our system to perform continuous, real-time analysis of evolved gases and effectively monitor electrochemical reactions, setting the stage for further studies and optimization in diverse electrochemical systems.

Table 6.2: Overview of the steady-state concentration percentages of H_2, D_2, and HD gases, as detected by the QMS.

Detected Gas	Steady-State Concentration (%)
H_2	30
D_2	28
HD	42

6.6   Conclusions

Our investigation centered on developing an OEMS system to allow real-time, continuous monitoring and comprehensive understanding of the electrochemical gas evolution processes involving H_2 and D_2. The system capably differentiated between H_2, D_2, and HD isotopes and tracked their concentration changes in real-time. This

successful implementation underlines the effectiveness of our system.

The importance of our work is underpinned by the in-depth insights it provides into the electrochemical dynamics of hydrogen isotopes. By enabling real-time monitoring, our system stands superior to conventional 'snapshot' analysis techniques, contributing to a more exhaustive understanding of the processes at hand.

Our system's primary strength is its capacity for real-time evolved gas analysis. By integrating an electrochemical hydrogen pump with a QMS, we captured the dynamic evolution of hydrogen isotopes. The use of the Extrel MAX300-CAT Quadrupole Mass Spectrometer augmented our system's sensitivity and precision. Implementing chronopotentiometry at -40 mA induced a steady gas evolution state, and the utilization of gas diffusion electrodes and Nafion Proton Exchange Membrane was instrumental in the effective functioning of the electrochemical cell. Our calibration methodology, using varied H_2 and D_2 mixtures, ensured reliable measurements.

Our OEMS system holds potential in a myriad of applications. In the realm of sustainable energy, our system can improve the performance of hydrogen-based technologies like fuel cells and electrolyzers. Its capability to distinguish between isotopic species makes it a valuable resource in nuclear fusion research, where understanding isotopic exchange reactions is vital. By facilitating these reactions under different conditions, our system paves the way for advancements in these crucial research fields.

6.7 Future Work

The study's outcomes have produced valuable insights into the electrochemical evolution of hydrogen isotopes, laying a robust foundation for future investigations. Owing to the rising interest in hydrogen as a sustainable energy source, continued research in this domain is both necessary and promising. Exploring the electrochem-

ical behavior of other isotopes in different electrolyte types would be interesting. The effect of electrode materials and the design of the electrochemical cell on reaction kinetics and efficiency also merit further investigation. Potential isotopic fractionation during the electrochemical process could reveal variations significant for isotope separation technologies.

Moreover, the detailed temporal resolution of our data presents unique opportunities for advanced data analytics. Machine learning algorithms could be utilized for recognizing and predicting gas evolution patterns, thereby offering new ways to optimize electrochemical reactions in real-time. Despite its versatility and effectiveness in understanding gas-evolving reactions, our OEMS system can be further improved and adapted for innovative applications. Integration of additional detectors or sensors, like a pH sensor, could offer complementary information about electrochemical reactions. Improving the inlet valve and fluidic design could enhance gas transfer efficiency from the electrochemical cell to the mass spectrometer, potentially aided by Computational Fluid Dynamics (CFD) simulations.

Despite the promising results of our study, we recognize certain limitations that need to be addressed. When interpreting mass spectrometry data, we need to meticulously account for isotopic contributions from H_2, D_2, and HD. Slight discrepancies in isotope ratios or calibration inaccuracies could potentially affect the precision of our data. An additional constraint in our system is observed during rapid alterations in the flow rates of H_2 and D_2. We have found that while D_2 adjusts quickly to changes in flow rate, H_2 has a slightly slower response time. This discrepancy manifests as a persistent background peak at 2 m/z, which can affect the accuracy of real-time analysis.

To address these issues, we've made significant modifications to the roughing pump bellows. By employing larger bellows and removing a junction, we managed

to substantially reduce the time required for the background peak to dissipate. This adjustment has markedly improved our system's response time and accuracy during rapid changes in gas flow rates. It is worth considering potential improvements to the Quadrupole Mass Spectrometer to further alleviate the issue of the background peak at 2 m/z. One approach could involve making adjustments to the bellows of the rough pump to facilitate fast removal of hydrogen from the MS. Moreover addition of a second rough pump (or another pump to aid the rough pump) would be helpful for fast removal of background peak at 2 m/z. Additionally, the incorporation of advanced ionization techniques could help to reduce interference and noise, thus improving the signal-to-background ratio. The implementation of a more dynamic ion detection system, which could adjust more rapidly to changes in gas flow rates, might also be beneficial. Finally, integrating machine learning algorithms could allow for the prediction and subsequent removal of these background signals, thus optimizing the real-time analysis of evolved gases. Through these advancements, we foresee a potential for even more accurate, precise, and efficient analysis using our OEMS system, further reinforcing its applicability in hydrogen-based technology research. These opportunities for exploration and adaptation further validate the potential of our system in future research.

References

(1) Zhang, X.; Zhan, J.; Yu, Z.; Deng, J.; Li, M.; Shao, Y. *Chinese Journal of Chemistry* **2023**, *41*, 214–224.

(2) Baltruschat, H. *Journal of the American Society for Mass Spectrometry* **2004**, *15*, 1693–1706.

(3) Bruckenstein, S.; Gadde, R. R. *Journal of the American Chemical Society* **1971**, *93*, 793–794.

(4) Wolter, O.; Heitbaum, J. *Berichte der Bunsengesellschaft für physikalische Chemie* **1984**, *88*, 2–6.

(5) Javier, A.; Chmielowiec, B.; Sanabria-Chinchilla, J.; Kim, Y.-G.; Baricuatro, J. H.; Soriaga, M. P. *Electrocatalysis* **2015**, *6*, 127–131.

(6) Shakibi Nia, N.; Martucci, A.; Granozzi, G.; García, G.; Pastor, E.; Penner, S.; Bernardi, J.; Alonso-Vante, N.; Kunze-Liebhäuser, J. *Electrochimica Acta* **2019**, *304*, 80–86.

(7) Svengren, H.; Chamoun, M.; Grins, J.; Johnsson, M. *ChemElectroChem* **2018**, *5*, 44–50.

(8) Lysgaard, S.; Christensen, M. K.; Hansen, H. A.; García Lastra, J. M.; Norby, P.; Vegge, T. *ChemSusChem* **2018**, *11*, 1933–1941.

(9) Jusys, Z.; Binder, M.; Schnaidt, J.; Behm, R. J. *Electrochimica Acta* **2019**, *314*, 188–201.

(10) Möller, S.; Barwe, S.; Masa, J.; Wintrich, D.; Seisel, S.; Baltruschat, H.; Schuhmann, W. *Angewandte Chemie International Edition* **2020**, *59*, 1585–1589.

(11) De Souza, J. C. P.; Silva, W. O.; Lima, F. H. B.; Crespilho, F. N. *Chemical Communications* **2017**, *53*, 8400–8402.

(12) Queiroz, A. C.; Souza, M. L.; Camilo, M. R.; Silva, W. O.; Cantane, D. A.; Messias, I.; Pinto, M. R.; Nagao, R.; Lima, F. H. B. *ChemElectroChem* **2022**, *9*, e202101408.

(13) Willms, T.; Kryk, H.; Hampel, U. *Journal of Chromatography A* **2016**, *1458*, 126–135.

(14) Moreno-García, P.; Kovács, N.; Grozovski, V.; Gálvez-Vázquez, M. d. J.; Vesztergom, S.; Broekmann, P. *Analytical Chemistry* **2020**, *92*, 4301–4308.

(15) Santasalo-Aarnio, A.; Kwon, Y.; Ahlberg, E.; Kontturi, K.; Kallio, T.; Koper, M. T. M. *Electrochemistry Communications* **2011**, *13*, 466–469.

(16) Hosoda, R.; Kamoshida, N.; Hoshi, N.; Einaga, Y.; Nakamura, M. *Carbon* **2021**, *171*, 814–818.

(17) Borer, P.; Hug, S. J. *Journal of Colloid and Interface Science* **2014**, *416*, 44–53.

(18) Oberacher, H.; Pitterl, F.; Erb, R.; Plattner, S. *Mass Spectrometry Reviews* **2015**, *34*, 64–92.

(19) Liu, P.; Lu, M.; Zheng, Q.; Zhang, Y.; Dewald, H. D.; Chen, H. *Analyst* **2013**, *138*, 5519–5539.

(20) Herl, T.; Matysik, F.-M. *ChemElectroChem* **2020**, *7*, 2498–2512.

(21) Miao, Z.; Chen, H.; Liu, P.; Liu, Y. *Analytical Chemistry* **2011**, *83*, 3994–3997.

(22) Yasuda, S.; Matsushima, H.; Harada, K.; Tanii, R.; Terasawa, T.-o.; Yano, M.; Asaoka, H.; Gueriba, J. S.; Diño, W. A.; Fukutani, K. *ACS Nano* **2022**, *16*, 14362–14369.

(23) Lozada-Hidalgo, M.; Hu, S.; Marshall, O.; Mishchenko, A.; Grigorenko, A. N.; Dryfe, R. A. W.; Radha, B.; Grigorieva, I. V.; Geim, A. K. *Science* **2016**, *351*, 68–70.

(24) MAX300-CAT Product Note `https://extrel.com/wp-content/uploads/2020/12/MAX300-CAT-Product-Note-LPC100D.pdf` (accessed 08/07/2023).

(25) Operating principle: Laminar differential pressure mass flow technology `https://www.alicat.com/choosing-an-instrument/theory-of-operation-laminar-differential-pressure-flow-measurement/` (accessed 08/07/2023).

(26) Zhu, P.; Gastol, D.; Marshall, J.; Sommerville, R.; Goodship, V.; Kendrick, E. *Journal of Power Sources* **2021**, *485*, 229321.

Chapter 7

Impact of CVD Graphene-Embedded Nafion Membranes on Hydrogen Isotope Selectivity

7.1 Abstract

This research undertakes a comprehensive investigation using online electrochemical mass spectrometry (OEMS) into the isotope selectivity of graphene-embedded Nafion membranes for electrochemical hydrogen isotope separation. The work expands upon prior studies by implementing an updated preparation procedure for the CVD graphene-embedded membranes that focuses on reprotonation/redeuteration after the copper etching step. The absence of high isotope selectivity attributable to CVD graphene-integrated Nafion membranes was systematically demonstrated via OEMS analysis of the output gas mixtures from electrochemical hydrogen pump cells

fed with a mixture of H_2 and D_2 gases. The findings have significant implications for the broader field of hydrogen isotope separation, specifically questioning the previously held belief about the role of CVD graphene in such processes. The study concludes with the presentation of potential directions for future research, underlined by the necessity for meticulous experimental design and protocol modification in advancing the field.

7.2 Introduction

In the realm of nuclear fusion, the quest for high-performance materials for hydrogen isotope separation becomes paramount, given its importance in nuclear fusion, heavy water reactors, and specific medical applications[1][2]. Ensuring the efficient separation, enrichment, and reuse of deuterium and tritium from nuclear fusion byproducts and radioactive wastewater is fundamental for ecological safety and economic longevity in the nuclear and fusion industry[3][4][5]. Among various separation methodologies such as palladium membrane diffusion[6], cryogenic distillation[7], and quantum sieving[2][8], the use of membranes in electrochemical pumping for hydrogen isotope selectivity stands out[9][10][11]. It's especially promising due to its potential for reduced energy consumption and scalability[10]. Graphene, a single atomic layer of carbon atoms arranged in a two-dimensional honeycomb lattice, has emerged as an attractive candidate in separation science because of its atomic thickness and potential for selective permeability[12][13][14]. When incorporated into Nafion, a commonly used proton exchange membrane, the resulting hybrid material has previously been reported to demonstrate high separation efficiencies for hydrogen isotopes[9].

Recently, an exploration into the integration of single-layer graphene, pre-

pared via a Chemical Vapor Deposition (CVD) technique, into Nafion membranes has gained momentum[10][15]. The superior mechanical, thermal, and electrical properties of graphene, coupled with its impermeability to gases, positions it as an excellent candidate for enhancing Nafion membranes' performance. Initial studies reported notable isotope separation factors, with some claims reaching values as high as 8[10] and 14[9]. However, these claims, while fascinating, were based on experimental designs that overlooked critical factors such as defects in the graphene layer introduced during the transfer process, ammonium and copper contamination during the etching process, and the lack of proper control experiments, as discussed in Chapter 5 of this dissertation.

Given these findings and questions raised in the literature concerning claims of H/D selectivity by CVD graphene[16], this study embarks on an in-depth investigation into the genuine isotope selectivity of graphene-embedded Nafion membranes. By rectifying issues encountered in previous experimental designs and introducing an updated procedure for membrane preparation, we aim to bridge the gaps in the current understanding of hydrogen isotope separation in these membranes and provide reliable insights for further development in this field.

Our study aims to elucidate the real contribution of graphene to isotope selectivity in the hydrogen-deuterium separation process. Previous studies have hinted at a potential role for graphene in enhancing isotope selectivity, though these findings have been obscured by methodological issues including the fact that they did not explicitly study separations, but rather compared relative rates for transport. To address these challenges, we utilize the advanced analytical capabilities of OEMS to analyze mixtures of gases evolved from electrochemical pump cells. OEMS enables us to analyze the output gas mixtures produced during hydrogen isotope separation with exceptional precision and accuracy. Through a systematic experimental approach and

rigorous analysis, this research contributes to the broader understanding of graphene's potential role in hydrogen isotope separation. A detailed examination of this process not only clarifies the role of graphene but also provides invaluable insights into the challenges and prospects of graphene-Nafion composites. These findings establish a solid foundation for future advancements in hydrogen isotope separation research and technology, ultimately aiding the quest for more efficient materials in this field.

7.3 Materials and Methods

7.3.1 Revised Procedure for Fabrication of NGN Membranes

The fabrication of graphene-embedded Nafion membranes has been further refined to improve reliability and effectiveness. To create twelve sandwich-like membranes, six integrated graphene layers within two Nafion 211 layers (NGN) and six consisting of solely Nafion 211 layers (NN) were assembled. Graphene grown on copper sheet from Chemical Vapor Deposition (CVD) was purchased from ACS Materials LLC. These copper—graphene sheets were layered onto Nafion 211 and hot-pressed at 140 °C and 600 psi for 3 minutes, creating the copper—graphene—Nafion membrane composites. To remove the copper substrate, the composite membranes were soaked in a 0.3 M Ammonium Persulfate (APS) solution for ~10 hours. After rinsing with water and D_2O respectively, the resulting Graphene—Nafion composites were then separated into two groups: one set of three membranes was immersed in 0.5 M D_2SO_4 in D_2O, and the other three in 0.5 M H_2SO_4 in H_2O, each for a duration of 8 hours. After that they were washed with water and D_2O followed by immersing them in the same solutions for an additional 3 hours. The membranes were then allowed to dry at room temperature. To construct sandwich-like membranes, a single D-form or

123

Figure 7.1: Process of CVD graphene transfer onto Nafion 211 membranes. A. CVD graphene on copper sheets hot-pressed onto single layers of Nafion 211 membranes. Teflon-reinforced fiberglass sheets were placed from either side of it prior to hot-press. B. Copper—graphene—Nafion composites were immersed in 0.3 M APS solution. C. and D. Post-etched graphene-deposited membranes.

H-form Nafion 211 (prepared by soaking in 0.5 M D_2SO_4 in D_2O, or 0.5 M H_2SO_4 in H_2O respectively for 8 hours) was hot-pressed onto the graphene-containing Nafion membranes, again at 140 °C and 600 psi for 3 minutes.

7.3.2 Preparation of Control Membranes: NN Membranes in H and D Forms

Non-graphene control membranes were assembled for comparison. These were constructed by hot-pressing either two H-form Nafion 211 membranes or two D-form Nafion 211 membranes together, mirroring the graphene-integrated assembly process without the inclusion of graphene. All twelve sandwich-like membranes, both graphene-containing and non-graphene controls, were used to create Membrane Electrode Assemblies (MEAs). Two 0.18 cm^2 disk-shaped Pt/C cloth electrodes were hot-pressed onto either side of each sandwich-like membrane, encapsulating the membrane between the two electrodes under identical hot-pressing conditions.

124

7.3.3 Collaborative Efforts: Preparation of Samples from Vanderbilt University

In addition to our in-house preparations, four samples from our collaborators at Vanderbilt University were also evaluated. The preparation method for these samples slightly differed from our own but still preserved the essential structure of graphene-embedded Nafion membranes. At Vanderbilt, the graphene was grown in their laboratory and then transferred to Nafion 211 using a hot press. Copper removal was achieved using a 0.2 M APS solution for approximately 3 hours, a slightly lower concentration and shorter duration compared to our method. Following this, the membranes were immersed in a 0.1 M HCl solution for 24 hours to ensure thorough re-protonation, a longer period than our procedure. Subsequently, they were rinsed extensively with DI water and dried overnight. To complete the sandwich structure, the graphene layer was encapsulated with an additional Nafion 211 layer using a hot press. This resulted in a similar Nafion—Graphene—Nafion configuration to our membranes.

The final step of attaching Pt/C electrodes to these Vanderbilt-prepared membranes followed our own established procedure. Two 0.18 cm^2 disk-shaped Pt/C cloth electrodes were hot-pressed onto either side of each sandwich-like membrane, encapsulating the membrane between the two electrodes under identical conditions to our method.

7.3.4 OEMS Analysis of Output Gas Mixtures

The methodology for OEMS analysis of the output gas mixtures is a crucial aspect of our experimental procedure, building on the protocols detailed in Chapter 6. The newly prepared graphene-embedded Nafion membranes and control Nafion

membranes were mounted in the cell using the procedure outlined in subsection 3.3 of Chapter 6. Chronopotentiometry at -40 mA was then applied using the WaveDriver 20 electrochemical workstation by PineResearch. This process was carried out under the same conditions as our prior experiments, ensuring consistency in our experimental setup. Once the current was applied, the gaseous products of the electrochemical reaction, including hydrogen and deuterium and hydrogen deuteride, were continuously produced and needed to be analyzed. To carry out this analysis, the output gases were transported to the Quadrupole Mass Spectrometer (QMS) by a carrier stream of Argon gas at a flow rate of 20 SCCM.

The gas analysis was performed using the MAX300-CAT™ Laboratory Mass Spectrometer by Extrel. This instrument offers high sensitivity and resolution, allowing for precise measurements of the constituent gases. The operational principles and the specific settings of the QMS were set as per the established protocol detailed in Chapter 6. Data analysis was conducted based on the calibration curve established in our previous work. This enabled us to convert the detected relative intensities for each m/z value into the corresponding concentration (%) of the individual gas components, providing a detailed composition profile of the output gas mixtures. The reliability of our QMS measurements was confirmed through frequent calibration of the OEMS following the calibrating procedure described in Chapter 6, ensuring the robustness and reproducibility of our experimental findings. This rigorous approach to the OEMS analysis of the output gas mixtures ensured that our observations and interpretations were grounded in reliable and accurate data.
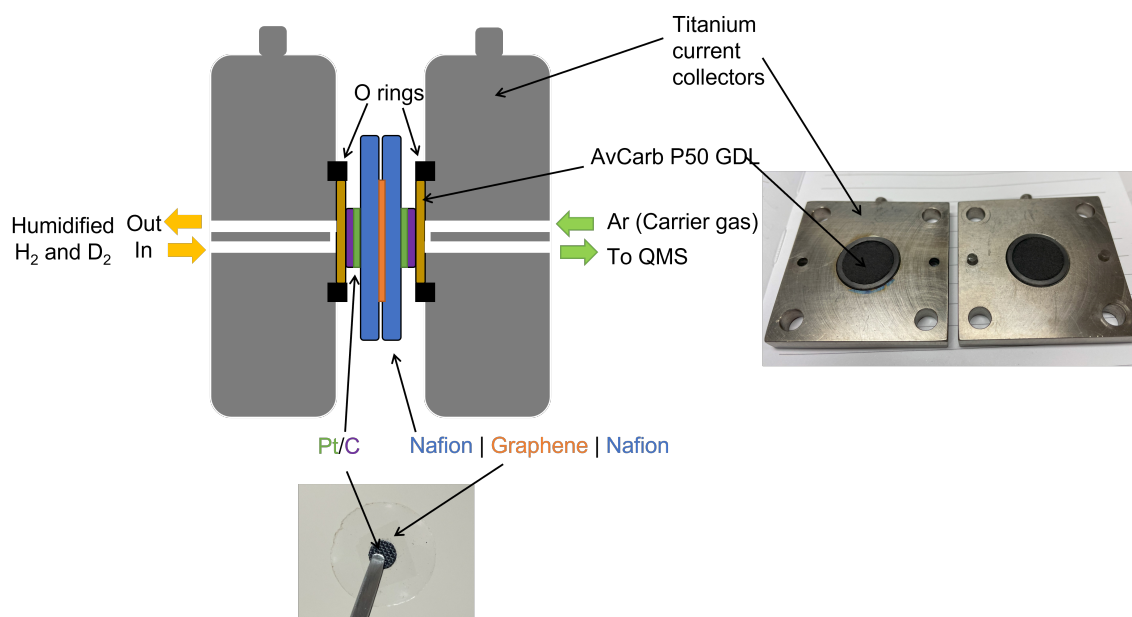
Figure 7.2: Schematic of the hydrogen pump cell setup. Diagrammatic representation of the deuterium/hydrogen pump cell setup.

7.4 Results

7.4.1 Experimental Demonstration of Absence of Graphene's Isotope Selectivity

The central findings of our research emerged from the systematic analysis of output gas mixtures from electrochemical hydrogen pump cells using a QMS. This analysis, which included both the graphene-embedded Nafion membranes and the control non-graphene membranes, was designed to quantify the isotope selectivity imparted by graphene. The results were compelling: across all our experimental runs, the OEMS analysis revealed no detectable isotope selectivity arising from membranes. Regardless of whether the membrane was initially prepared in the H or D form, the OEMS results consistently showed similar output gas composition for all the membranes. This lack of isotope selectivity from graphene was confirmed by

our comparison with the control non-graphene membranes. As anticipated, these control membranes also displayed no significant isotope selectivity. These findings unambiguously demonstrate that the graphene within the Nafion membranes does not contribute to isotope selectivity under the conditions of our experiments. This conclusion directly contradicts previous claims regarding graphene's role in isotope selectivity, compelling a reevaluation of our understanding of isotope transport through graphene-embedded membranes.

7.4.2 Summary of Key Findings with Graphs and Tables

7.5 Results and Discussion

7.5.1 Interpreting the Findings in Light of Study Objectives

Prior to applying a fixed current of -40 mA in chronopotentiometry, the membranes were humidified by passing humidified H_2 and D_2 gas through the anode side of the electrochemical pump cell to reach the optimal proton/deuteron transport condition of the MEA. The primary objective of our study was to determine whether graphene embedded in Nafion membranes truly contributes to isotope selectivity in hydrogen isotope separation. Our results, consistently obtained across several experimental runs, indicate that this is not the case. As demonstrated across Figures 7.3-7.6 and Table 1, OEMS analyses of the output gas mixtures of our MEAs revealed no notable isotope selectivity that could be attributed to the presence of graphene.

A closer look at Figures 7.3, 7.4, and 7.6 reveals that across various MEAs, the predominant component in the output gas mixtures was HD at approximately ∼41%, followed by H2 at ∼32%, and D2 at around ∼27%. The introduction of a graphene layer sandwiched between two decontaminated membrane layers did not change the
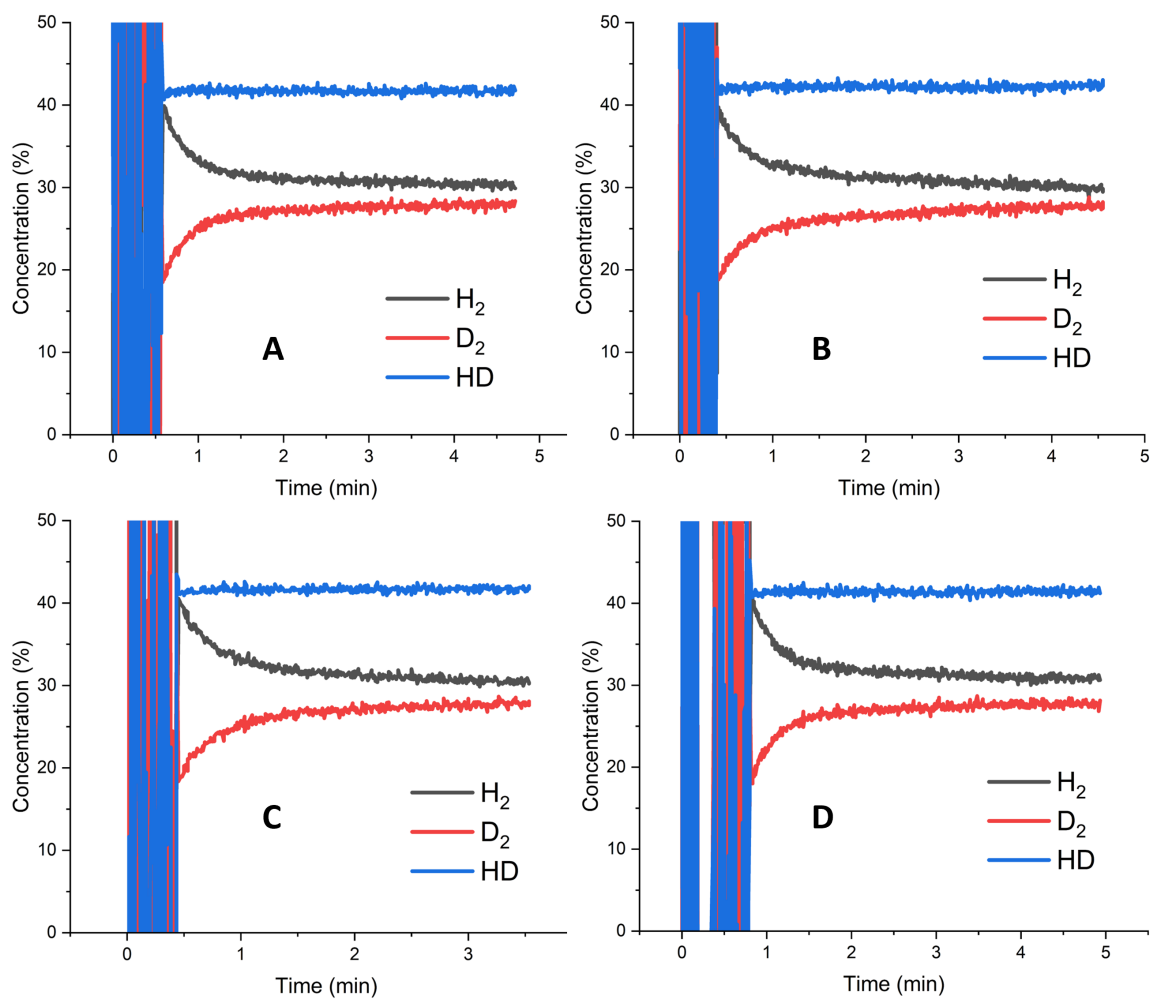
Figure 7.3: Time-dependent variations in concentrations of output gases from each MEA type. A. NN (H), B. NGN (H), C. NN (D), D. NGN (D).
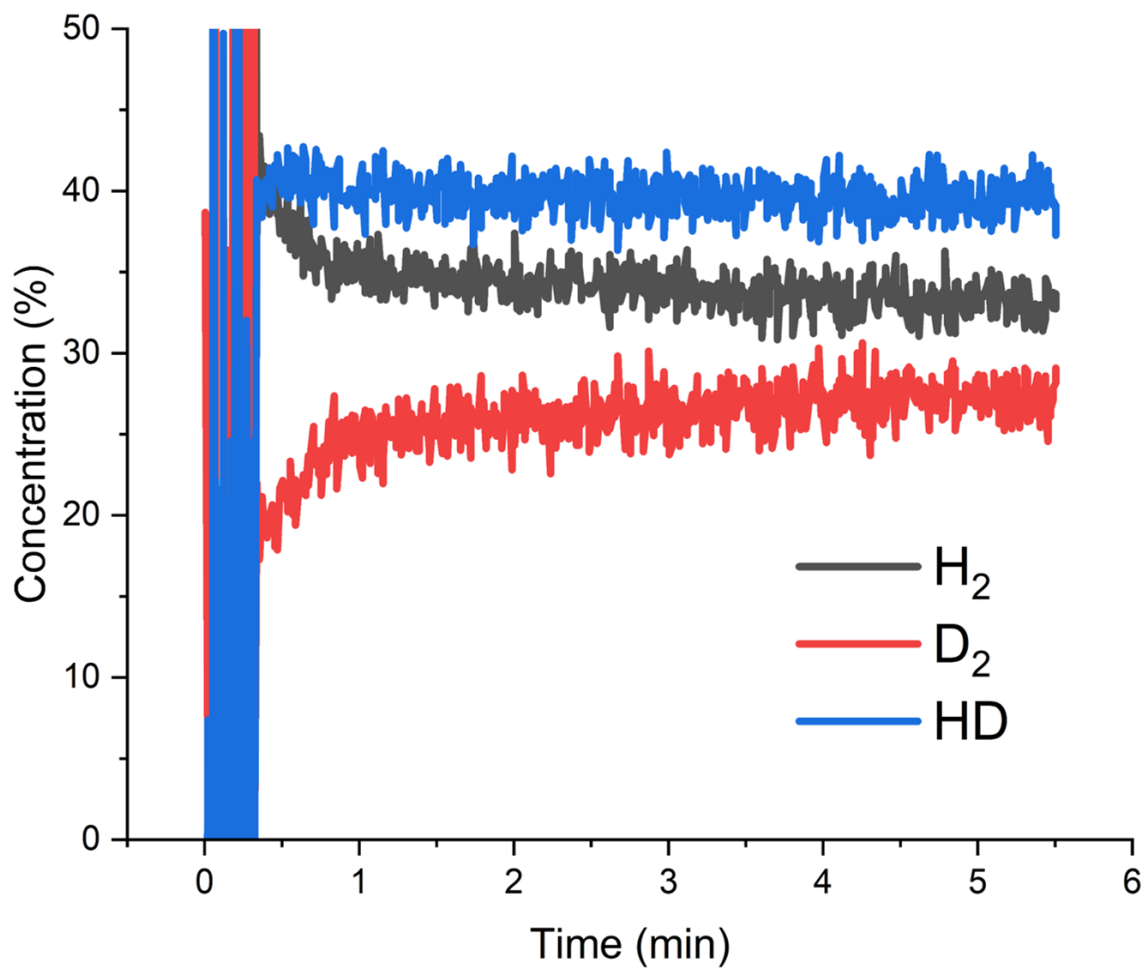
Figure 7.4: Sample time-dependent variations in concentrations of output gases from NGvN (H) MEA.

Table 7.1: Results of QMS analysis. This table presents and compares the output gas mixtures' isotopic composition from the QMS analyses for both the graphene-embedded and non-graphene control membranes. * The NGvN set of membranes represents the membranes that were prepared from CVD graphene grown in Vanderbilt University's laboratory.

Membrane	H_2 %	D_2 %	HD %	H/D Selectivity
NN1 (H)	30	28	42	1.0
NN2 (H)	31	27	42	1.1
NN3 (H)	31	28	42	1.1
NGN1 (H)	30	27	42	1.1
NGN2 (H)	29	29	42	1.0
NGN3 (H)	30	28	42	1.0
NN1 (D)	32	26	42	1.1
NN2 (D)	32	27	42	1.1
NN3 (D)	31	27	42	1.1
NGN1 (D)	29	29	42	1.0
NGN2 (D)	33	26	41	1.1
NGN3 (D)	31	28	41	1.1
NGvN1 (H)	32	29	39	1.1
NGvN2 (H)	35	26	39	1.2
NGvN3 (H)	34	26	40	1.2
NGvN4 (H)	31	30	39	1.0
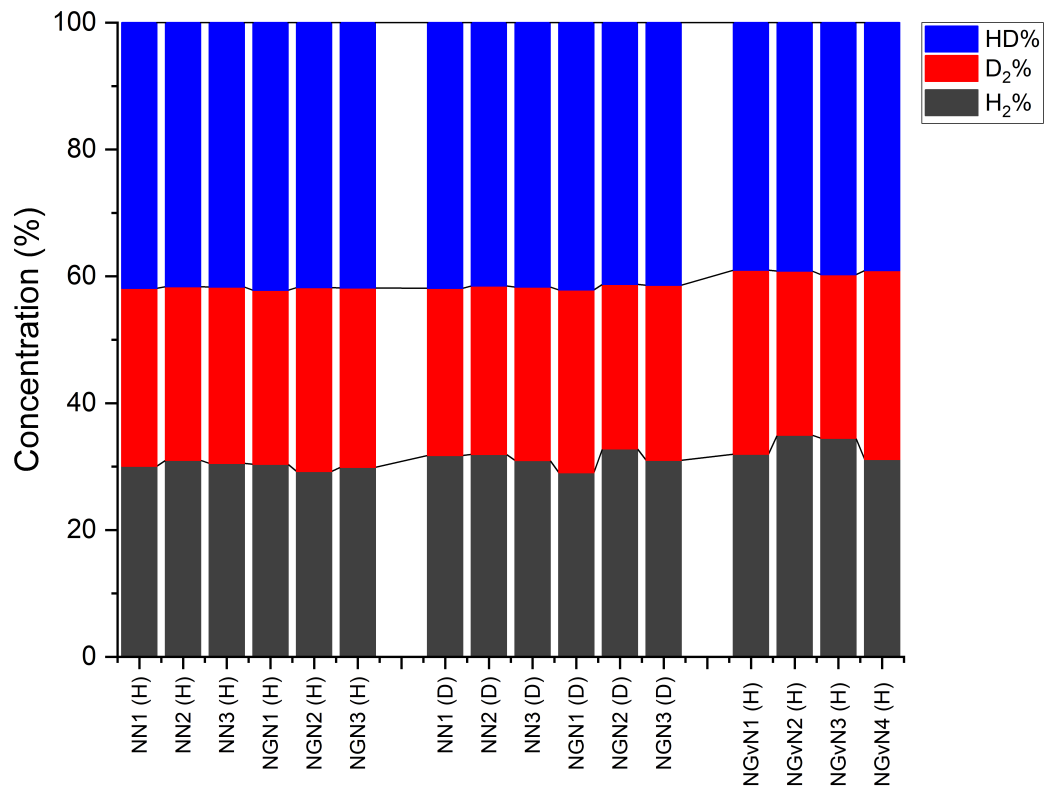
Figure 7.5: Isotopic composition of output gas mixtures from OEMS analyses across all MEAs.
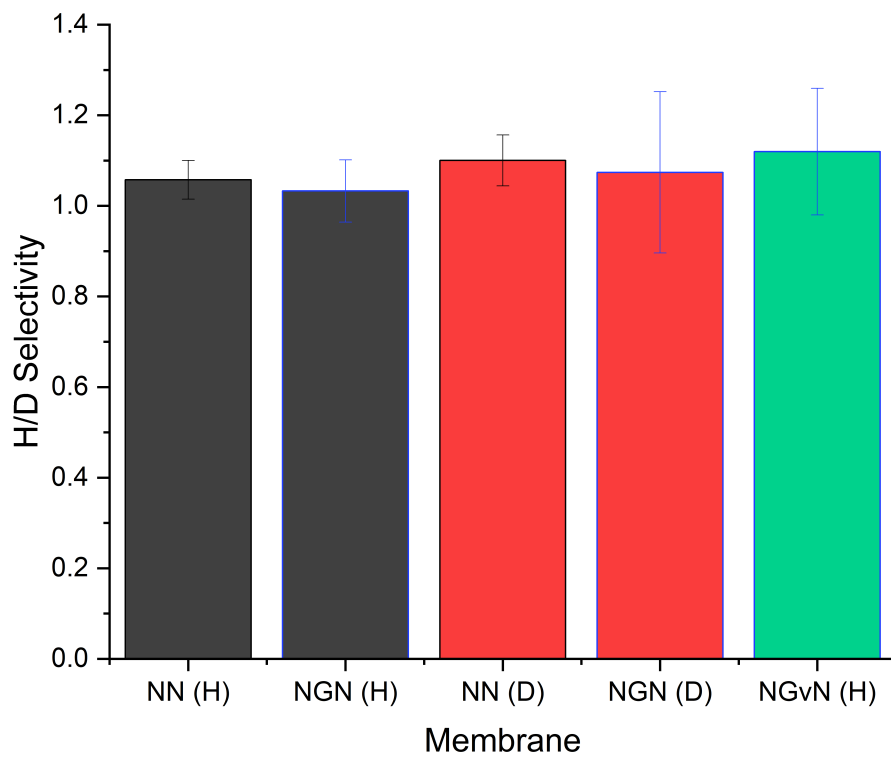
Figure 7.6: Average H/D selectivity for each type of membrane with 95% confidence intervals.
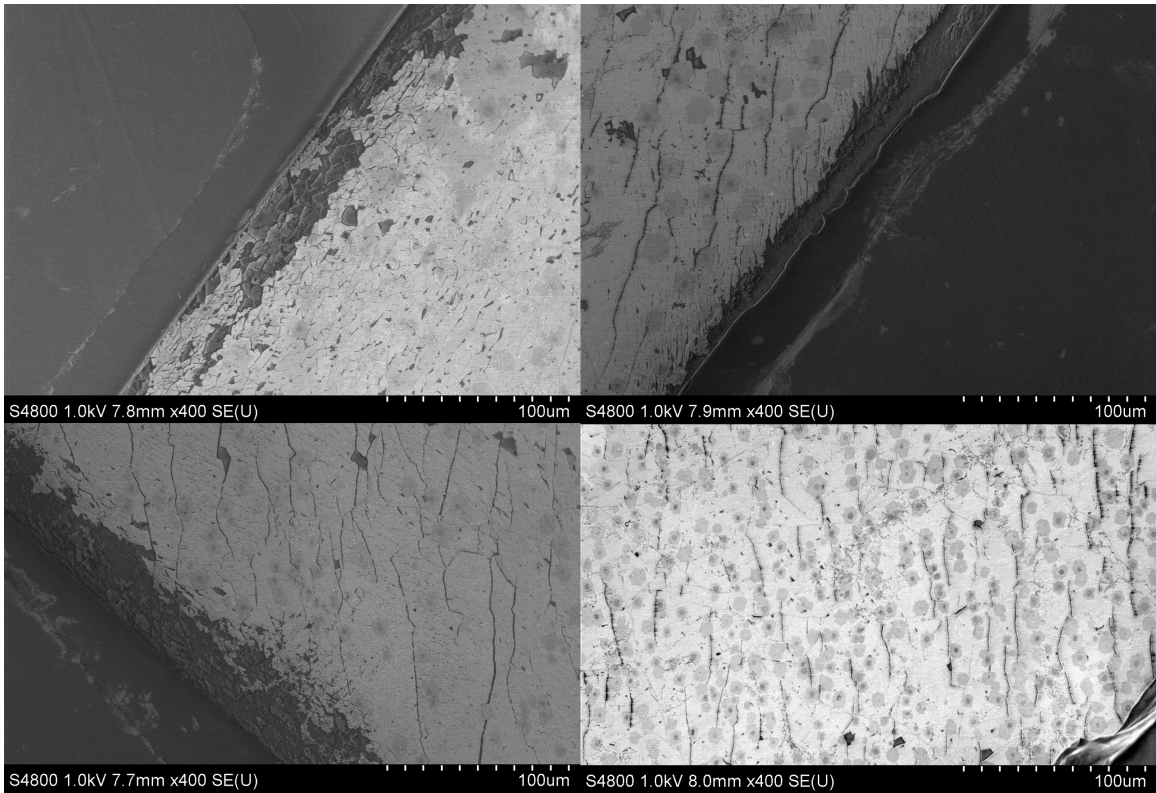
Figure 7.7: Scanning Electron Microscopy (SEM) Images of CVD-Graphene on Nafion 211 Membranes. These high-resolution images obtained from the Hitachi S-4800 SEM showcase the microstructure of the CVD-graphene on Nafion 211 membrane. The darker regions represent the Nafion substrate, whereas the lighter areas depict the graphene layer.

transport in favor of H over D. This trend was consistent throughout various trials, regardless of whether the membranes initially existed in H or D form.

The graphene-embedded membranes and their non-graphene counterparts displayed nearly identical selectivity ratios, estimated to be around 1 to 1.2, when a 50:50 humidified H_2 and D_2 gas mixture was fed to the electrochemical pump cell. This uniformity was evident not just in our MEAs but also in the graphene-integrated membranes sourced from the Vanderbilt group. The H/D selectivity ratios, presented in Table 7.1, were derived using the following equation:

$$H/D \text{ Selectivity } = \frac{H_2(\%) + \frac{1}{2}HD(\%)}{D_2(\%) + \frac{1}{2}HD(\%)} \tag{7.1}$$

These findings strongly counter previous assertions that graphene embedded in Nafion membranes can significantly enhance isotope selectivity. The striking absence of any substantial isotope selectivity due to graphene, as demonstrated in our data, is an essential piece of evidence that clarifies the real role of CVD graphene in these systems. This fulfills our study objective, providing a more accurate understanding of the mechanisms underlying hydrogen isotope separation in graphene-embedded Nafion membranes. It also underscores the need for rigorous controls and meticulous experimental design in such studies to avoid confounding factors and to produce reliable results.

7.5.2 Comparison with Previous Research

A critical part of our study was to compare our findings with those from prior studies. Previous investigations suggested that graphene embedded within Nafion membranes considerably enhances isotope selectivity. Our data, however, challenge this notion by demonstrating a lack of any substantial isotope selectivity attributable

to graphene. We should note that the inconsistency between our findings and previous reports could be due to the variations in experimental conditions and methodologies. For instance, prior studies may not have fully accounted for the potential contamination of membranes with ammonium and copper ions, which can influence transport dynamics and selectivity. In contrast, our study carefully avoided this contamination by reprotonating/redeuterating the Nafion membranes after the copper etching step. Use of a OEMS gas analysis technique to study gas mixtures significantly improves upon indirect methods of measurement, such as conductivity which were performed on distinct MEAs in separate H-pump and D-pump experiments, given that H_2 and D_2 gas mixtures are incompatible with conductivity measurements. Resistance measurements are highly sensitive to cell conditions; any trace of contamination from cations in the membrane would inadvertently elevate resistance levels, as substantiated by the findings presented in Chapter 4. These discrepancies emphasize the importance of thorough controls, meticulous methodology, and rigorous analysis in interpreting results. As our study demonstrates, overlooking these elements can lead to significant misinterpretations of data and inaccurate conclusions.

7.5.3   Discussion on the Observed Isotope Selectivity

The observation that both the graphene-embedded Nafion membranes and the control Nafion membranes yield a similar H/D isotope selectivity ratio (around 1-1.2) suggests that the inclusion of a graphene layer does not appear to influence the selectivity. The data indicate that graphene doesn't provide any significant advantage or modification in terms of enhancing hydrogen isotope selectivity under the given conditions. We propose two main reasons to explain this observation.

The first relates to the etching process and the inherent nature of Nafion 211

to expand when in contact with humidity. Nafion 211 has a reported linear expansion of approximately 10% when it transitions from a relative humidity of 50% at 23 °C (73 °F) to a water-soaked state at the same temperature[17]. This expansion of Nafion 211, however, is not experienced uniformly throughout the membrane during the copper etching process. The etching of copper, initiated at the edges and gradually spreading towards the center, leads to an uneven exposure of the graphene layer and subsequent expansion of the Nafion membrane. Initially, the presence of the copper sheet restricts this expansion due to its rigid nature. But as the etching progresses and copper is removed, the underlying Nafion expands along with the overlying graphene layer. This expansion, while non-uniform, induces stress into the graphene layer, resulting in the development of cracks and holes in the atomically thin layer. This damage compromises the structural integrity of the graphene layer, thereby nullifying its potential effect on isotope selectivity. As depicted in Figure 7.7, SEM images reveal cracks and imperfections on the graphene surface after it has been transferred onto the Nafion membrane.

The second reason revolves around the dynamic conditions the membranes are exposed to, specifically the influence of humidity. Post fabrication, the sandwich-like MEAs are exposed to atmospheric conditions, causing them to absorb moisture and attain equilibrium with their surroundings. This absorbed humidity forms a network of water molecules within the membranes, even prior to the experimental runs. During the experiment, as humidified 50:50 H_2 and D_2 gas is fed into the cell for a extented period of time, the membranes absorb more moisture, and the water molecule network expands, facilitating the hopping of protons/deuterons. Given that the graphene layer is already perforated (as a result of the etching process), it does not obstruct this water network. Consequently, the continuous water pathways govern the transport of protons/deuterons across the membrane, resulting in no difference in

isotope selectivity between the graphene-embedded and non-graphene membranes.

The reasons we propose are further supported by studies from the University of Warwick group, which clearly demonstrated that proton transmission occurs at defect sites in graphene[18].

In conclusion, the findings of this study suggest that while graphene presents many promising characteristics, in the context of this experiment, its inclusion within Nafion membranes does not significantly influence hydrogen isotope selectivity. Further studies may be warranted to optimize the graphene layer incorporation and to explore its potential benefits under different conditions or using different methodologies.

7.5.4 Implications for the Field of Hydrogen Isotope Separation

Our findings carry significant implications for both the academic and industrial sectors involved in hydrogen isotope separation. The observation that the presence of CVD graphene within Nafion membranes does not notably affect hydrogen isotope selectivity challenges the initial hypothesis that graphene's unique properties would enhance this selectivity. The insight that the etching process and subsequent moisture absorption could compromise the structural integrity of the graphene layer adds another dimension to our understanding of graphene-Nafion composites. It alerts us to the complex and subtle interactions at play and their potential to impact membrane performance. This realization invites a reevaluation of the current strategies used for embedding graphene within membranes and calls for a more careful consideration of the broader operating conditions, like humidity and temperature.

Furthermore, the prominent role of a water molecule network within the mem-

branes for proton/deuteron transport signifies the importance of understanding the interaction between the membrane, the embedded graphene, and the surrounding environment. This could also stimulate new research avenues exploring how to control or harness this water molecule network for improved isotope selectivity.

Importantly, our results underscore the need for careful, sophisticated investigation when incorporating new materials like graphene into established systems such as Nafion membranes. The impressive properties of a material in isolation do not automatically translate into improved performance when integrated into a complex system, owing to the array of factors and interactions at play.

The most direct impact is on the design and evaluation of isotope separation membranes. Our findings essentially challenge the perceived benefits of CVD graphene-embedded Nafion membranes in enhancing isotope selectivity for large-scale applications. By demonstrating that CVD graphene may not contribute to selectivity as previously assumed, we highlight the need for continued exploration of other materials and structures that may enhance isotope selectivity. Our results underscore the significance of rigorous control and characterization of such membranes to avoid confounding effects and inaccurate conclusions.

Finally, this study contributes to a more comprehensive understanding of hydrogen isotope separation using Nafion membranes. It provides valuable insights that can guide future research and engineering efforts, aiming to develop improved systems for efficient and effective hydrogen isotope separation.

7.6   Conclusion

A key finding of our study is the lack of isotope selectivity from graphene, contradicting previous assumptions about the material's role in enhancing hydrogen

isotope separation in these membranes. This conclusion was reached through careful analysis of output gas mixtures using OEMS, revealing the inclusion of graphene within Nafion membranes did not yield a noticeable impact on the H/D isotope selectivity ratio. Both the graphene-embedded (ours and Vanderbilt group's membranes) and the control non-graphene membranes exhibited a similar selectivity ratio of around 1-1.2 under a 50:50 H_2 and D_2 gas mixture feed.

The revelation that graphene does not significantly contribute to isotope selectivity within Nafion membranes is of substantial importance to the broader field of hydrogen isotope separation. Given graphene's well-documented unique properties, such as high thermal conductivity, strength, and impermeability to gases, the prevailing assumption has been that the incorporation of graphene into Nafion membranes would naturally lead to enhanced isotope selectivity. Our findings refute this, serving as an essential correction to the understanding of the operational principles behind these graphene-embedded membranes.

The absence of isotope selectivity from CVD graphene prompts a reevaluation of how we approach the design of membranes for hydrogen isotope separation. This suggests that the focus should perhaps shift towards a deeper understanding and optimization of the inherent properties of the membrane material itself, such as Nafion, and the role of kinetic isotope effects and transport differences.

Our findings are thus of high importance, not just in the pursuit of optimizing hydrogen isotope separation, but also in shaping future research directions in the broader field of isotope separation and membrane technology. This study provides a vital reminder of the necessity for continued in-depth examination and rigorous testing of prevailing assumptions in science and technology, leading to more reliable and effective solutions for the challenges we face.

References

(1) Rethinasabapathy, M.; Ghoreishian, S. M.; Hwang, S.-K.; Han, Y.-K.; Roh, C.; Huh, Y. S. *Advanced Materials* **2023**, *n/a*, 2301589.

(2) Oh, H.; Hirscher, M. *European Journal of Inorganic Chemistry* **2016**, *2016*, 4278–4289.

(3) Kim, H.; Kumar Singh, B.; Um, W. *Journal of Industrial and Engineering Chemistry* **2023**, *121*, 264–274.

(4) Fu, X.; Wang, J.; Chen, C.; Yang, M.; Gong, Y.; Hou, J.; Xiao, C.; Cong, H.; Huang, H.; Wang, H.; Peng, S. *Microporous and Mesoporous Materials* **2023**, *348*, 112387.

(5) Gao, R.; Lin, L.; Li, Z.; Liang, Y.; Gu, W.; Yang, J.; Yan, J.; Fan, J. In *Proceedings of the 23rd Pacific Basin Nuclear Conference, Volume 2*, ed. by Liu, C., Springer Nature Singapore, pp 654–667.

(6) Fujiwara, H.; Fukada, S.; Yamaguchi, Y. *International Journal of Hydrogen Energy* **2000**, *25*, 127–132.

(7) Enoeda, M.; Yamanishi, T.; Yoshida, H.; Naruse, Y.; Fukui, H.; Muta, K. *Fusion Engineering and Design* **1989**, *10*, 319–323.

(8) Oh, H.; Kalidindi, S. B.; Um, Y.; Bureekaew, S.; Schmid, R.; Fischer, R. A.; Hirscher, M. *Angewandte Chemie International Edition* **2013**, *52*, 13219–13222.

(9) Bukola, S.; Liang, Y.; Korzeniewski, C.; Harris, J.; Creager, S. *Journal of the American Chemical Society* **2018**, *140*, 1743–1752.

(10) Lozada-Hidalgo, M.; Zhang, S.; Hu, S.; Esfandiar, A.; Grigorieva, I. V.; Geim, A. K. *Nature Communications* **2017**, *8*, 15215.

(11) Lozada-Hidalgo, M.; Hu, S.; Marshall, O.; Mishchenko, A.; Grigorenko, A. N.; Dryfe, R. A. W.; Radha, B.; Grigorieva, I. V.; Geim, A. K. *Science* **2016**, *351*, 68–70.

(12) Hu, S.; Lozada-Hidalgo, M.; Wang, F. C.; Mishchenko, A.; Schedin, F.; Nair, R. R.; Hill, E. W.; Boukhvalov, D. W.; Katsnelson, M. I.; Dryfe, R. A. W.; Grigorieva, I. V.; Wu, H. A.; Geim, A. K. *Nature* **2014**, *516*, 227–230.

(13) O'Hern, S. C.; Boutilier, M. S. H.; Idrobo, J.-C.; Song, Y.; Kong, J.; Laoui, T.; Atieh, M.; Karnik, R. *Nano Letters* **2014**, *14*, 1234–1241.

(14) Boutilier, M. S. H.; Sun, C.; O'Hern, S. C.; Au, H.; Hadjiconstantinou, N. G.; Karnik, R. *ACS Nano* **2014**, *8*, 841–849.

(15) Bukola, S.; Beard, K.; Korzeniewski, C.; Harris, J. M.; Creager, S. E. *ACS Applied Nano Materials* **2019**, *2*, 964–974.

(16) Xue, X.; Chu, X.; Zhang, M.; Wei, F.; Liang, C.; Liang, J.; Li, J.; Cheng, W.; Deng, K.; Liu, W. *ACS Applied Materials amp; Interfaces* **2022**, *14*, 32360–32368.

(17) Nafion Membrane Chart `https://www.fuelcellearth.com/nafion-membrane-chart/` (accessed 08/07/2023).

(18) Bentley, C. L.; Kang, M.; Bukola, S.; Creager, S. E.; Unwin, P. R. *ACS Nano* **2022**, *16*, 5233–5245.